Structure and Dynamic Processes Involved in the Amorphization of Zeolite Y with Different Cations

Xuejiao Sun

Department of Physics

Aberystwyth University

This dissertation is submitted for the degree of

Doctor of Philosophy

April 2018

Acknowledgement

I would like to express my sincere gratitude to both my supervisors Dr Dave Langstaff and Prof. Neville Greaves for the continuous support of my Ph.D study and related research, for their patience, motivation, and immense knowledge. I would like to thank their advice on all the chapters in this thesis. I would also like to thank the support from Geography Department at Aberystwyth University for ICP-MS work, Department of Material Science at Shanghai University for DSC work, I11 at Diamond Light Source for HR-XRPD work, ISIS MARI for inelastic neutron scattering work and ISIS Material Characterization Laboratory for XRPD work. In particular, I would like to thank help from I11 beamline support scientist Dr Sarah Days and ISIS MARI beam scientist Prof Toby Perring for the experiments. Besides，I would like to thank the advice from Dr Edwin Flikkema on the modelling part. Without their help, the thesis could not have been successfully conducted.

I would like to thank my parents for supporting me spiritually throughout writing this thesis and my life in general.

Abstract

Zeolites, as promising raw materials for making glass, have been studied for many years. Their framework structures provide them with properties different from other mineral materials, such as low density, water absorption capacity and ion exchange property. Building from subunit cages, zeolites have a huge family with different properties and topologies. Sodium zeolite Y can be mass-produced and is easy to obtain which is therefore the studied material in this thesis. Although some researches have been done on glass formation from zeolites, many aspects in the amorphization process including thermodynamics, structural changes, dynamical changes need more study. Further more, study on glass formation from ion exchanged zeolite glass is now a new research topic.

In this thesis, *ex situ* temperature induced amorphization of sodium zeolite Y ($Na_{58}Al_{58}Si_{134}O_{384}\cdot 212H_2O$) has been studied. Multiple techniques were used to investigate different properties of it. Differential scanning calorimetry (DSC) was conducted to study the thermal properties of Na zeolite Y, finding that the structural collapse happens over a large temperature range covering 200K, in which the speed of collapse accelerates with higher temperature. Therefore, three target temperatures were chosen in this range to amorphize Na zeolite Y using different lengths of heating time to obtain samples with different degree of amorphization. These amorphous samples are then studied by X-ray powder diffraction (XRPD) and High resolution X-ray powder diffraction (HR-XRPD) to detect their structural changes during collapse. The

data were analyzed by Rietveld Methods (TOPAS software), finding that the amorphization shrinks the cage topology, and makes the charge-compensating Na ion move to sodalite cages and double 6-fold rings (D6R), which are smaller than the super cages. Raman spectroscopy was also used to study the dynamics of Na zeolite Y and its amorphization. The band of 4-fold and 6-fold rings which make up the cages can be clearly seen in the Raman spectra of crystalline zeolite Y, along with a small stretching mode peak feature. When amorphization take place, the peaks for 4- and 6-fold rings will first decrease then grow again suggesting the disappearance and regrowth of the rings. Some new rings like 5-fold rings appear after collapse similar to other dense alumina silicate glasses. Inelastic neutron scattering (INS) was also used to detect the dynamic properties of the Na zeolite Y, suggesting that the cage structure shrinks with amorphization.

Ion exchange can make a lot of changes to the properties of the Na zeolite Y before and after amorphization, therefore, Cu and Nd exchanged zeolite Y are also studied in this thesis. Studied by DSC, the ion exchanged zeolite Y shows higher collapse temperature and faster collapse within amorphization range. This can be caused by the higher field strength and different cation occupancy of the ion exchanged species. Samples with different degrees of amorphization were studied by XRPD and HR-XRPD similar to Na zeolite Y, finding that the exchanged ion shrinks the unit cell in proportion to their higher field strength and smaller ionic sizes in the order Na-Nd-Cu. However, the movement of the cation caused by the heat treatment during

amorphization makes different influence on the Nd and Cu exchanged zeolite. The unit cell size of amorphous Cu zeolite Y becomes larger than crystalline Cu zeolite Y, but still smaller than the crystalline Na zeolite Y. This is due to high field strength of the Cu^{2+} cation and movement of the cations from supercage to sodalite cage. The change of the amorphous Nd zeolite Y is similar to that occurring in Na zeolite Y. Raman spectroscopy for Cu zeolite Y showed quite different features to Na zeolite Y and Nd zeolite Y，the latter two being similar to one another. In Cu zeolite Y the 4-fold and 6-fold peaks diminish in intensity slightly and then grow, when new features like 5-fold rings appearing. The band for 6-fold rings dominates the features of 4- and 5-fold rings, indicating a change in topology for Cu exchanged zeolite Y.

This thesis includes suggestions for further work to confirm the findings. Taken together, these findings contribute to the expanding literature of zeolite amorphization and may find commercialization applications.

Table of contents

1. Introduction

Although glass formation has been studied for many years [*1-3*], there are still many aspects for researchers to discover. Zeolites as starting materials to form glass have some very unique properties [*4*]. For example, they have a nano-porous framework structure, unusual crystalline structures and are easily ion exchanged [*5, 6*]. These properties make zeolites useful in many areas. Zeolite Y is one kind of zeolite which is widely used in industry [*7*], so it is always a convenient raw material in experiments forming zeolite glass [*8, 9*]. This has been frequently studied, however study is required if the different processes involved are to be understood. This chapter offers a background for the present study and includes description of the crystalline state, glassy state, zeolite Y and ion exchange and amorphization that transforms crystals into glasses.

In this chapter, therefore two states of solid will be presented in detail – crystal and glass. These states describe the beginning and end of the glass formation process. As a part of this work, zeolite Y is a principal theme and the starting material for these studies. In the crystalline section, the common properties of symmetries are discussed leading to the particular properties of zeolites. The various ways to form glass and amorphous materials are then explained. Finally, the chapter focuses on explaining how the amorphous state can be reached if melting and quenching is not available

1.1. Crystal

Crystals are a kind of solid whose ions，atoms or molecules are arranged periodically and orderly [*10*]. These always form regular geometrical shapes. In this structure the energy of bonds between constituents is the lowest, so crystal is usually the most stable solid type. Crystals have been recognized by people for thousands of years, however there are mysteries in crystals still needing to be discovered. The study of crystals is known as crystallography. Crystals are everywhere in everyone's daily life, for instance, salt, sugar, and drugs. Diamond is a typical example of a crystal familiar to scientists. It is composed only of carbon atoms, connected by covalent bonding to form face-center cubic structure (Fig. 1.1). This structure makes diamond one of the hardest materials on the earth.

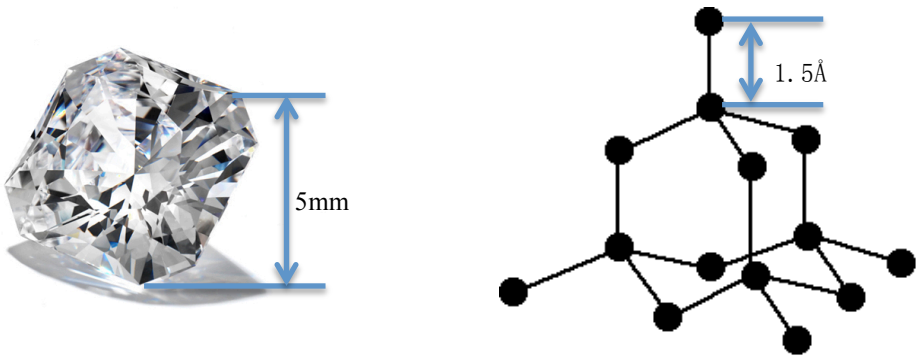

Fig.1.1 Image of diamond and its crystalline structure [*11*]

A lattice system is commonly used to identify the crystal structure, which is built according to specific unit cells referred to an axial system. This is called Bravais lattices and was first introduced by Auguste Bravais in 1850 [*12*]. All crystalline solids may be classed as one of the 7 types of unit cells which are described as

triclinic, monoclinic, orthorhombic, rhombohedral, tetragonal, hexagonal and cubic (Fig. 1.2). A Unit cell can also be divided into three distinct cases depending on whether the additional point is at the centre of the unit cell (*body-centred*), the centre of one face and, because of the translational periodicity, its opposite (*side-centred*) or the centre of all its faces (*face-centred*). They are classified by the three edge, unit cell or lattice parameters (a, b, c) and three interaxial angles (α, β, γ), which are indicated in Fig. 1.2.

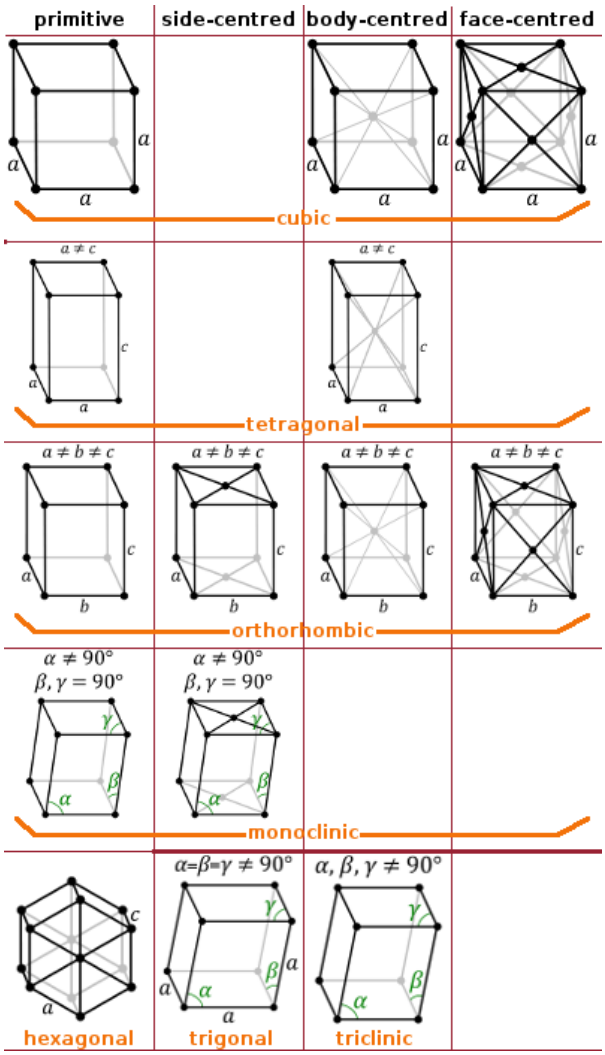

Fig.1.2 Seven types of Bravais unit cell with additional points [*13*]

In these lattice systems, 32 point groups compatible with the 7 types of crystal unit cell. Hermann-Mauguin symbols are used to describe these point groups. This symmetry system has five types of elements including center of inversion, rotation axis, mirror, rotation-inversion axis and screw axis. The parameters (a, b, c) and angles (α, β, γ) are from this system. To describe the structure of a crystal more specifically, space groups are used, which are a combination of translational symmetry and point symmetry. There are 230 space groups in 3-D crystal space. All of these combined together can draw the structure of a crystal very precisely.[*14*]

Because of their periodic structure，crystals have many common features，like:

(i) Homogeneity; density and composition are the same everywhere in the crystal.

(ii) Anisotropy; some properties may differ for different orientations for example electric resistance, heat transfer, birefringence etc.

(iii) A clearly defined melting point, which means the transition to the molten state occurs over a narrow temperature range for a particular pressure.

(iv) As the periodicity is typically a few Angstrom(10^{-10}m), X-rays with a wavelength comparable to this can be diffracted by crystals to produce a pattern which can be analyzed to obtain structural information. [*15, 16*]

1.1.1. Zeolites

The unique physicochemical properties of zeolites make them a very special type of mineral[*7*]. They were originally named zeolites by Swedish mineralogist Axel

Fredrik Cronstedt in 1756 [*17*] from the Greek name "ζέω λίθος" , "ζέω (zéō)" for boiling and "λίθος (lithos)" for stone. This name refers to the fact that zeolites can lose huge amounts of water through boiling when heated. Zeolites can be produced both in nature and synthetically.

One of the most important groups comprises aluminosilicates constructed from TO_4 tetrahedra, where T represents Al or Si. Zeolites are generally classified in terms of the second building units (SBUs), made up of cornersharing TO_4 units. The basic SBUs are listed in Fig. 1.3. To form a regular zeolite structure, the tetrahedral T atom is located in the center of the units and the neighboring oxygen atoms bridge adjacent TO_4 tetrahedra along the connecting line. These units combine together to form channels, layers, cages, bridges and cavities, creating a huge internal surface, typically thousands of square meters per gram. The combinations of the different kinds of SBUs make highly diverse frameworks, therefore leading to large zeolite families. Hundreds of zeolites have been discovered and synthesized, and many more predicted.

Benefiting from each particular structure, zeolites have lots of unique properties different from other dense aluminosilicates, like the minerals nepheline, mallite, sodalite, although their general chemical compositions stay the same:

$$M^{z+}_{m/z}\,[Al_mSi_nO_{2(n+m)}]\cdot qH_2O.$$

Here M can represent one of a number of cations including Na^+, Li^+, K^+, Cu^{2+}, Zn^{2+}…

The cation charge compensates for the AlO_4^- tetrahedral, donating *m/z* electrons, *z* being the cation valence, *m* the atomic fraction of aluminiums present, *n* the number of silicons present , *2(m+n)* the number of oxygens and *q* is the number of water molecules associated. The charge compensating ions fill the framework of the zeolite to give the whole structure neutral charge, usually occupying SBUs adjacent to the aluminiums in the network. The number of water molecules occupying the cavities alters in amount but is usually one to two per tetrahedron. The water present in zeolite can be removed by heating, usually between 473-573K, hence the name “boiling stone”

In general the zeolites can be classified by following rules:

i. a framework structure consists of corner-sharing tetrahedral units

ii. the architecture of channel and cage which usually range in size between 3 to 20 Å

iii. water molecules present in cavities prior to dehydration

iv. cation exchange properties, replacing M cations with other varieties.

According to these rules some aluminophosphates built from AlO_4 and PO_4 tetrahedra can also be called zeolites. In contrast to aluminosilicates, aluminophosphate structures are not charged, so in principle no additional cations are included in the structure.

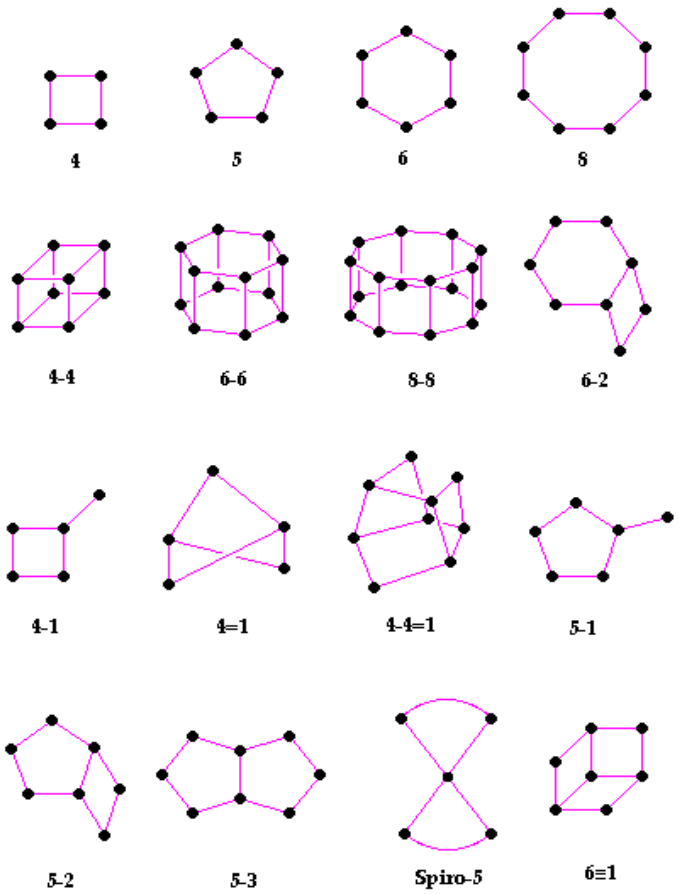

Fig. 1.3 The basic units of zeolite structure [*18*]

As mentioned, the open cage structures give zeolites some special properties. One most obvious property which differs from other minerals is the low density 1.5-1.6 $g \cdot cm^{-3}$, compared with typical values of other minerals 2.2-2.6 $g \cdot cm^{-3}$ of the same basic compositions $M^{z+}_{m/z}\,[Al_mSi_nO_{2(n+m)}] \cdot qH_2O$.

The large internal surface areas in the cavities provide lots of possibilities in zeolite applications [*7*]. The most common capacity coming from this is gas and water absorption. The degree of water adoption varies with temperature, as high temperatures can desorb water from the cavities. When the temperature comes down zeolites can reabsorb water. This captivity is applied widely in the industry to get

water out or to desiccate materials containing water, i.e. as a drying agent. Care needs to be taken as fast removal of water from zeolites can sometimes destroy the channels and cages, for instance by removing the aluminium from the framework, in a process known as “dealumination”. Depending on the channel structure of the zeolite, gases of different molecular dimensions can be transported or separated. This can be called a “molecular sieve”. If the charge compensation cation is H^+, zeolites can act as a solid acid [*19*]. These are used extensively in cracking hydrocarbons in oil refineries.

Ion exchange is another unique property of zeolites, this also benefits from the large internal areas in the cavities and the variety of the possible charge compensating cations. The ion exchange of zeolites is unique because it happens under thermal and chemically mild conditions in contrast to high temperature and/or acidic conditions. Acidic conditions can destroy the zeolite structure. The ion exchange usually involves the cations in the structure but also can involve the framework-building units AlO_4^-. When cation exchange takes place, the new cations can cause major changes in the properties of the zeolites. For example, the stability of the structure can be improved by replacing Na^+ by Nd^{3+} or Cu^{2+}. The unique property of exchanged ion can be shown in the physiochemical features of the zeolite. For example, Nd exchanged zeolite Y is usually used in industrial production because it confers a stable physiochemical condition. Glasses made from Nd^{3+} exchanged zeolites have potential in laser applications, where the Nd is effective in population inversion. Turning to the ion exchange involving AlO_4^-, this kind of exchange is useful to obtain acid resistant

zeolites. This is because the stability of the zeolites under acidic conditions is increased for higher Si/Al ratios. The lack of Al in the zeolite structure can be called dealumination, which can become excessive when the dehydration is too fast causing the structure to collapse. The dealumination should therefore be minimized during zeolite dehydration by slow heating. When the Si/Al ratio reaches more than 10, this zeolite is called high silica zeolite, e.g. silicate. In some circumstances, all the Al in the structure can be exchanged by Si, which will decease the charge compensating cations in the cavities because the interaction with AlO_4^- in the cavities is no longer required.

1.1.2. Zeolite Y

Zeolite Y is the raw material of all these studies in this thesis. It has a Faujasite (FAU) type of structure, with the cubic Space group 227 (Fd-3m)[*20*]. The composition of the zeolite Y material used is $Na_{58}Al_{58}Si_{134}O_{384}\cdot 212H_2O$. The structure of FAU is shown in Fig. 1.4. It is formed by 24 sodalite cages connected by double 6-membered rings (D6Rs) as shown in Fig. 1.4. The lattice parameter or constant is between 24.2-25.2Å, while the super cage diameter is approximately 11.8 Å, sodalite cage is around 9.4 Å and D6R about 7.4 Å.

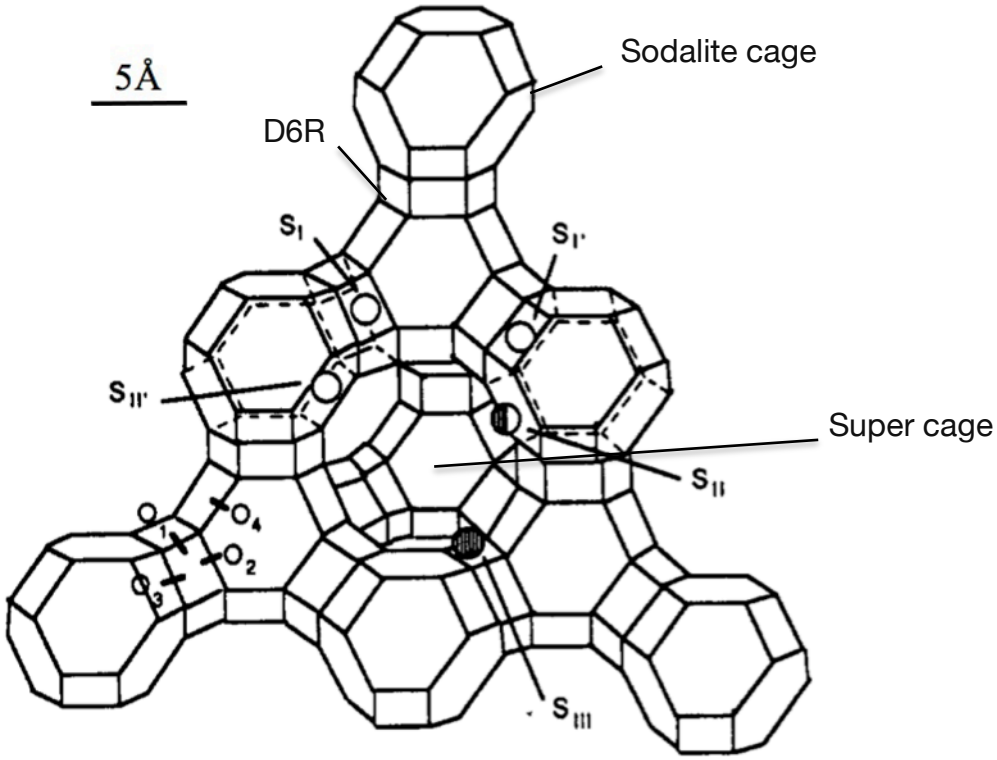

Fig. 1.4 Structure of zeolite Y showing sodalite cages (9.4 Å) connected by D6R (7.4 Å), generating a large super cage (11.8 Å) [*21*].

1.1.3. Ion exchanged Zeolite Y

The ion exchange of zeolite Y involves the charge compensating Na^+ cations in the structure. The new cation can substitute for Na^+ in the super cages, sodalite cages and D6Rs. The ratio of the replacement is governed by the concentration of the exchange ion in the solution and its valence *z*. The exchanged ion will not only replace the position of the Na^+ but can also cause changes in the cation positions moving to a more central place or a place closer to the edge in the cages depending on its size and valence.

1.2. Glass

Glass is one of the earliest materials manufactured by human beings [*22*] dating back to 5000BC where Phoenicians found it in the embers of wood fire. Humans started to make objects from glass in about 3000BC. Until 1500BC glasses were produced separately from ceramics which were formed by sintering crystalline materials. Glass bottles thousands of years old can be seen in museums, which show the cleverness of ancient people in using glass. At first glass was moulded into bottle shapes, later the Romans discovered how to blow glass into vessels of different shapes. The glass compositions then were a little bit different from modern glasses, for they were always obtained by melting sand and plant ashes or soda ashes to get Na_2O-K_2O-SiO_2. These kinds of glass are not so pure. In modern times, our glass production is much more stable and pure. For example the universal glass composition for window material is 69-74% silica + 5-14% sodium oxide (Na_2O) + 10-16% lime (CaO) + magnesia (MgO) + alumina (Al_2O_3). Glass has become an intense study field of research in the last hundred years. These studies differ in raw materials, glass forming mechanisms and different applications.

Glasses are defined as non-crystalline amorphous solids. The arrangement of the atoms and ions is so random that sometimes they are described as a frozen liquid, which means glasses are solids which have the structure of liquids frozen. These solids benefit from large entropy as they are fabricated with high energy, but this means that they are relatively unstable both mechanically and thermodynamically. As

most of the energy comes from the residual strain left in glass during cooling, this produces lots of wanted and unwanted effects. For instance, Prince Rupert's Drops are glasses with very high internal residual strain that are hard to break in the head by a hammer [*23*]. They are formed by dipping molten glass into cold water. However when a Prince Rupert's drop is slightly damaged in the tail it will explode into powder and flakes. (Fig. 1.5) Thermal toughening has been used in tempered glass for architecture and vehicle window glass to create a tough barrier that is also transparent.

Fig. 1.5 Prince Rupert's Drops showing drop with a large tail (left) which if broken destabilizes the whole specimen (right) [*24*]

1.2.1. Glass transition and various ways to form glass

After all those years' research in to glass, scientists have discovered many ways to form glass, its raw materials differ from liquid to crystal. All these methods are in

order to make the structure amorphous. The different ways is shown in Fig. 1.6

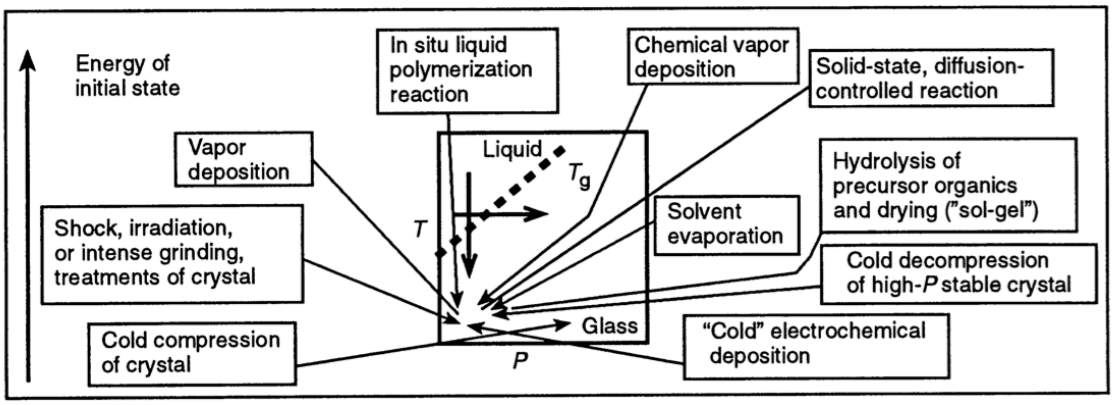

Fig. 1.6 Various routes to the glassy state collated from reference [*25*]

This figure schematically indicates a wide variety of ways of forming amorphous materials. In the center, the temperature-pressure (P-T) diagram indicates melt quenching from the liquid to the glassy state. The energies of the initial states relative to the final glassy states are also shown [*25*]. The basic conditions that change in this figure are the temperature and pressure, which may differ in application methods.

When it comes to forming glasses from liquids, cooling from high temperature is the most conventional way. This method was used widely in industrial production such as producing window glass and other functional glass [*26*]. Sometimes liquid polymerization reaction can also be used at ambient temperature and pressure to form glass, for example, polymerization of monomer liquid to form glassy materials [*27, 28*].

In some circumstances glass may be formed directly from gaseous pre-cursors, an example of this technique is in the widely used Chemical Vapour Deposition (CVD) of thin films of glassy materials, such as silica [*29*]. In the case of silica, one commonly used precursor is Silane (SiH4) which is reacted with Oxygen to deposit silicon dioxide (SiO2) on a substrate [*30*]. There are many variations of this technique, some of the notable variants carry out the deposition at low pressure (LPCVD) [*31*]or use a plasma to activate the pre-cursors (PECVD) [*32*]

Another way to form glass comes from the raw crystalline material. Almost all crystallites can be transformed into glass by cold compression [*33*], shock [*34*], irradiation [*35*] or intense grinding [*36*], even through the temperature for these techniques is low, high energy and high entropy glassy state can still be achieved by applying pressure and radiation to the raw materials. A ball milling maybe needed to form finely powdered glass from crystalline starting material as a kind of intense grinding [*37*]. Compression can be conducted under high pressure at ambient temperature in diamond anvil cell [*38*].

The right part of the diagram shows techniques which combine pressure with temperature to break the balance of the reaction in order to achieve a glassy state in a similar manner to quenching. In solid-state diffusion controlled reaction, solids reacted to form glass with high temperature diffusion. For example, an amorphous alloy can be formed using solid-state diffusion from pure polycrystalline Au and La

thin films [*39*]. Solvent evaporation to form glass can happen when the solute is unable to crystalize under solvent evaporation. Combined with levitation solvent evaporation can be used to study the amorphization of drugs [*40*].

The sol-gel route is another way for glass formation which is widely used recent years. Hydrolysis of precursor organics and drying uses the principal of homogenizing, for example, silver containing and silver free $Na_2O{\cdot}CaO{\cdot}2SiO_2$ glasses can prepared by sol–gel synthesis using tetramethil orthosilicate, sodium ethoxide, calcium nitrate tetrahydrate and silver nitrate as starting materials and methyl ethyl ketone as solvent [*41*].

The decompression from stable high pressure crystalline phase can form glass at ambient temperature. This is proved by decompressing $CaSiO_3$ and $MgSiO_3$ perovskites from their high pressure stability fields [*42*]. The various route of forming glass below T_g may yield glasses that are thermodynamically distinct from those obtained by the other high temperature routes but which may transform to them by way of non-equilibrium transitions. The difficulty of generating high temperature over a reasonable volume means that this route is not used much.

Even though so many methods have been introduced, the common method of glass formation used industrially is still cooling from a viscous liquid. By cooling a liquid rapidly from a temperature above the melting point T_m to a temperature at which the

crystalline structure is lost, one can bypass the recrystallization of the liquids as it is cooled by this way, the relaxation time becoming extremely long to point where it is beyond observation. For example, in the production of silicate glass, the molten liquid is quenched from 1500K. The amorphous structure of the molten material is frozen to where the equilibrium is broken on cooling. The temperature when the original structure is lost is called T_f, which is fictive and changes with the speed of cooling. The Energy/ entropy/volume-temperature curve around T_f is called glass transition area [*1*]. (Fig. 1.7)

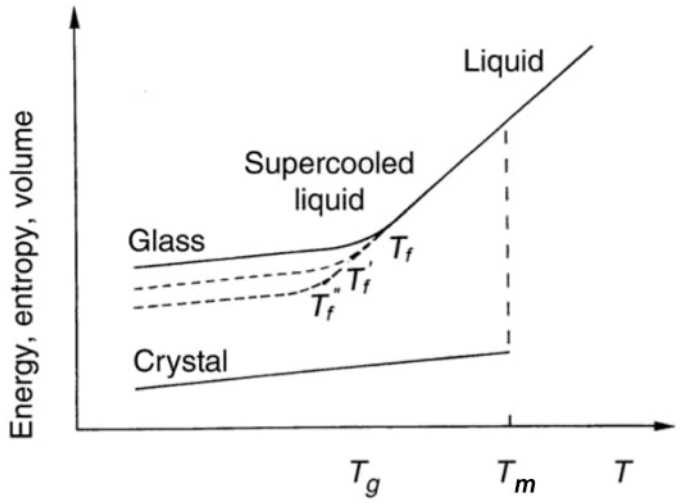

Fig. 1.7 Schematics for the liquid, supercooled liquid, glassy and crystalline states where T_m and T_g denote the melting point of the crystal and glass-transition temperature of the liquid, respectively. Taken from ref [*1*].

1.2.2. Different glass forming systems and amorphized materials

Glasses are amazingly wide used by mankind, ranging from oxide glass and

chalcogenide glass to metallic glass. Oxide glasses hold a most important position in our daily life, for example windows, display screens, windscreens, bottles etc. While chalcogenide glass and metallic glass represent the functional glasses used nowadays, e.g. infrared optics[*43*], low loss transformers[*44*], mechanically resistant cases for mobiles [*45*]etc.

1.2.2.1. Oxide glass

Coming to oxide glasses, these are silicate, borate and phosphate glasses. The principal ingredients of silicate glass is SiO_2, network-modifying alkalis such as Na and K are added to achieve glass formation at lower temperature. In silica, Si atoms are surrounded by four bridging O atoms, as explained in Zachariasen model of SiO_2 glass [*3*] (Fig. 1.8). In silicate glass Si atoms can be surrounded by one, two, three, or four bridging O atoms. The charge caused by non-bridging oxygens is compensated by the alkali or alkaline earth ion (network modifier) added. The structural and chemical local order characterized by various types of Si environment can be described as Q^n species, where n is between 0 to 4 and represents the number of bridging O surrounded Si. These are illustrated in Fig. 1.9, with the fractions expected for each Q^n species and two model distributions according to the composition of the network modifier. The binary model is based on the reaction:$2Q^n=Q^{n-1}+Q^{n+1}$, and there can be only one Q^n species at any stoichiometric composition and only two species elsewhere. For a random distribution model Q^n covers a broader composition, with three or four species exist which close to reality.

If the modifier is Na_2O and CaO, soda-lime-silica glass can be produced. This kind of glass occupies almost 90% of the glass production, as they can be used as windows, phone screens, containers and so on. Aluminosilicate glasses are formed by the addition of Al_2O_3, applied widely in bulb and glass fiber products. If PbO is added, lead glass is formed which has a high index of refraction and was originally used for decorative purposes and optical instruments. It was originally used to form a high reflective index glass for decoration and optical instrument. The lead also give the glass the property that it is highly absorbing of X-rays and γ -rays. The content of SiO_2 in silicate glass is over 99%, making it important in telecommunication, where fibres coated by high reflective index (GeO_2 + SiO_2) film, totally lossless reflect signals for km [*46*].

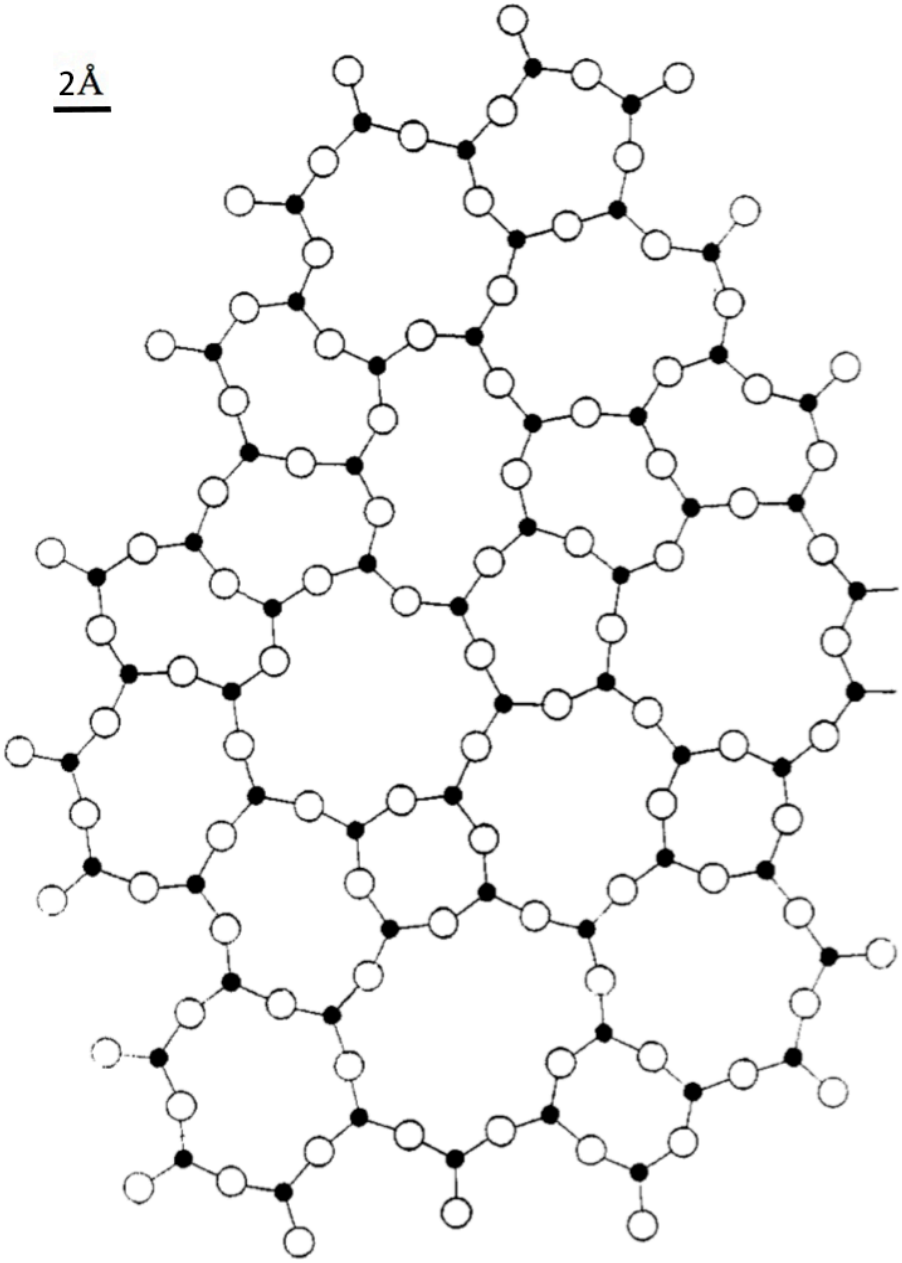

Fig. 1.8 The glass network of silica in two dimensions, in which black balls are Si, and white balls are O. [*3*]

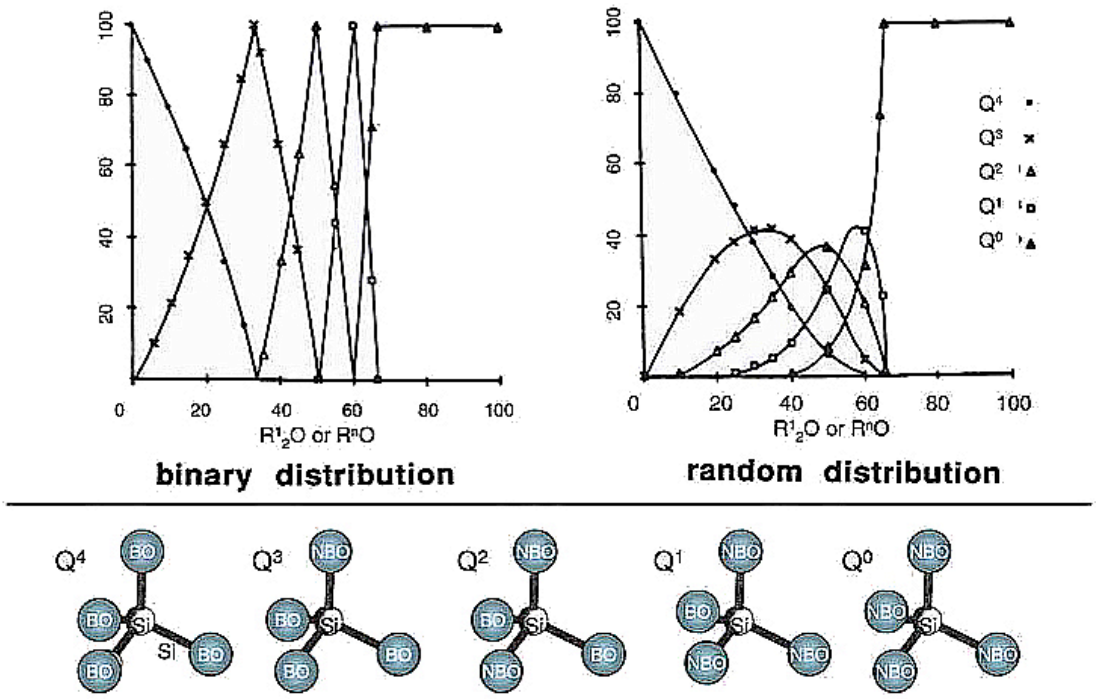

Fig. 1.9 Theoretical Q species distribution in binary alkali/alkaline-earth silicate glasses expected from a chemically ordered binary model (left) and from a random model (right). Different Q^n configurations are shown below [*1*].

B_2O_3 is the basic composition of the borate glass, however pure B_2O_3 glass is so chemically unstable, that it cannot be used in daily life. Borate glass normally used is a combination of borate and silicate glass. Pure borate glass can tell a lot about the structure of borosilicate glass. It consists of many planar B_3O_6 boroxol rings made by three O bridging BO_3 triangles. Borosilicate glass can be used for nuclear waste disposal [*47*].

Phosphate glass shows similar network structure to silicate glasses, but incorporates

polyphosphate chains. Because phosphate melts have high solubility for heavy ions and a low glass transition temperature, they can be used for nuclear waste disposal [*47*]. In telecommunications phosphate containing rare earths are used as optical amplifiers for optical fibre repeaters [*48*].

1.2.2.2. Chalcogenide glasses and halide glasses

Chalcogenide glasses and halide glasses can be achieved by replacing the oxygen in the oxide glass by sulfides, selenides, tellurides or halogens like fluorine. They show structural similarities with oxide glass because they are networks. However, chalcogenide glasses are semiconducting and are under development for non-volatile random access memories because they can transform from insulator glass to metallic glass and back under different heating conditions. Halide glasses have a high refraction index and can be used in optical instruments. They have superior optical transmission to silicate glass [*49*].

1.2.2.3. Metallic glass

Metallic glasses were first introduced by Kramer in 1930s using the vapour deposition method. (Fig. 1.6) Molten metals need very high speed cooling to achieve glassy state, as metals are so easy to crystalize. Metallic glasses have the advantage of both glass and crystalline metal. They are mechanically tougher than oxide glass and less easily deformed like crystalline metal. One commercial application of metallic glass is its use for golf clubs [*45*]. Metallic glass is also used in the core of transformers provides

a significant reduction in iron losses, compared with grain-oriented silicon steels.

1.3. Amorphization

Amorphization is the transformation from a crystalline phase to an amorphous (non-crystalline) phase without melting or vitrification, e.g. cold compressions in Fig. 1.6. It describes the process of a crystal structure changing under pressure and temperature. It is different from glass formation from raw materials by melting and melt quenching, but in techniques they have some similarities. Amorphization can also be achieved by shock, irradiation or intense grinding (Section 1.2.1).

1.3.1. Amorphization process

Amorphization can generally be obtained by pressure or temperature. When temperature is used in amorphization, it is usually below the melting temperature T_m and around the glass transition T_g. (Fig. 1.7) which means it is a solid reaction. Not all materials can be amorphized by thermal methods, as many crystals generally melt. However many materials do amorphize before melting, the most obvious examples are zeolites under temperature and quartz under pressure. D. Wolf et al have made some comparison in thermodynamics between solid-state amorphization and melting, showing some similarities while also explaining it by volume expansion [*51*]. Solid state amorphization was called mechanical melting according to this paper. Thermal decompressive amorphization was also reported by Skinner and Fahey in forming stishovite from silica under high pressure [*52*].

Apart from temperature, pressure induced amorphization (PIA) is the most frequent way used to get the amorphous state without melting. PIA was first reported by Mishima et al. [*53*] in 1984 as they found that ice under 77K could be pressed leading to amorphous ice. Since then, scientists kept discovering amorphization in different materials, like quartz, zeolite and other minerals. The amorphization can be obtained by pressure under different temperatures, but mostly room temperature. Consisting of SiO_2, quartz has been studied by many researchers looking at its structure and molecular dynamics. It is believed that amorphization has a relation to the density of the precursor materials, for example zeolite (~1.5 $g \cdot cm^{-3}$) can be amorphized under 5-10GPa while silica (~ 2.65 $g \cdot cm^{-3}$) needs 25GPa or higher.

Amorphization may also be induced by radiation and beams of ions, neutrons or electrons. Schwarz and Johnson give several examples of minerals amorphized by irradiation and mechanical methods in 1988 [*50*].

Ball milling is another method for obtaining amorphization, whose mechanism is the combination of temperature and pressure. The temperature comes from the friction while the pressure come from the strikes. Together influence is added to the specimen.

1.3.2. Potential application

Amorphous framework materials have a promising prospect in drug encapsulation as

the framework can prevent the drug from losing its activity but allow a relatively slow release. C. Orellana-Tavra etc. showed that the amorphous metal-organic framework can slow the drug release considerably compared to the crystalline framework [*54*]. Amorphization can be used to control the pore size of the encapsulating materials and hence the drug release rate. As a lot of materials have a good solubility for heavy ions, for example borate materials, amorphization is also promising method for the nuclear waste disposal. Amorphous ice can be used in scientific experiments to stabilize proteins for low temperature crystallization. For example, single molecules can be retained having a similar state in amorphous ice to that in liquid water at room temperature, which can maintain bioactivity. The liquid-glass transition offers a model for many other experiments, including study of organic compounds, or drug structure. In a word, the application of amorphous materials is promising, however it still needs efforts to discover and understand more.

To make these applications possible and achieve a deeper understanding of zeolite Y, ion exchanged zeolite Y, their amorphization and glass formation process were studied in this thesis. Techniques such as differential scanning calorimetry (DSC), X-ray powder diffraction (XRPD), high resolution X-ray powder diffraction (HRXRPD), inductively coupled plasma mass spectrometry (ICP-MS), Raman spectroscopy and neutron scattering are used. The details are illustrated in following section. The structure and dynamic information is analyzed too, including the changes caused by the exchanged ion in crystalline zeolite Y and amorphous zeolite Y.

1.4. References

1. G. N. Greaves and S.Sen, "Inorganic glasses, glass-forming liquids and amorphizing solids". *Advances in Physics* 56, 1 (2007).
2. C. A. Angell, "Formation of glasses from liquids and biopolymers". *Science* 267, 1924 (1995).
3. W. H. Zachariasen, "The atomic arrangement in glass". *J. Am. Chem. Soc.* 54, 3841 (1932).
4. H. V. Koningsveld, "Compendium of Zeolite Framework Types: Building Schemes and Type Characteristics". *Elsevier*, (2007).
5. G. N. Greaves, L. M. Colyer, A. J. Dent, K. K. Fox, S. W. Carr and R.H. Jones, "In situ study of ceramic formation from Co2+ Cu2+ and Zn2+ exchanged zeolite-A using combined XRD/XAFS techniques". *Nucl. Instr. Meth. Phys. Res.* B97, 107 (1995).
6. L. M. Colyer, Univ. Keele (1996).
7. A. Dyer, *An Introduction to Zeolite Mocular Sieves*. (Wiley, New York, 1988).
8. C. Levelut, J. Haines, A. Isambert, P. Hebert, S. Kohara, D. A. Keen, T. Hammouda and D. Andrault, "Topologically ordered amorphous silica obtained from the collapsed siliceous zeolite, silicalite-1-F: a step toward "Perfect" glasses.". *J. Am. Chem. Soc.* 131, 12333 (2009).
9. S. Fuhrmann, T. Palenta, G. N. Greaves, W. Schwieger and L. Wondraczek "Thermal collapse and hierarchy of polymorphs in a faujasite-type zeolite and its analogous melt-quenched glass". *J. Chem. Phys.* 142, 084503 (2015).

10. C. Kittel, *Introduction to Solid State Physics, 8th Edition*. (Wiley, New York, 2004).

11. GIANT COVALENT STRUCTURES, http://www.chemguide.co.uk/atoms/structures/giantcov.html

12. A.Bravais, "Memoir on the systems formed by points regularly distributed on a plane or in space". *J. Ecole Polytech* 19, 1 (1850).

13. Bravais lattices in three dimensions, http://users.aber.ac.uk/ruw/teach/334/bravais.php

14. W. Opechowski, *Crystallographic and metacrystallographic groups*. (Elsevier Science Ltd, North-Holland, 1986).

15. B.E. Warren, *X-Ray Diffraction*. (Dover Publications, 2012).

16. B.D. Cullity and S.R. Stock, *Elements of X-ray Diffraction*. (Prentice Hall, 2001).

17. A. F. Cronstedt, "Natural zeolite and minerals". *Kongl Vetenskaps Academiens Handlingar Stockholm* 17, 120 (1756).

18. Structure, http://www.ch.ic.ac.uk/vchemlib/course/zeolite/structure.html

19. A. C. Dimian and G. Rothenberg A. A. Kiss, "Solid Acid Catalysts for Biodiesel Production –-Towards Sustainable Energy". *Advanced Synthesis and Catalysis* 348, 75 (2006).

20. M. I. Aroyo, Ed., *International Tables for Crystallography Volume A: Space-group symmetry*, vol. A (International Union of Crystallography, Chester, ed. 6, 2016), vol. A, 6.

21. C. R. A. Catlow E. Dooryhee, J. W. Couves, P. J. Maddox, J. M. Thomas, G. N. Greaves, A. T. Steel, and R. P. Townsend, "A Study of Cation Environment and Movement during Dehydration and Reduction of NickeCExchanged Zeolite Y by X-ray Absorption and Diffraction". *Jpounal of Physical Chemistry* 95, 4515 (1991).

22. J. E. Shelby, *Introduction to Glass Science and Technology*. (Royal Society of Chemistry, 2005).

23. C. Frank and J. W. Steeds L. Brodsley, "Prince Rupert's Drops". *Notes and Records of the Royal Society of London* 41, 1 (1986).

24. Prince Rupert's Drop, http://imgur.com/piHDHcC

25. C. A. Angell, "Formation of glass from liquids and biopolymer". *Science, New Series* 267, 1924 (2014).

26. F. V. N. Tooley, *The Handbook of Glass Manufacture: A Book of Reference for the Plant Executive, Technologist, and Engineer*. (Books for the Glass Industry Division, Ashlee Publishing Company, 1984).

27. K. L. Ngai, C. A. Angell, G. B. McKenna, P. F. McMillan and S. W. Martin,, "Relaxation in glassforming liquids and amorphous solids". *App. Phys.* 86, 3133 (2000).

28. J. Schwarcz, *The Right Chemistry: 108 Enlightening, Nutritious, Health-Conscious and Occasionally Bizarre Inquiries into the Science of Daily Life*. (Doubleday Canada, 2012).

29. H. O. Pierson, *Handbook of Chemical Vapor Depostion [i.e. Deposition] (CVD):*

Principles, Technology, and Applications. (Noyes Publications/William Andrew Pub., 1999).

30. G. E. Totten, K. Funatani and L. Xie, *Handbook of Metallurgical Process Design*. (CRC Press, 2004).
31. A. S. Turtsevich, O. Yu Nalivaiko and L. P. Anufriev, "LPCVD borophosphosilicate-glass films: Deposition and properties". *Russian Microelectronics* 36, 251 (2007/07/01, 2007).
32. J. L. He, M. H. Hon and L. C. Chang, "Properties of amorphous silicon carbide film deposited by PECVD on glass". *Materials Chemistry and Physics* 45, 43 (1996/07/01/, 1996).
33. M. S. Surinder and S. K. Sikka, "Pressure induced amorphization of materials". *Progress in Materials Science* 40, 1 (1996/01/01/, 1996).
34. A. J. Gratz, L. D. DeLoach, T. M. Clough and W. J. Nellis, "Shock Amorphization of Cristobalite". *Science* 259, 663 (1993).
35. Y. Limoge and A. Barbu, "Amorphization mechanism in metallic crystalline solids under irradiation". *Physical Review B* 30, 2212 (08/15/, 1984).
36. A. W. Weeber and H. Bakker, "Amorphization by ball milling. A review". *Physica B: Condensed Matter* 153, 93 (1988/10/01/, 1988).
37. A. De Gusseme J. F. Willart, S. Hemon, G. Odou, F.Danede and M.Descamps, "Direct crystal to glass transformation of trehalose induced by ball milling". *Solid State Communication* 119, 501 (2001).
38. A. Jayaraman, "Diamond anvil cell and high-pressure physical investigations".

Reviews of Modern Physics 55, 65 (01/01/, 1983).

39. R. B. Schwarz and W. L. Johnson, "Formation of an Amorphous Alloy by Solid-State Reaction of the Pure Polycrystalline Metals". *Physical Review Letters* 51, 415 (08/01/, 1983).

40. C. J. Benmore and J. K. R. Weber, "Amorphization of Molecular Liquids of Pharmaceutical Drugs by Acoustic Levitation". *Physical Review X* 1, 011004 (08/08/, 2011).

41. M. Catauro, M. G. Raucci, F. de Gaetano and A. Marotta, "Antibacterial and bioactive silver-containing Na2O·CaO·2SiO2 glass prepared by sol–gel method". *Journal of Materials Science: Materials in Medicine* 15, 831 (July 01, 2004).

42. A. Chizmeshya, M. Hemmati, G. H. Wolf, P. H. Poole, J. Shao and C. A. Angell, "Crystalline-amorphous transition in silicate perovskites". *Phys. Rev. B* 51, 14841 (1995).

43. A. R. Hilton, *Chalcogenide Glasses for Infrared Optics*. (McGraw-Hill Education, 2010).

44. B. W. Kennedy, *Energy Efficient Transformers*. (McGraw-Hill, 1998).

45. W. L. Johnson, "Bulk amorphous metal—An emerging engineering material". *JOM* 54, 40 (March 01, 2002).

46. D. L. Williams S.T. Davey, B.J. Ainslie, W.J.M. Rothwell and B. Wakefield "Optical gain spectrum of GeO2-SiO2 Raman fibre amplifiers". *Optoelectronics* 136, 301 (1989).

47. M.I. Ojovan and W. E. Lee, *An Introduction to Nuclear Waste Immobilisation*.

(Elsevier Science, 2013).

48. M. Karabulut, E. Melnik, R. Stefan, G. K. Marasinghe, C. S. Ray, C. R. Kurkjian and D. E. Day, "Mechanical and structural properties of phosphate glasses". *Journal of Non-Crystalline Solids* 288, 8 (2001/08/01/, 2001).
49. J. L. Adam and X. Zhang, *Chalcogenide Glasses: Preparation, Properties and Applications*. (Woodhead Publishing Limited, 2013).
50. W. L. Johnson and R. B. Schwarz, "Remarks on solid state amorphizing transformations". *Journal of Less Comon Metals* 140, 1 (1988).
51. D. Wolf and S. Yip, *Materials Interfaces: Atomic-level Structure and Properties*. (Springer Netherlands, 1992).
52. B. J. Skinener and J. J. Fahey, "Observations on the Inversion of Stishovite to Silica Glass ". *Journal of Geophisical Research* 68, 5595 (1963).
53. L. D. Calvert and E. Whalley O. Mishima, "'Melting ice' I at 77 K and 10 kbar: a new method of making amorphous solids". *Nature* 310, 393 (1984).
54. S. A. Mercado and D. Fairen-Jimenez C. Orellana-Tavra, "Endocytosis Mechanism of Nano Metal-Organic Frameworks for Drug Delivery". *Advanced Healthcare Materials* 5, 2261 (2016).

2. Methodology

2.1. Ion exchange

2.1.1. Ion exchange

As mentioned in the first chapter, ion exchange is a very important property of zeolites because the cations in the cages show weak connection to the AlO_4^- tetrahedra. This leads to the freedom of the cations in the cages. The capability of the ion exchange is usually decided by the ratio of Si/Al, the size of the cages, and the position and property of the cations. If the ratio of Si/Al is high, there are less cations needed to compensate the charges. A cation bigger than the channels will be prevented from entering a cage. Moreover, the position of the cation is easy to explain for certain samples, but it is hard to explain how the exchanged ion might reach other SBUs. Some positions, for example super cages in Zeolite Y, will be more susceptible to exchange taking place. The exchange is selective for certain ions, this selectivity is not obvious for large cations however for small cations the ion exchange is easier. According to H. S. Sherry [*1*], when the exchange rate is low this preference is influenced by the radius of the hydrated compensating cation, the bigger the radius the lower the selectivity. However, when the exchange rate reaches a limit, which depends on the zeolite type, the exchange selectivity depends on the effect of free energy due to the interaction between the cations once dehydrated and the negatively charged lattice. Based on the same theory, M. Jeffroy et al [*2*] used Monte Carlo simulations to compute a model to calculate the univalent cation exchange isotherms in zeolites for cations like Li^+, Na^+, K^+.

The theories to describe the ion exchange in zeolites have been studied for several years. A. I. Kalinichev studied the dynamics of ion exchange from the selectivity of the ion and the influence of the solute concentration in 1996 [*3*]. It is very complex that the exchange rate comes from the influence of both selectivity and solute concentration, so Kalinichev showed the result in two nonlinear mass conservation formulas. In thermodynamics, R. T. Pabalan and F. P. Bertetti studied the model of the reaction of the solution and zeolite, and showed that the exchange solution can be achieved by analyzing the composition of the zeolite using thermodynamics [*4*]. This thermodynamics model is very useful in multi-cation systems.

There are several kinds of methods to complete ion exchange, including the solution exchange, the solid exchange and the molten salt exchange methods. The method most used and the easiest is the solution exchange method, which is the one adopted in this research.

2.1.2. Specimen preparation

In addition to zeolite Y, further samples were prepared by exchange of Na^{+} by Cu^{2+} and Nd^{3+} cations, as shown in table 2.1

Exchange Ion	Method
Cu^{2+}	Zeolite Y (20g) was dispersed into 400mL of water to make

	Liquid1. Cu $(NO_3)_2$ (4g) was dispersed into 5mL of water to make Liquid 2. Liquid 1 was mixed with Liquid 2, stirred for 24h. It was dried under 80℃. It was dissolved again into 400mL of water, and stirred for 24h It was dried again under 80℃. Sample was dried under 300℃ for 15h.
Nd^{3+}	Identical to exchange method for Cu^{2+}, except the exchange ion is Nd^{3+}.

Table 2.1 The solution method used in zeolite Y exchange

2.2. Research Techniques

During the course of this research, various analytic techniques were used, including powder diffraction using laboratory X-ray machine(XRPD), and high brightness synchrotron(SXPD), differential scanning calorimetry (DSC), mass spectroscopy, Raman spectroscopy and neutron scattering. The amorphization of interest of a transitional process (from crystalline to amorphous) of a bulk material. The above techniques were therefore chosen to study the structural and dynamical changes of the zeolite samples. These particle averaging techniques and their physics basis are described in details next.

2.2.1. X-ray Powder Diffraction

2.2.1.1. XRPD

Diffraction happens when waves of X-ray, neutron or electron pass through periodic crystalline lattices generating patterns. X-ray powder diffraction (XRPD) is a very common technique, and can give researchers information about the structure of materials when these patterns are analyzed and interpreted. When higher resolution is required, powerful synchrotron radiation is usually used which gives detailed information due to higher brightness however is a limited resource due to availability and high demand. High resolution X-ray powder diffraction (HR-XRPD) is therefore used to obtain structural details in complex crystal systems instead of laboratory XRPD.

2.2.1.2. Theory

X-rays are electromagnetic (EM) radiation similar to visible light however with shorter wavelength (~ 0.1-3.0 Å). When X-rays interact with an atom, the waves can be scattered by the electron cloud of the atom according to the EM theory [*5*]. When a monochromatic X-ray is incident upon a single crystal, it will be scattered by the regular arrangement of atoms or molecules in the crystal giving rise to interference of the waves. Just like a grating with visible single color light making dark and bright bands, the interference of the X-rays is known as “diffraction”.

If the crystal is oriented particularly referring to the beam and an imaging detector is

used, a pattern of bright spots can be caught, which is unique to the crystal structure. Fig. 2.1 shows a representation of a crystal lattice with the atoms in the lattice represented by black dots. An incoming x-ray beam will be reflected from all of the atoms in the lattice, with each atom in the lattice acting as a radiator. The path difference between waves reflected from adjacent crystal planes in the lattice causes constructive and destructive interference to occur. In the simplified representation shown in Fig 2.1, constructive interference will occur when the angle of incidence of the beam is such that the path length difference between crystal planes is equivalent to a whole number of wavelengths of the incident radiation. This difference in path length may be determined by simple trigonometry and gives rise to the Bragg's law formulation:

$2d_{hkl}sin\theta_B=\lambda$,

where d_{hkl} is interplanar distance, θ_B is scattering angle, λ is the wavelength of the X-rays. (Fig. 2.1)

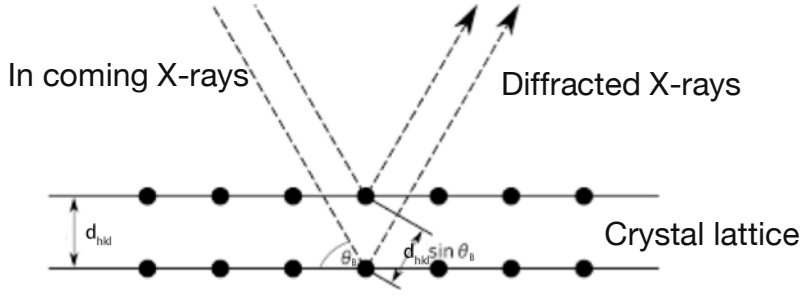

Fig. 2.1 Schematic incoming X-rays scattered into particular directions determined by the crystal lattice spacing [*6*]

The interference pattern is produced in reciprocal space and may be used to determine

the real space structure of a crystalline sample, using techniques like Rietveld refinement(details in section 2.3.1).

In the reality the planes are actually present in three dimensions, so the definition of the planes use the Miller indices (Fig. 2.2). The axis is usually defined in the direction of the lattice vectors a, b, c, as shown Fig. 1.2 in chapter 1, α, β, γ are the angles between the three unit vectors. The Miller index (*h,k,l*) is defined as the reciprocal of the intersection with each axis.

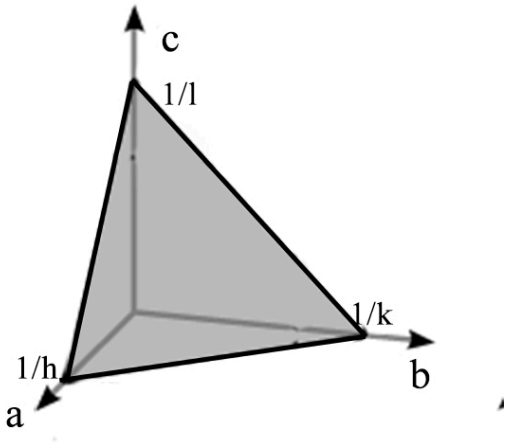

Fig. 2.2 Miller index *h, k, l* coordinates in reciprocal space

Each real space interplanar distance d_{hkl} is defined in terms of *h, k, l*, the coordinates in reciprocal space. The formula is $d_{hkl} = \frac{2\pi}{|ha+kb+lc|}$

The lattice spacing d_{hkl} can be defined as:

Cubic system: $\frac{1}{d_{hkl}^2} = \frac{h^2+k^2+l^2}{a^2}$

Tetragonal system: $\frac{1}{d_{hkl}^2} = \frac{h^2+k^2}{a^2} + \frac{l^2}{c^2}$

Orthorhombic system: $\frac{1}{d_{hkl}^2} = \frac{h^2}{a^2} + \frac{k^2}{b^2} + \frac{l^2}{c^2}$

In the other systems the angle parameter α, β, γ also needs to be incorporated. In these cases expressions for d_{hkl} will be much more complex, but are given in elementary crystallography text books [*7*]. Zeolite Y in this study has a cubic system.

The Bragg's equation is useful to index diffraction peaks or reflections leading to the determination of crystal lattice and symmetry. However, the intensities for all the measured Bragg peaks from a sample are very important to determine structural details (atomic coordinates, temperature factors and occupancies) [*8*]. The intensity (I) can be predicted as:

$I_{hkl} = k\,|F_{hkl}|^2\, e^{-2M}\, p\,[LP]\, A(\theta)$

k is scaling constant,

F_{hkl} is structure factor,

e^{-2M} is temperature term, where $M = Bn(\sin\theta_B/\lambda)^2$ and B_n is the isotropic temperature factor (Debye-Waller) of atom *n*,

p is multiplicity factor

LP is Lorentz-polarisation factor (geometric)

$A(\theta)$ is absorption factor of the sample.

The structure factor, F_{hkl} is given by the following depends upon the atomic position (r_n) and $r_n = x_n a + y_n b + z_n c$,

where x_n, y_n and z_n are the fractional coordinates in a, b and c lattice parameters, respectively. Therefore,

$$F_{hkl} = \sum_n f_n \, g_n e^{2\pi \cdot i(hx_n + ky_n + lz_n)}$$

where f_n $(= f_o + f' + if'')$ is the atomic scattering factor and g_n is the site occupancy factor.

XRPD combined with Rietveld refinement, especially when using powerful synchrotron X-ray beam, can reveal small details in the microporous structures of zeolites including atomic parameters: fractional atomic coordinates, site occupancy, and atomic displacement or temperature factor.

In a powder diffraction pattern, the 3-D diffraction information is condensed to a single direction. Therefore, multiplicity factor (p) arises from the sets of hkl planes which have identical d-spacing due to symmetry. For example, the d-spacing of (1,0,0), (0,1,0), (0,0,1), (-1,0,0), (0,-1,0), and (0,0,-1) peaks in a cubic lattice are the same and p=6. Whereas (111) has 8 identical peaks giving p=8. Therefore, the Bragg peak intensity must calculated including the multiplicity of the corresponding *hkl*

plane. In addition, some planes overlap but possess different structure factors. For example, in a cubic lattice the 511 and 333 reflections possess identical lattice d-spacing. As the Rietveld refinement is a whole pattern fitting technique that involves all the structural parameters, when the peak intensity is calculated, the overlapped Bragg peaks can be accounted for.

In order to get the structural information of a single crystal from every orientation, the sample needs to be rotated for the measurement of intensities from the different d-spacings. However, in an ideal powder specimen, there are hundred thousands to millions of tiny crystallites. The distribution of every orientation should be equal, so for a given interplanar distance d there will be a number of crystallites at the right orientation, giving rise to a small bright spot. All these spots combine together to form a bright ring, called the Debye-Scherrer ring [*5*]. Different Debye-Scherrer rings for different d-spacings are shown on Fig. 2.3, in which d_1, d_2 represent different interplanar distances.

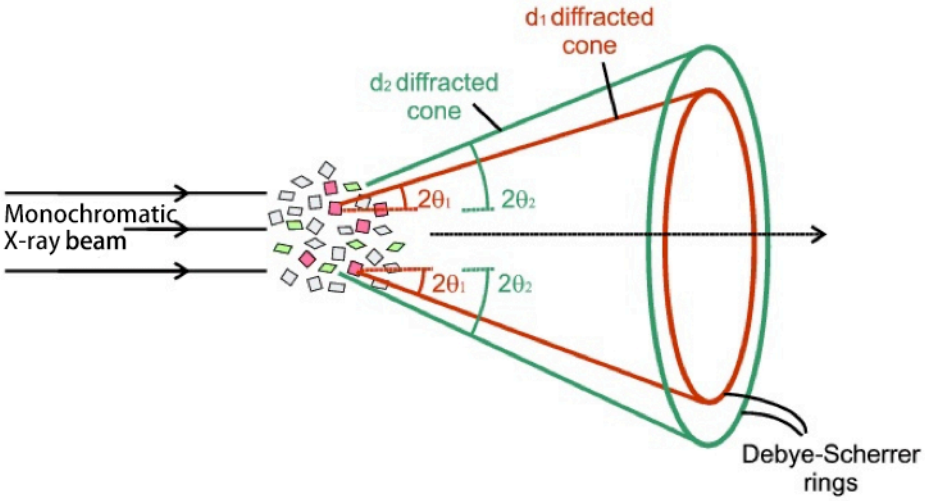

Fig. 2.3 Diffraction from a crystalline powder showing the different Debye-Scherrer rings[*9*]

Samples for powder diffraction need to be isotropic to make sure every crystalline orientation possible is represented equally. This is done by grinding powder to micron size crystallites.

2.2.1.3. HR-XRPD

The principle of HR-XRPD is the same as XRPD [*10*]. However, the high resolution technique usually exploits powerful X-ray beam produced from a synchrotron radiation (SR) machine[*11*]. The first such SR instruments were developed more than two decades ago [*12* - *14*]. There are a number of advantages using a SR beam for XRPD when comparing with a laboratory X-ray set:

a) High brightness (intense and highly collimation) means: (i) smaller angular divergence of the incident beam, hence high angular resolution data can be obtained, and (ii) deep probing of structural details with high contrast (high signal-to noise ratio) data for the detection of small features.

b) Tuneable X-ray wavelength: (i) fluorescence occurs if the incident energy is above the absorption edge of one of the elements in the crystal lattice, this fluorescence cause high background and may be avoided by using lower energies. (ii) tuneable X-ray may be used to deliberately tune to absorption edges for resonant diffraction, i.e. to enhance the electronic contrast between neighbouring elements in a lattice such as Cu and Zn.

c) Large or spacious instrument for sample environments means non-ambient or in situ experiments are routinely conducted.

The collection of optical components to select a particular wavelength of radiation from the synchrotron, shape the beam and focus it onto a sample together with the associated radiation containment hutches are referred to as a beamline. The 1st hutch (from the source) houses optic components such as monochromator and mirrors to deliver a highly collimated and intense (high brightness) beam to the sample. In the 2nd or experimental hutch on the beamline used for these experiments (DLS I11), there is a heavy duty, high precision diffractometer, designed to provide excellent angular precision (~0.1mdeg). The diffractometer has two-circles; the small θ for the mounting of sample stage such as sample spinner and the large 2θ for the mounting of detection system. Spinning capillary sample at the centre of the θ-circle is used for two important reasons. First, the preferred orientation of crystallites is less of a problem and secondly, a rotating sample can bring more crystallites to diffraction conditions.

The instrumental resolution can be further improved by installing an analysing crystal (Si 111 or Ge 111) on the 2θ-circle, between the sample and detector. The perfect crystal has very narrow acceptance angle for diffraction (a few mdeg. at 12.4 keV or λ~1 Å) and it only allows certain radiation at correct energy (a pre-set Bragg angle) to pass through and reach the detector. Although high resolution data can be obtained by scanning 2θ, the collection time can take quite some time for good statistic due the narrow bandpass of the crystal and its attenuation. To decrease data collection time, multi-analysing crystals (MAC) are used, ranging from several to many such as the designs of beamline ID22 (formerly ID31) [*15*] at the European Synchrotron Radiation Facility (France), 11BM beamline at the Advanced Photon Source (USA) [*16*] and beamline I11 [*17*] at Diamond Light Source (UK).

The HR-XRPD measurements were carried out using the facility at Diamond Light Source on beamline I11and the experimental hutch is shown in Fig.2.4

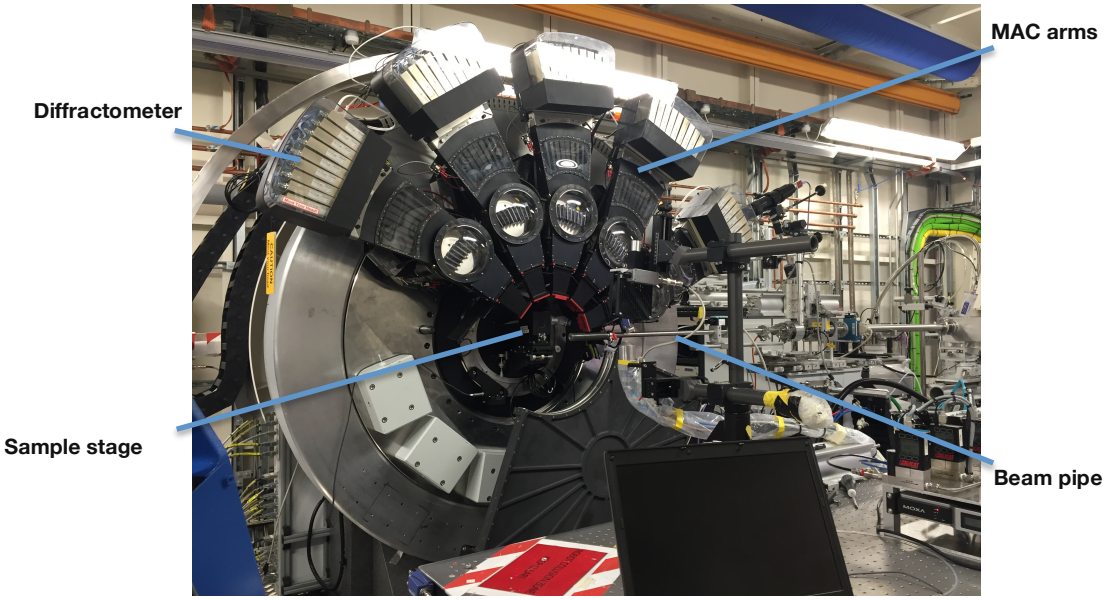

Fig. 2.4 A photograph of beamline I11 at Diamond Light Source, UK

The large instrument has MAC of Si111 to provide tight collimation of the diffracted beams on the 5 arms surrounding the powder sample loaded in a capillary (Fig. 2.5) for the collection of high resolution data. The X-ray optics on the beamline use a Si111 monochromator to filter out a single wavelength (optimised at 15 keV~ λ =0.826 Å) which comes out from the beam pipe and impinges on the sample.

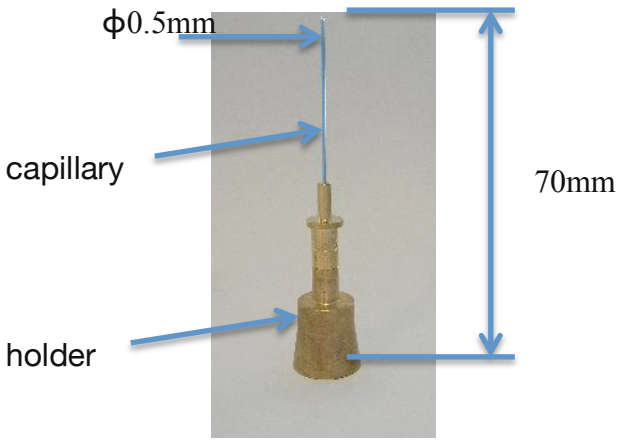

Fig. 2.5 A typical capillary sample with the diameter 0.5mm, 0.01mm thickness and

length 70mm, showing the blue powder supported by a holder that is inserted into the control circle for diffraction

In order to randomize the specimen of micron sized crystallites further, the capillary container was spinning during the experiment. The powder sample was filled in the capillary as shown in Fig. 2.5. The capillary is mounted on the sample stage by a robotic sample changer. Each of the MAC arms contain 9 detectors, so there are altogether 45 detectors covering 3-150 degrees. The monochromatic beam comes out from beam pipe, was diffracted by the powder sample and the X-ray signals distributed in 2θ were recorded by the detectors. The final diffraction pattern of 2θ versus intensity was produced by the merging of all recorded data. This process is described in detail by Thompson et al (2009) [*17*].

Compared to other methods for detecting material atomic structure, HR-XRPD offers a more rapid way also with small quantities of powder. HR-XRPD uses a high brightness beam (intense and highly collimated) which gives it the advantages over conventional XRPD. With a good crystalline powder sample, the technique produces narrower peaks with good counting statistics obtained from relatively short measuring time. These are essential for detailed structural analysis.

As gaining access to HR-XRPD beamlines is not always possible, measurements using X-ray machine of laboratory setting is much easier. Therefore the approximate

structures of the zeolite samples were obtained using XRPD, while the high resolution of HR-XRPD was used to give detailed information about ion positions and possible movements. Both techniques were therefore used to detect the degree of amorphization in zeolite materials and ion positions at each stage.

The patterns of the zeolite samples obtained from I11 have been analyzed by Rietveld Refinement [*18*](available in software TOPAS), which can refine from an initial guessed atomic structure to fit the measured patterns.

2.2.2. DSC

Differential scanning calorimetry (DSC) is a thermal technique measuring the specific heat needed to raise the temperature of the sample to a set temperature [*19*]. If the heat flow is negative then the sample is giving out heat (exothermic), otherwise the sample is absorbing heat (endothermic). This kind of measurement can detect the melting point, phase changes, water loss and the glass transition temperature. All these changes have an obvious reffect in the heat exchange. According to these changes, different phases can be predicted.

The DSC machine is shown in Fig. 2.6. The heat flow is obtained by comparing the sample with respect to a reference.

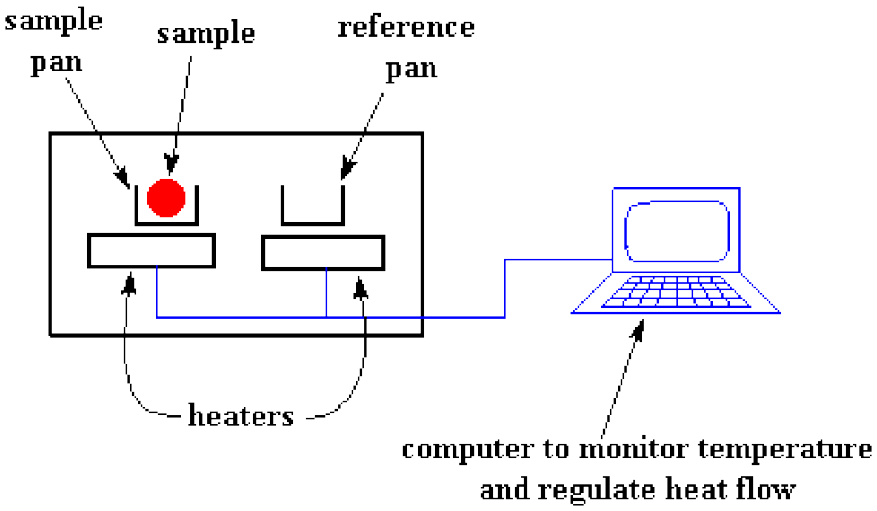

Fig. 2.6 Schematic of DSC instrument where heat flow in or out of the specimen is determined differentially with respect to a reference [*20*].

The output of the DSC reflects the heat difference changes taking place with time and/or temperature (Fig. 2.7). This diagram can be used to calculate enthalpies of transitions. The Enthalpy can be calculated by

$$\Delta H = KA$$

Where ΔH is the enthalpy of the transition, K is the colorimetric constant, A is the area under the curve. T_m for instance melting in the diagram defines as the transition temperature, for a phase change, for example the melting temperature T_m of the specimen

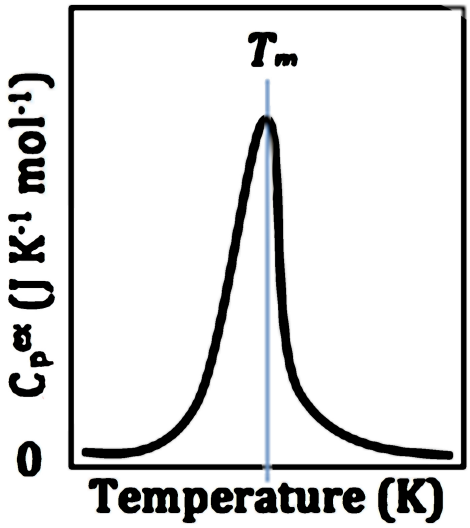

Fig. 2.7 DSC diagram showing a exothermic peak for melting [*21*]

DSC can be used in the study of zeolites to measure the glass transition temperature T_g, the melting point T_m and the water loss endotherm [*22*]. As shown in Chapter 1 Fig. 1.7, T_g represents the temperature where the glass transforms from a rigid solid to a supercooled liquid. In DSC, it is characterized by a broad endotherm. Zeolites can absorb large quantity of water in to the cages, the temperature of water loss is also very important to the study of zeolites and amorphization.

2.2.3. ICP-MS

Inductively coupled plasma mass spectrometry (ICP-MS) is a type of mass spectrometry which can detect the chemical composition of samples. The quantity of the sample can be very low. The principle of this technique was found by Eugen Goldstein in 1886 [*23*], when he observed rays from the anode travelling in a

discharged gas were in the opposite direction to the electron beam rays from the cathode when these passed through channels in cathode. So he named these rays “canal rays”. In 1899, Wilhelm Wien found that the deflection was caused by strong electric or magnetic fields, so he built a device to separate the canal rays according to the charge (Q)-to-mass of the ions ratio (Q/m) [*23*]. This device employs parallel electric and magnetic fields, and is the origin of ICP-MS devices used today.

In mass spectrometry, the sample can be ionized by different methods , sometimes it is bombarded by electrons to make the molecules break, sometimes it is dissolved into acid solution [*24*]. The starting sample can be solid, liquid or gas.

In ICP-MS the sample is ionized by a argon plasma, generated by an intense radio frequency field. The ionized sample is then introduced to the analysis chamber where a mass spectrometer separates the ions of the sample according to Q/m. Ions of the selected mass pass through the quadruple where they are detected by an electon multiplying detector. A schematic of typical ICP-MS is shown in Fig. 2.8.

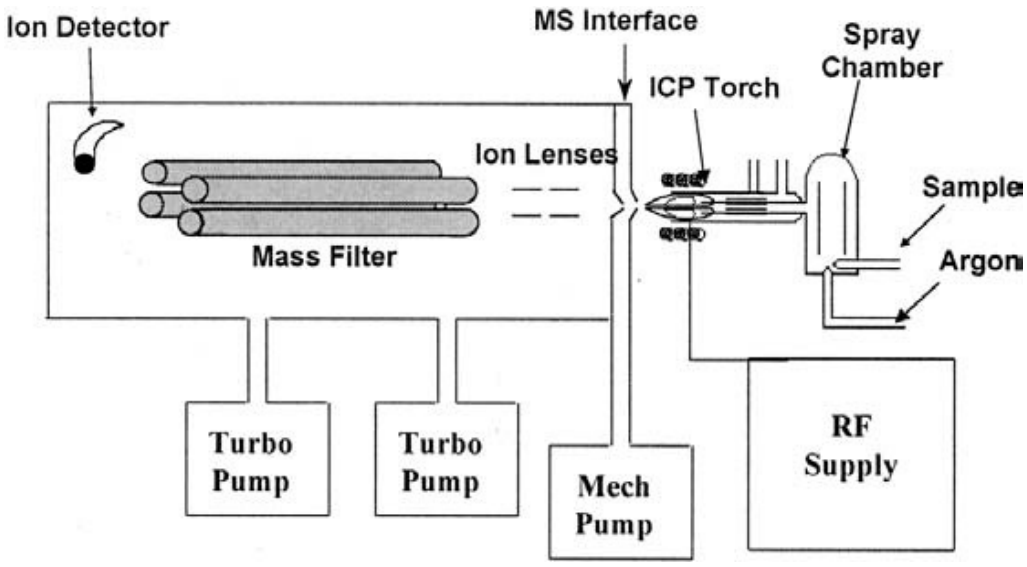

Fig. 2.8 ICP-MS to obtain chemical composition of zeolite samples. This shows the specimen injection, inductivity coupled plasma and mass spectrometer. [*25*]

2.2.4. Raman spectroscopy

Raman spectroscopy is a technique using laser light (usually in the near infrared or ultraviolet range) to detect the vibration, rotation and other dynamic behavior in specimens. This technique originates from the Raman effect found by Sir C. V. Raman in extended research on molecular light-scattering in 1928 [*26*]. He was awarded the Nobel Prize for this in 1930. At first, this technique was limited by its low sensitivity and poor monochromatic light in 1940s. However, the development of laser techniques in the 1960s brought improvement to these techniques. Now it is a standard lab technique to identify the structure of bonds and bond bending phenomenon in molecules and solids.

When monochromatic light is incident on a specimen, it will interact with the sample

causing inelastic scattering and elastic scattering [*27*].The energy change of this interaction is shown in Fig. 2.9. If the photons on collision with a molecule are elastically scattered, there is no energy change between them. This kind of elastic scattering is called Rayleigh scattering. However, some collisions, can be inelastic, which will result in energy exchange between the molecules and photons. The energy from the photons can transfer to molecules exciting them to higher energy levels or the vibration and rotation energy of the molecule can also transfer to photons (Fig. 2.10). The vibrational energy change will cause the energy of the radiated photons to change. The relationship between them is $E=h\upsilon$, where E is the energy of a photon, h is Planck's constant, and υ is the frequency of the photons. The change of the frequency $\Delta\upsilon$ is called Raman shift. When the energy of molecule's final state is higher than the initial state, the energy of the light will be lower ($\Delta\upsilon$ is negative), this shift is called Stokes Raman scattering. In the opposite cases where the energy of the final state is lower than the initial state, it would be called the Anti-Stokes Raman shift. Every Raman active substance has its unique spectrum, related to the vibration and rotational modes of molecules.

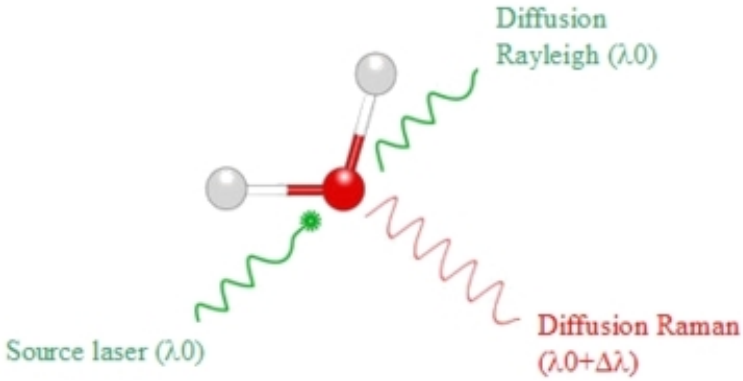

Fig.2.9 The energy changes in inelastic Raman Spectroscopy [*28*]

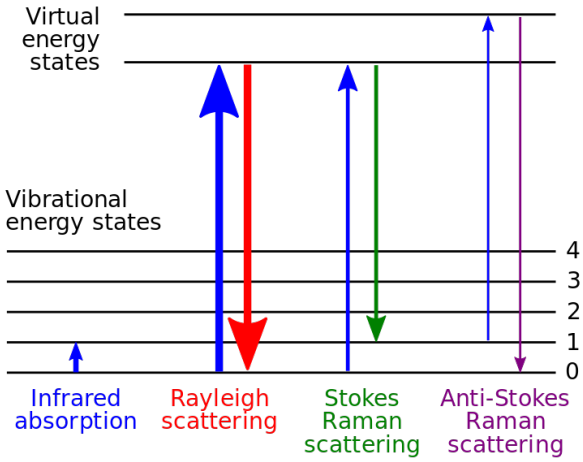

Fig. 2.10 The schematic of the energy changes in Raman spectroscopy [*29*]

Raman spectroscopy has been applied to zeolites in different states of amorphization to discover changes that take place during amorphization [*30*].

2.2.5. Neutron scattering

Elastic Neutron diffraction has similar principles to the X-Ray diffraction that complies with Bragg's Law. However, neutrons interact with the nucleus of an atom

whereas X-ray interact with the electron cloud surrounding the atom. This makes X-ray and neutron scattering complimentary techniques, in which neutron diffraction is more sensitive to some light elements for example water and has higher penetration. Inelastic Neutron scattering can study microscopic dynamics of the materials. The energy of the incident neutron can change by giving or receiving energies from the phonons like Raman spectroscopy. Inelastic neutron scattering can provide dynamic information in the structure, for example, the vibrational density of states (VDOS).

Inelastic neutron Scattering (INS) is usually used to study molecular motion as well as magnetic and excitations. Results are usually described in terms of the dynamic structure factor *S(Q, w)*, where *Q* is the difference between the incoming and outgoing neutron vector, *w* is the energy exchanged between them.

Inelastic scattering experiments normally require the wavelength of the incident and outgoing beams and an energy analysis of the scattered neutrons. This can be done through time-of-flight techniques [*30*].

2.3. Data analysis techniques

2.3.1. Rietveld Analysis

Rietveld refinement is a method developed by Hugo Rietveld to characterize crystalline structure[*31*]. It refines the material structure using the positions, intensity and width of the peaks from the scattering pattern. A least squares method is applied

to refine the calculated pattern for trial atomic positions to fit the measured pattern in order to obtain the precise atomic coordinates [*32*].

Principle of Rietveld Refinement

The theoretical intensity at point i of the diffraction diagram can be calculated by

$$y_{ic} = y_{ib} + \sum_{\Phi} S_{\Phi} \sum_{\Phi} G_{\Phi}(2\theta_i - 2\theta_k) I_k \ ,$$

GΦ: normalized profile shape function

I_k: intensity of the *kth* reflection

SΦ: scale factor of phase *Φ*. Summation performed over all phases *Φ*, and over all reflections k contributing to the respective point.

y_{ib}: background

y_{ic}: calculated intensity

I_k: The equation and parameters are given in section 2.2.1.2.

The goal of the refinement is to minimize the difference of the calculated pattern and the observed pattern using a least square method,

$$wss = \sum_i w_i \left(y_i^{obs} - y_i^{calc}\right)^2 , w_i = \frac{1}{y_i^{obs}},$$

wss: the difference of the intensity of the calculated pattern and the observed pattern

y_i^{obs}: observed intensity at the ith step

y_i^{calc}: calculated intensity at the ith step

$$w_i = \frac{1}{y_i^{obs}}$$

Quality of the refinement

For a well-fitted XRPD pattern, the difference between the observed and calculated patterns should be small or minimised, and no specific peaks should be poorly fitted. If there is any major peak discrepancy, it may suggest faults in the proposed model. Refinement factors or *R*-factors [*18*] to be described below are useful indicators for the evaluation of a refinement, especially in the case of small improvements to the model, but it should not be used as the final confirmation of the structure. The most important criteria for judging the quality of a Rietveld refinement are (i) the fit of the calculated pattern to the observed data and (ii) the chemical sense of the structural model. The former can be evaluated on the basis of the final profile plot and the latter on a careful examination of the final atomic parameters such as bond lengths, bond angles and site occupancies [*33*].

The *R*-factors can provide a more quantitative guidance over the quality of the fit, where the *R*-factor quantities are R_p, R_{wp}, R_{exp} and χ^2 or goodness-of-fit (g.o.f):

$$R_{wp} = \frac{\sum_i w_i (y_i^{obs} - y_i^{cal})^2}{\sum_i w_i (y_i^{obs})^2}$$

$$R_{wp} = \sqrt{\left(\frac{\sum_i w_i (y_i^{obs} - y_i^{cal})^2}{\sum_i w_i (y_i^{obs})^2} \right)}$$

$$R_p = \frac{\sum_i |(y_i^{obs} - y_i^{cal})|}{\sum_i y_i^{obs}}$$

$$R_{exp} = \sqrt{\left(\frac{n-p}{\sum_i w_i (y_i^{obs})^2}\right)}$$

$$\chi^2 = \frac{R_{wp}^2}{R_{exp}^2}$$

n = the number of observables of the data

p = the number of parameters of the refinement

y_i^{obs} = the experimental Bragg peak intensity

y_i^{cal} = the calculated Bragg peak intensity

w_i = the weighting coefficient at the i^{th} step (=$1/y_i^{obs}$)

The weighted profile, R_{wp} is the most significant as the numerator is the function being minimized. R_{exp} is the 'expected' R-factor when there are n observables and p parameters, which is the best possible value that the R_{wp} value could possibly reach. Adequate XRPD refinements generally have R_{wp} values below 12%, and χ^2 should approach 1 for an ideal refinement. As the number of peaks increases, it is more difficult to achieve low R_{wp} values. In general, for a highly symmetric structure (fewer Bragg peaks), R_{wp} < 8% is considered acceptable, and for a medium complex phase/structure, < 10% is good; for a complex system (i.e., monoclinic to triclinic), <

15% is acceptable. As for HR-XRPD data obtained from a synchrotron source, the R_{exp} values become less meaningful as the number of observables (n) is much greater than that of a laboratory X-ray analogue due to smaller 2θ step size (high resolution). Also the statistics of observed intensities (intense incident beam) are much higher and hence reducing the counting errors. These will lower the R_{exp} value and hence artificially raised the values of χ^2. Hence, the χ^2 value (or g.o.f.) should not be the only factor to judge the quality of the Rietveld refinement.

2.3.2. Structure determination during amorphization

Using the Rietveld refinement, the crystalline fraction was analyzed by subtracting the the amorphous background from the crystalline peaks[*18*]. The degree of amorphization at each stage was calculated from the integrated peak intensities using the following formula,

$$A\% = \left(1 - \frac{a_{cp}}{a_{al}}\right) 100\%$$

where a_{cp} is the area of the crystalline peaks in the pattern after the background subtraction, a_{al} is the area of all the peaks in the pattern. [*34*]

Using the calculation of an XRPD result for example in Fig. 2.11, the peak separation is illustrated by removing the amorphous background.

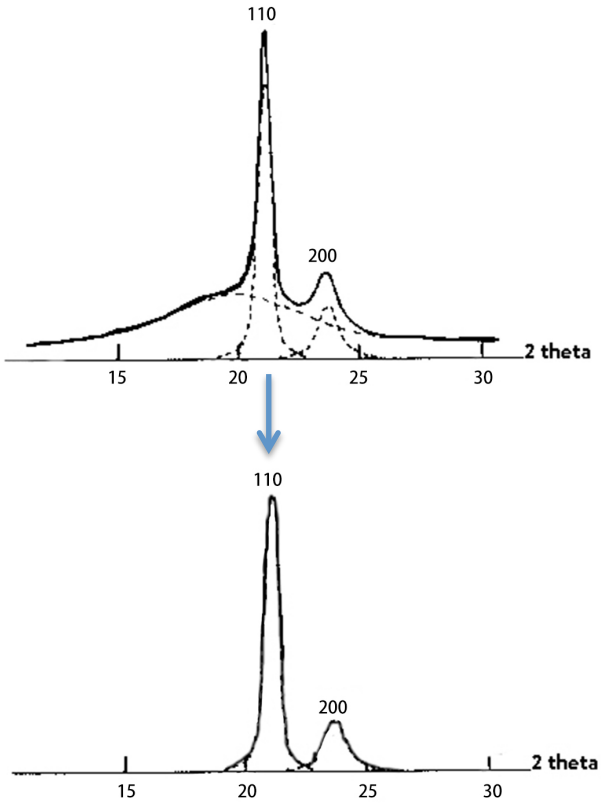

Fig. 2.11 The process of peak separation

2.4. Heat treatment for progressive amorphization

In order to prepare samples exploring collapse, various heat treatments were applied using a furnace and are detailed in following chapters 3 and 4.

2.5. References

1. H. S. Sherry, "The Ion-Exchange Properties of Zeolites. I. Univalent Ion Exchange in Synthetic Faujasite". *J. Phys. Chem* 74, 1158 (1966).
2. M. Jeffroy, A. Boutin and A. H. Fuchs, "Understanding the Equilibrium Ion Exchange Properties in Faujasite Zeolite from Monte Carlo Simulations". *J. Phys. Chem* 115, 15059 (2011).

3. A. I. Kalinichev, "Nonlinear Theory of Multicomponent Dynamics of Sorption and Chromatography". *Usp. Khim.* 65, 103 (1996, 1996).
4. R. T. Pabalan and F.P.Berterri, "Thermodynamics of Ion-Exchange Between Na+/Sr2+ Solutions and the Zeolite Mineral Cinoptilolite". *MRS* 333, 731 (1993).
5. D. M. Moore and R. C. Reynolds, *X-ray diffraction and the identification and analysis of clay minerals*. (Oxford University Press, Oxford, 1997).
6. Bragg's law, https://en.wikipedia.org/wiki/Bragg%27s_law
7. B.D. Cullity and S.R. Stock, *Elements of X-ray Diffraction*. (Prentice Hall, 2001).
8. B.E. Warren, *X-Ray Diffraction*. (Dover Publications, 2012).
9. Powder Diffraction, http://pd.chem.ucl.ac.uk/pdnn/diff2/kinemat2.htm
10. S. P. Thompson, J. E. Parker, J. Potter, T. P. Hill, A. Birt, T. M. Cobb, F. Yuan and C. C. Tang, "Beamline I11 at Diamond: A new instrument for high resolution powder diffraction". *Review of Scientific Instruments* 80, 075107 (2009).
11. P. Willmott, *An Introduction to Synchrotron Radiation: Techniques and Applications*. (Wiley, 2011).
12. J. B. Hastings, W. Thomlinson and D. E. Cox, "Synchrotron X-ray powder diffraction". *Journal of Applied Crystallography* 17, 85 (1984).
13. R. J. Cernik, P. K. Murray, P. Pattison and A. N. Fitch, "A two - circle powder diffractometer for synchrotron radiation with a closed loop encoder feedback system". *Journal of Applied Crystallography* 23, 292 (1990).
14. P. Coppens, D. Cox, E. Vlieg and I. K. Robinson, *Synchrotron radiation*

crystallography. (Academic Press, 1992).

15. ID22 - HIGH RESOLUTION POWDER DIFFRACTION BEAMLINE, http://www.esrf.eu/id22
16. P. L. Lee, D. Shu, M. Ramanathan, C. Preissner, J. Wang, M. A. Beno, R. B. Von Dreele, L. Ribaud, C. Kurtz, S. M. Antao, X. Jiao and B. H. Toby, "A twelve - analyzer detector system for high - resolution powder diffraction". *Journal of Synchrotron Radiation* 15, 427 (2008).
17. J. E. Parker, S. P. Thompson, J. Potter, T. P. Hill, A. Birt, T. M. Cobb, F. Yuan, and C. C. Tang, "Beamline I11 at Diamond: A new instrument for high resolution powder diffraction". *Review of Scientific Instruments* 80, 075107 (2009).
18. R. A. Young, *The Rietveld Method*. (Oxford University Press, Oxford, 1993).
19. G. W. H. Höhne, W. F. HemmingerH. J. Flammersheim, *Differential Scanning Calorimetry*. (Springer-Verlag Berlin Heidelberg, Berlin, 2003).
20. Differential scanning calorimetry, http://pslc.ws/macrog/dsc.htm
21. Differential scanning calorimetry, https://en.wikipedia.org/wiki/Differential_scanning_calorimetry.
22. F. Meneau, G. N. Greaves, A. Sapelkin,L. M. Colyer, I. ap Gwynn, S. Wade and G. Sankar, "The rheology of collapsing zeolites amorphized by temperature and pressure". *Nature materials* 2, 622 (2003).
23. S. Maher, F. P. M. Jjunju and S. Taylor, "Colloquium: 100 years of mass spectrometry: Perspectives and future trends". *Rev. Mod. Phys.* 87, 113 (2015).
24. O. D. Sparkman, *Mass Spectrometry Desk Reference*. (Global View Pub,

Califonia, 2000).

25. Inductively Coupled Plasma–Mass Spectrometry, https://icp-ms.wikispaces.com/
26. D. J. Gardiner, *Practical Raman spectroscopy*. (Springer-Verlag, Michigan, 1989).
27. E. Smith and G. Dent, *Modern Raman Spectroscopy: A Practical Approach*. (Wiley, New York, 2013).
28. Spectroscopie Raman, http://wwz.ifremer.fr/rd_technologiques/Moyens/Laboratoires/Spectroscopies-Techniques-de-mesures-in-situ/Spectroscopie-Raman
29. Raman spectroscopy, https://en.wikipedia.org/wiki/Raman_spectroscopy
30. L. Santona P. Castaldi, C. Cozza, V.Giuliano, C. Abbruzzese, V. Nastro and P. Melis, "Thermal and spectroscopic studies of zeolites exchanged with metal cations". *Journal of Molecular Structure* 734, 99 (2005).
31. A. A. Coelho, *Topas-Academic*. (A Computer Programme for Rietveld Analysis, 2004.).
32. G. Will, *Powder diffraction: The Rietveld method and the two stage method to determine and refine crystal structures from powder diffraction data*. (Springer Science & Business Media, 2006).
33. R. B. Von Dreele, L. B. McCusker, D. E. Cox, D. Louër and P. Scardi, "Rietveld refinement guidelines". *J. Appl. Cryst.* 32, 36 (1999).
34. R. E. Dinnebier, S. J. L. Billinge, *Powder Diffraction: Theory and Practice*. (Royal Society of Chemistry, 2008).

3. Sodium Zeolite Y

3.1. Introduction

The investigation on *ex-situ* temperature induced amorphization of sodium zeolite Y (Na zeolite Y) is described in this chapter. Dehydrated Na zeolite Y samples have been treated at various temperatures, making different samples with different degrees of amorphization. These various samples have been studied by Inductively Coupled Plasma Mass Spectrometry (ICP-MS), laboratory X-ray Powder Diffraction (XRPD), High Resolution X-ray Powder Diffraction (HR-XRPD), Differential Scanning Calorimetry (DSC), Raman spectroscopy, and inelastic neutron scattering. The samples used in this study were obtained from Shanghai Jiujie Chemical Corporation. The composition of Na zeolite Y may vary marginally according to its chemical production method, but the framework structure stays the same [*1*], which is also confirmed by XRPD in this work (Section 3.2.5). In order to determine the accurate composition of the Na zeolite sample, it was analyzed by ICP-MS. The structural changes due to amorphization have been studied by XRPD and HR-XRPD. Thermal properties of the Na zeolite Y samples are determined by DSC. Raman spectroscopy and inelastic neutron scattering are used to study the dynamic properties of the samples. Techniques are combined to study the different steps of the Na zeolite Y amorphization. All the techniques mentioned in this chapter were introduced in Chapter 2.

3.2. Experimental work

3.2.1. ICP-MS

Before any other measurement was taken, ICP-MS was used to determine the composition of the Na zeolite Y sample [*2*]. The Na zeolite Y sample (0.1g) was dissolved in HNO_3 solution and analysed with an Agilent Technology 7700 Series ICP-MS. The composition of metal ions is listed in Table 3.1. All the compositions are in weight percent. The content of oxygen was calculated by the valence.

Ion	Na	Al	Si
Weight percent (%)	7.82	9.10	21.74

Table 3.1 The weight percent of the metal ions in Na zeolite Y samples, errors within 0.01%

The chemical formula for the Na zeolite Y can be calculated from ICP-MS as $Na_{58}Al_{58}Si_{134}O_{384}$. The water content is not shown in this formula as it cannot be obtained from ICP-MS. This formula is used in preference to the minimized form as this represents the Na zeolite Y unit cell.

3.2.2. Water content

As the zeolite will always absorb water from the atmosphere until it reaches a limit, the water content in its chemical formula cannot be ignored. In this study, the water content of the sample was determined by weighing sample before and after

dehydration. The dehydration was carried out by heating the sample in a vacuum furnace to a temperature of 573K with the temperature raising rate at 20K/min, and kept for 1 hour. The weight difference and weight percent of water are shown in Table 3.2.

Sample weight before dehydration (g)	Sample weight after dehydration (g)	Weight difference (g)	Weight difference (%)
13.52	10.41	3.11	23.00

Table 3.2 The weight difference of the sample before and after dehydration and the weight percentage calculated from this.

By calculating weight percentage using the data in Table 3.2, the chemical formula for hydrated Na zeolite Y is shown to be $Na_{58}Al_{58}Si_{134}O_{384}\cdot 212H_2O$. Multiple samples were studied and the weight percent of the water were consistent to within 1%.

3.2.3. DSC

DSC was conducted on a NETZSCH DSC 404C in the Material Laboratory at Shanghai University, with the temperature raising rate 10K/min [*3*]. The sample used here is hydrated Na zeolite Y, because the sample would be dried during heating before it reaches amorphization temperature. Fig. 3.1 shows the DSC result of the hydrated sample.

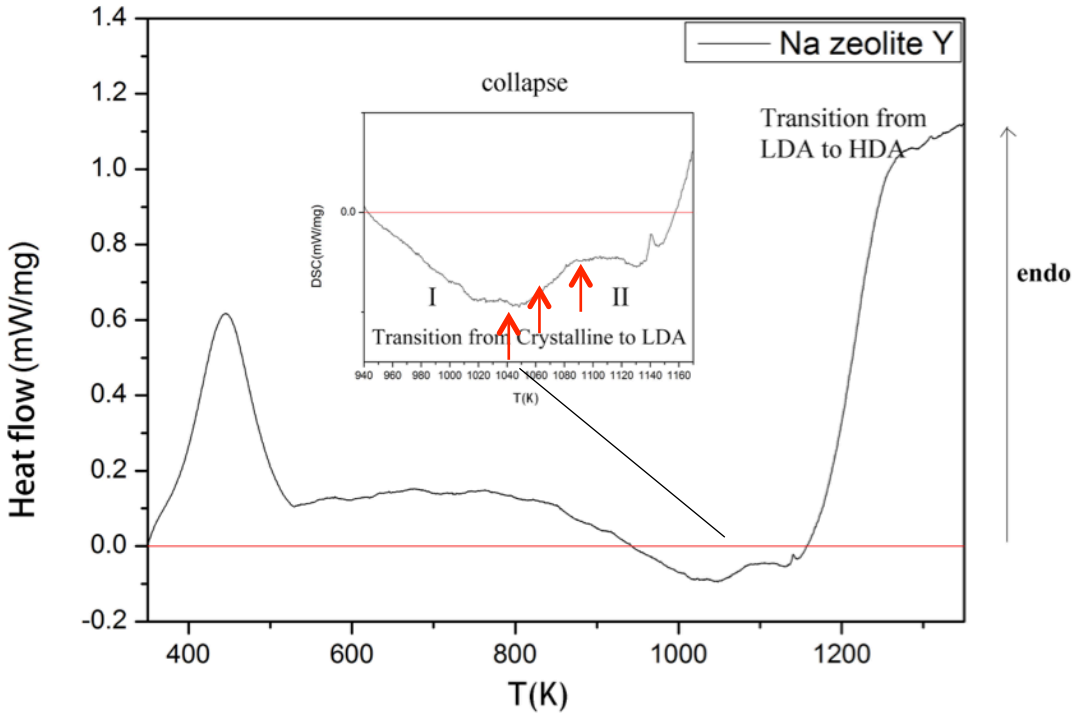

Fig. 3.1 DSC result of hydrated Na zeolite Y that shows the water loss, the collapse (inset) and the LDA to HDA process. Arrows show the target temperatures used in the XRPD experiment.

From Fig. 3.1, the water loss can be seen before the temperature arrives at 485K, where the sample gives out large quantity of heat making a very high exothermic peak. When the temperature arrives 946K, the sample starts to obtain energy which is the collapse period which is enlarged in the inset graph. Over this range, the change from I to II indicates the zeolite Y transfer from crystalline phase to low density amorphous phase.

This figure shows that the collapse start from 946K and end at 1150K, following by a transition from low density amorphous phase (LDA) to high density amorphous phase (HDA). The collapse shows a relatively broad peak, indicating that the collapse happens over a temperature range rather than a unique temperature, which agrees with the XRPD result shown below.

3.2.4. Amorphous sample preparation

All the Na zeolite Y samples were put into alumina boats for heat treatment. They were all heated to 573K by 20K/min and kept for 1 hour to get rid of water. Because this is the starting material of the following heat treatment, it is called dehydrated Na zeolite Y sample. Different heat treatments were conducted on the starting material, details for this are listed in Table 3.3 and shown graphically in Fig. 3.2 for clarity. The rate of temperature raise was kept at 10K/min. The temperature and the length of time that samples were kept were also listed. The range of temperature studied was taken from the DSC result from section 3.2.3.

Time / Temperature	0min	20min	40min	60min
1023K	Na1023-0	Na1023-20	Na1023-40	Na1023-60
1048K	Na1048-0	Na1048-20	Na1048-40	Na1048-60
1073K	Na1073-0	Na1073-20	Na1073-40	Na1073-60

Table 3.3 List of samples and heating regime

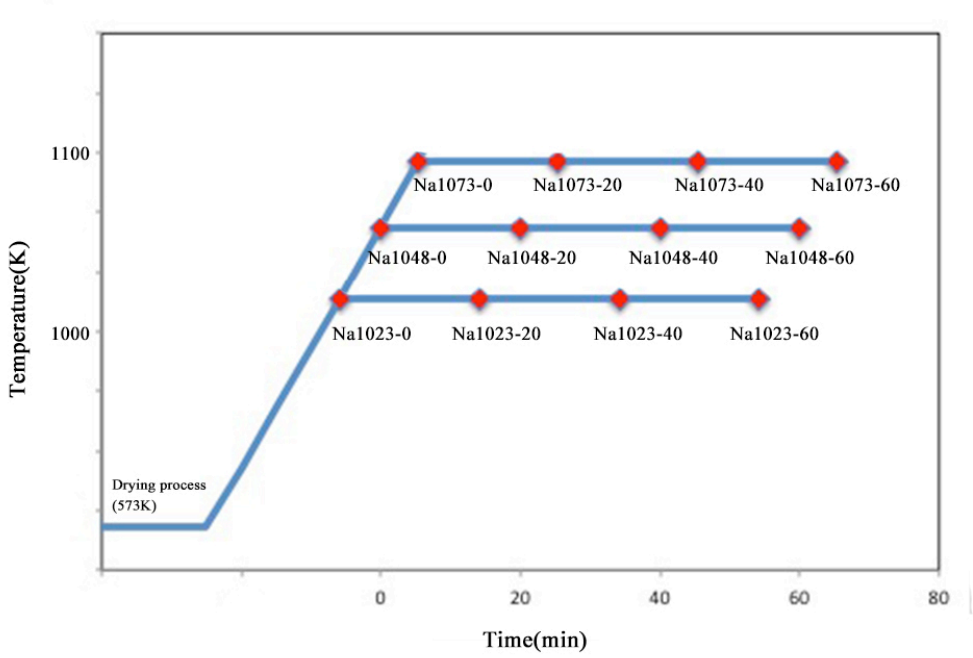

Fig. 3.2 Na zeolite Y samples under different heat treatment

3.2.5. XRPD

XRPD was conducted on all the samples listed in Table 3.3 and the dehydrated Na zeolite Y sample. XRPD measurements were taken in the ISIS Material Characterization Lab using a Rigaku Miniflex 600, with Cu $K\alpha_1$ (40kV, 15mA, λ=1.5406 Å). The XRPD pattern for dehydrated Na zeolite Y is shown in Fig. 3.3.

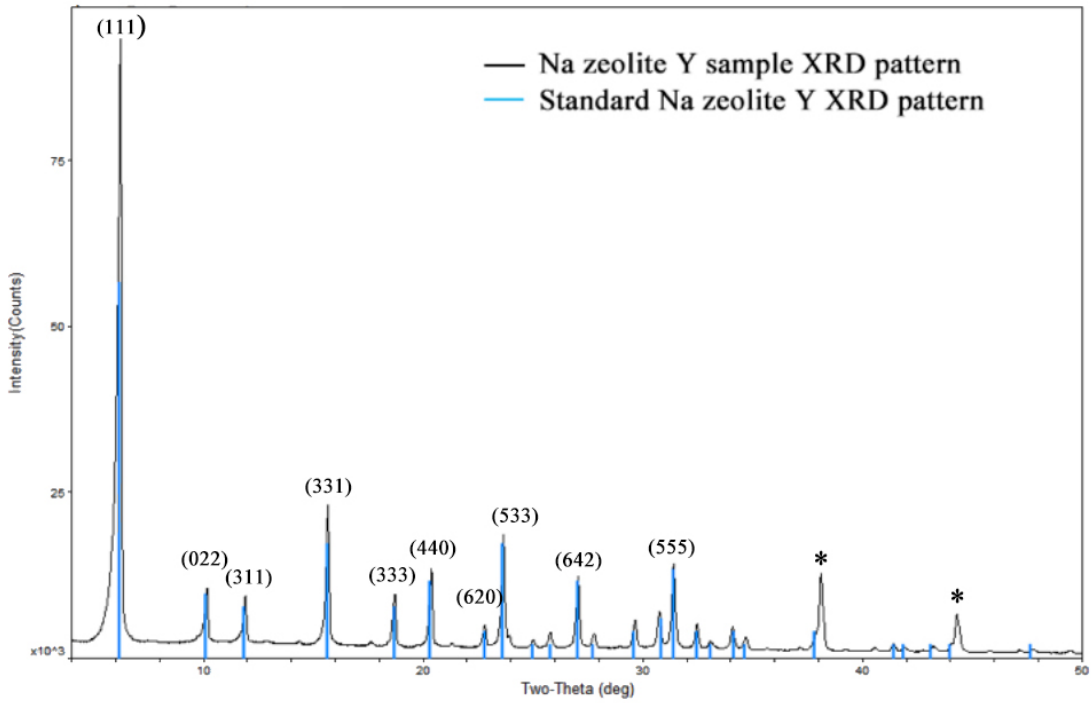

Fig. 3.3 The XRPD pattern of dehydrated Na zeolite Y, while the blue lines represent a reference Na zeolite Y pattern (JCPDS: 38-0239). The lattice planes defined by Miller index have been marked out. The two * peaks come from Al samples container.

The pattern shows agreement with the reference pattern, indicating that this sample holds a zeolite Y Faujasite structure.

The XRPD pattern of the Na zeolite Y samples heated under 1023K, 1048K and 1073K are shown in Fig. 3.4, 3.5 and 3.6 each measured at ambient temperature. The degrees of amorphization are calculated by Rietveld method based on the intensity subtraction method. (Chapter 2, Section 2.3.2)

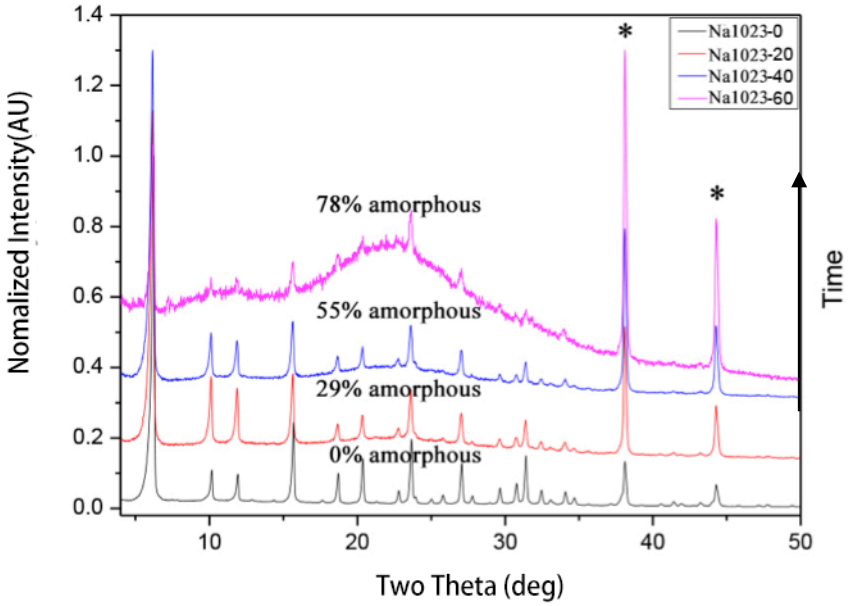

Fig. 3.4 The XRPD patterns for Na zeolite Y samples kept at 1023K for 0 min, 20min, 40min and 60min. Different degrees of amorphization are indicated. The * peaks come from the Al sample container.

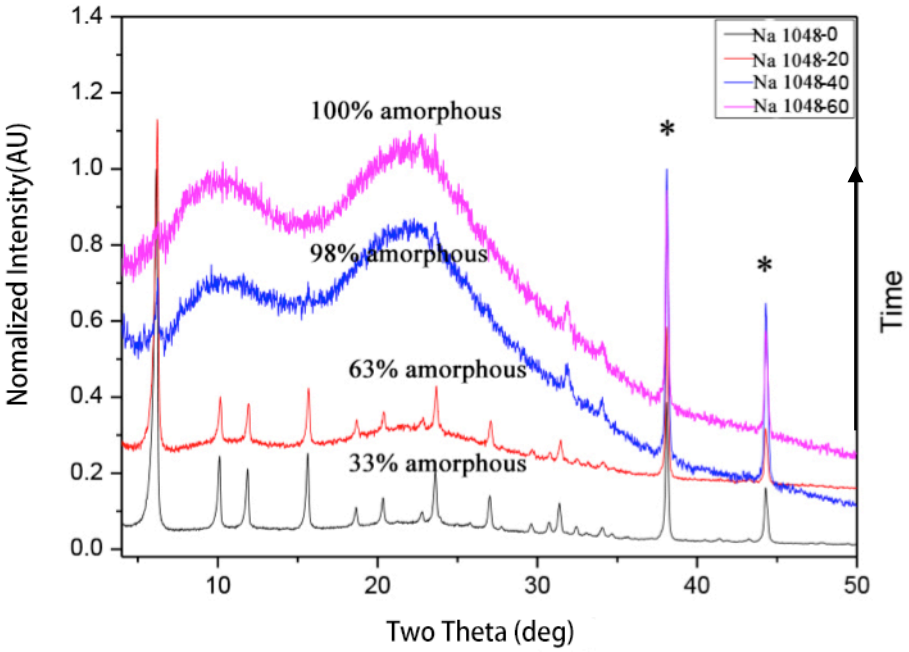

Fig. 3.5 The XRPD patterns for Na zeolite Y samples kept at 1048K for 0 min, 20min, 40min and 60min. Different degrees of amorphization are indicated. The * peaks come from the Al sample container.

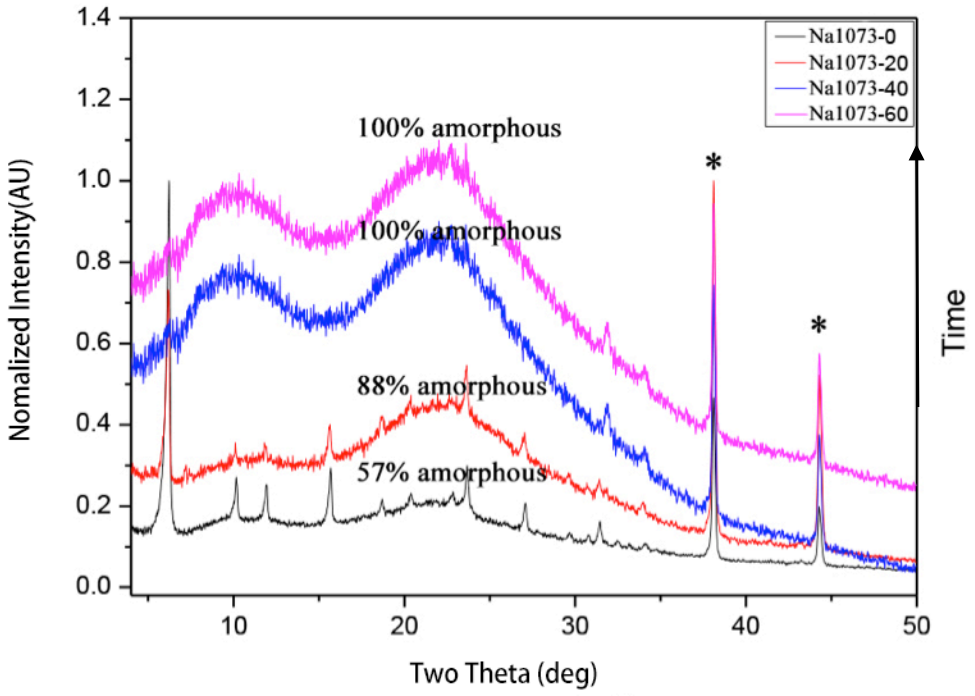

Fig. 3.6 The XRPD patterns for Na zeolite Y samples at 1073K kept for 0 min, 20min, 40min and 60min. Different degree of amorphization were indicated. The * peaks come from the Al sample container.

When samples were kept at 1023K, significant changes can be seen on the XRPD pattern which developed with time. As time passes, the intensity of the sharp diffraction peaks decrease and broad structures emerge indicating that the materials is becoming less crystalline and more amorphous.

When comparing the three figures it can be seen that the time used for the samples to totally collapse becomes shorter at higher temperature. The main difference between the collapse speeds was shown before the samples were kept at a set temperature. To make it clear the speeds of collapse at different target temperature are drawn in Fig. 3.7.

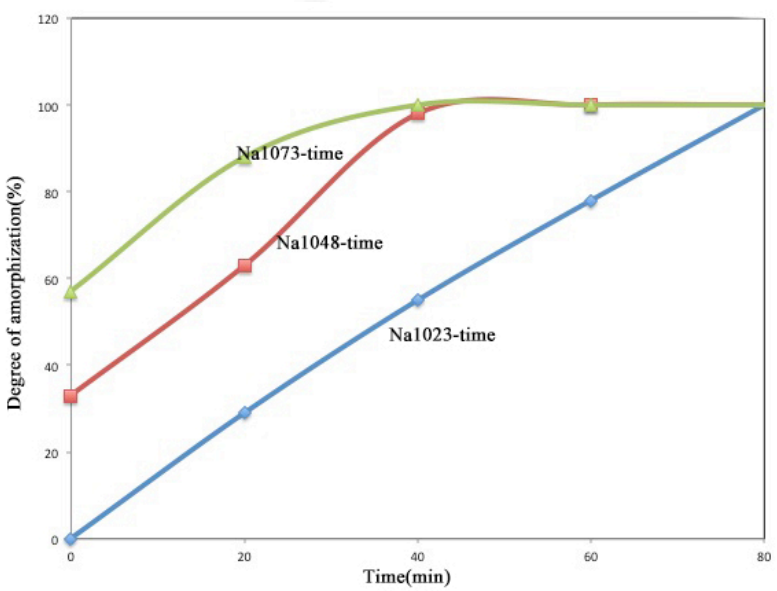

Fig. 3.7 The speed of amorphization at different temperatures

Even though the difference is slight, the trend of the influence of temperature can be seen. When the temperature is higher, the speed of collapse increases.

3.2.6. HR-XRPD

High Resolution Powder X-ray Diffraction (HR-XRPD) was performed on I11 at Diamond Light Source (DLS), using 15 keV , λ=0.825875(10) Å. [*4*]. The wavelength was calibrated using high quality Si powder standard (SRM640c) from National

Institute of Standards (NIST in USA). The initial pattern for dehydrated Na zeolite Y and Na1023-40 sample are shown in Fig. 3.4. A partial collapse sample Na1023-40 was chosen, to see the changes of atom positions under the heat treatment. All samples were dried and sealed in capillaries as described in Chapter 2, section 2.2.1.3 . Fig. 3.8 shows that the XRPD pattern of the sample before and after collapse. The change in the (111) peak shape and position is highlighted in Fig. 3.9.

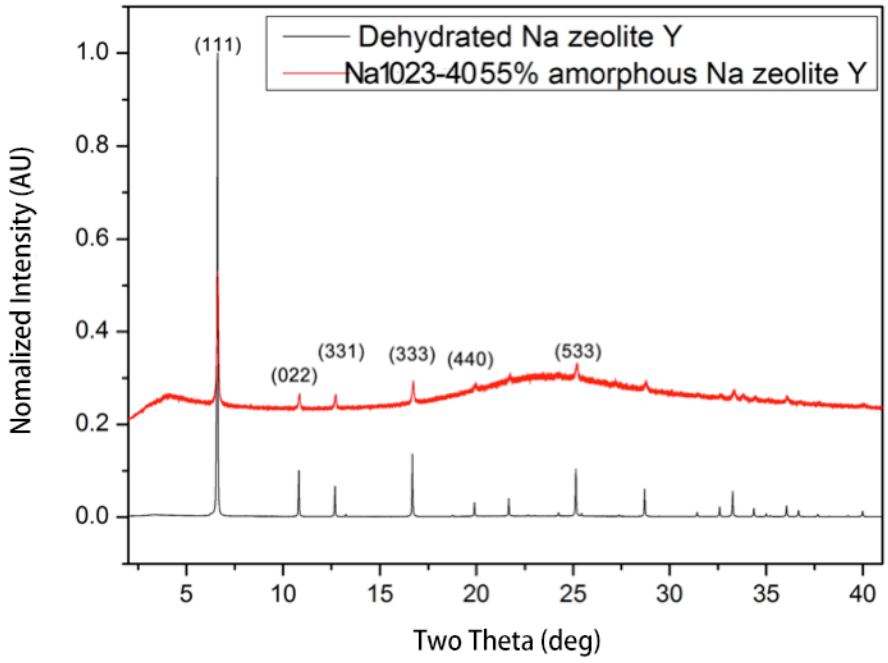

Fig. 3.8 HR-XRPD pattern of Na zeolite Y and sample Na1023-40 showing the replacement of diffraction peaks with different degree of amorphization

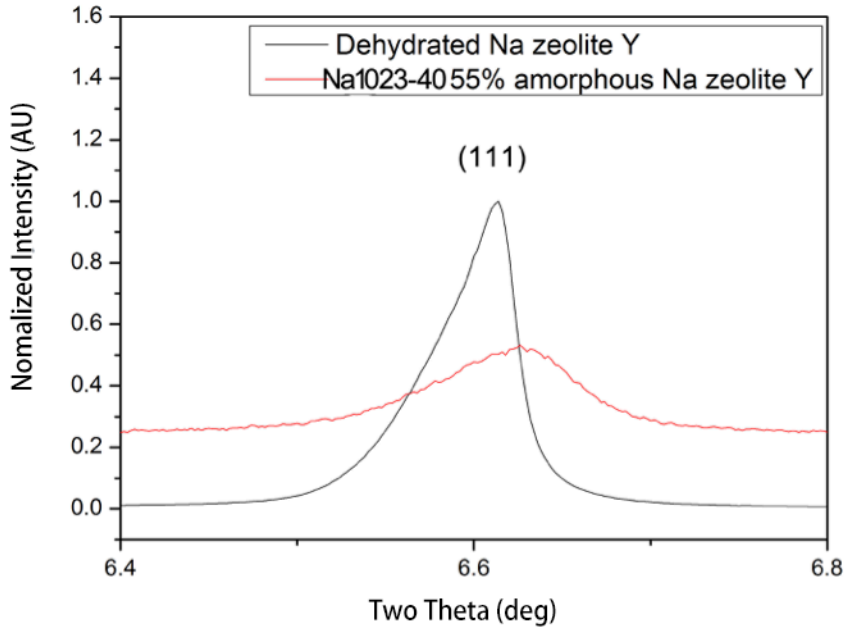

Fig. 3.9 The (111) peak's diffraction peak position changes in two Na zeolite Y samples, showing the shrinkage of the unit cell. The peak shown as red curve shifted to higher angle. The reduction of intensity was due to more amorphous content.

Taking (111) peak for instance, the peak position change indicated that the cage structure becomes smaller as a result of partial amorphization. The asymmetrical peak shape is due to the axial divergence of the HR-XRPD instrument [*4*].

HR-XRPD data (Fig. 3.8) were analysed using TOPAS software, which enables trial coordinates to be tested and then refined using the Rietveld technique based on the same space group (Chapter 1, Section 1.1). Starting with the published Na zeolite Y structure $Na_{59}Al_{59}Si_{133}O_{384}$ [5], this was refined for the dried commercial material $Na_{58}Al_{58}Si_{134}O_{384}$, indicating small differences in unit cell size and cation positions

(Table 3.4). In particular the higher loading of Si and lower loading of Al was responsible for the slight decrease in unit cell size, compared to the reference structure. Likewise there were small changes in the positions and occupancy of the charge-compensating cations, located in the double 6-fold rings (D6R), the sodalite cages and supercage. In the material used here, there were more Na in the sodalite cage and fewer Na in D6R and the super cage. Turning to the comparison between the partial collapsed sample Na1023-40 and the dehydrated commercial Na zeolite Y sample, differences between the unit cell sizes and the cation positions can again be seen. During the collapse the unit cell size decreases a lot, indicating that the cages shrink when high temperature is applied. This may well be due to the fact that in Na1023-40 55% of the sample is already amorphous. Having a higher density than crystalline Na zeolite Y could result in a local change in pressure for the remaining 45% crystal, as suggested in *in situ* XRPD [6 - *8*].The present results are a more accurate consequence of this effect conducted at ambient temperature where the unit cell clearly shrinks. The change of cation positions has shown that the cations move to smaller D6R and sodalite cages suggesting these are more stable in the structure. The dehydrated structure model is shown in Fig. 3.10.

Sample	Unit cell parameter (Å)	Na in D6R (%)	Na in sodalite cage (%)	Na in supercage (%)
Reference Na zeolite Y	24.791	11.5	35.1	53.4
Dehydrated Na zeolite Y	24.715 ± 0.0001	3.0 ± 0.03	46.3 ± 0.4	50.7 ±0.5
Na1023-40	24.689 ± 0.0002	5.6 ± 0.05	56.1 ± 0.5	37.9 ± 0.4

Table 3.4 Cubic size and ion distribution of reference zeolite Y and zeolite Y sample

(a)

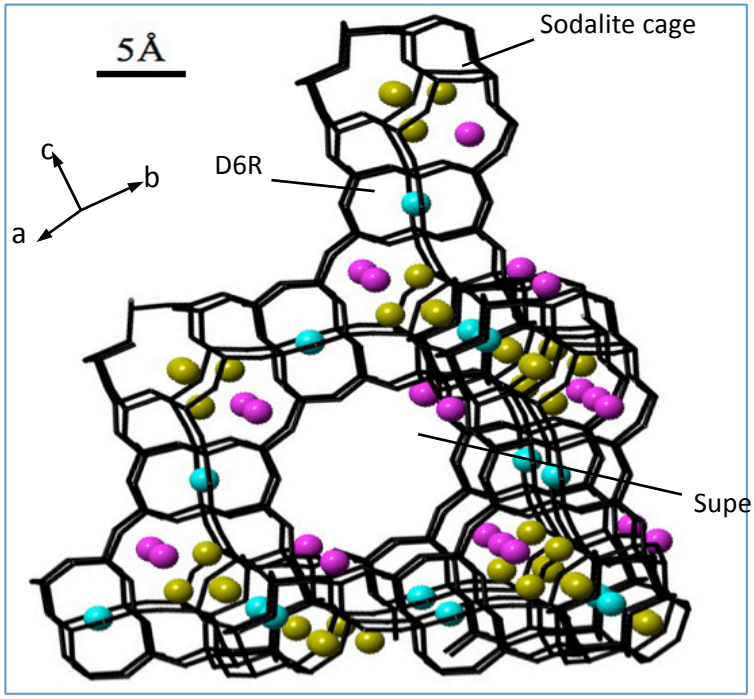

(b)

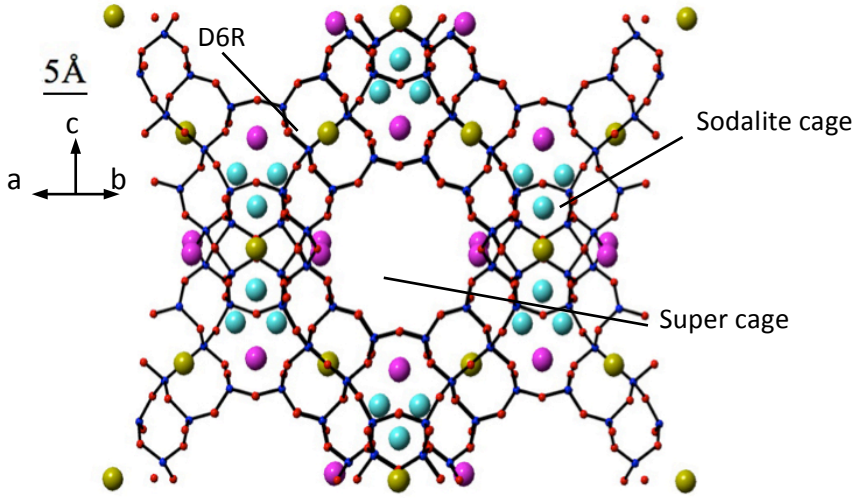

Fig. 3.10 (a)The structure of zeolite Y in 3D image (b) The structure of zeolite Y in 2D image, where magenta balls represent Na atoms in super cages, blue balls are Na

in sodalite cages and magenta balls are Na in D6R. The framework is built by Si, Al and O

After Rietveld refinement the parameters and coordinates are listed in Table 3.5 and 3.6. And the Rietveld refinement pattern were presented in Fig. 3.11

Rietveld parameters	Na zeolite Y	Na1023-40 sample
Scale factor	3.347e-7	3.339e-7
Zero point 2θ	-0.0857	-0.0082
Background		
B0	338.276	407.356
B1	-96.658	-105.150
B2	-48.940	-65.005
B3	-29.931	-18.235
Overall isotropic		
R_{wp}	9.252	6.743
R_{exp}	2.907	2.767
R_p	6.904	4.258

Table 3.5 Final parameters of Rietveld refinement (errors are within 1% of the original parameter)

Atom type	x	y	z	Occupation
		Na zeolite Y		
Si， Al	0.123	0.945	0.037	1
O1	0.174	0.174	0.979	1
O2	0.179	0.179	0.319	1
O3	0.252	0.252	0.143	1
O4	0.107	-0.107	0	1
Na1	0.086	0.0897	0.0897	0.7

Na2	0	0	0	0.05
Na3	0.238	0.238	0.238	0.90
		Na1023-40		
Si， Al	0.125	0.944	0.037	1
O1	0.172	0.172	0.983	1
O2	0.179	0.179	0.325	1
O3	0.252	0.252	0.139	1
O4	0.107	-0.107	0	1
Na1	0.246	0.242	0.246	0.90
Na2	0	0	0	0.12
Na3	0.445	0.561	0.445	0.68

Table 3.6 Final structure model of two samples (errors are within 1% of the original parameter)

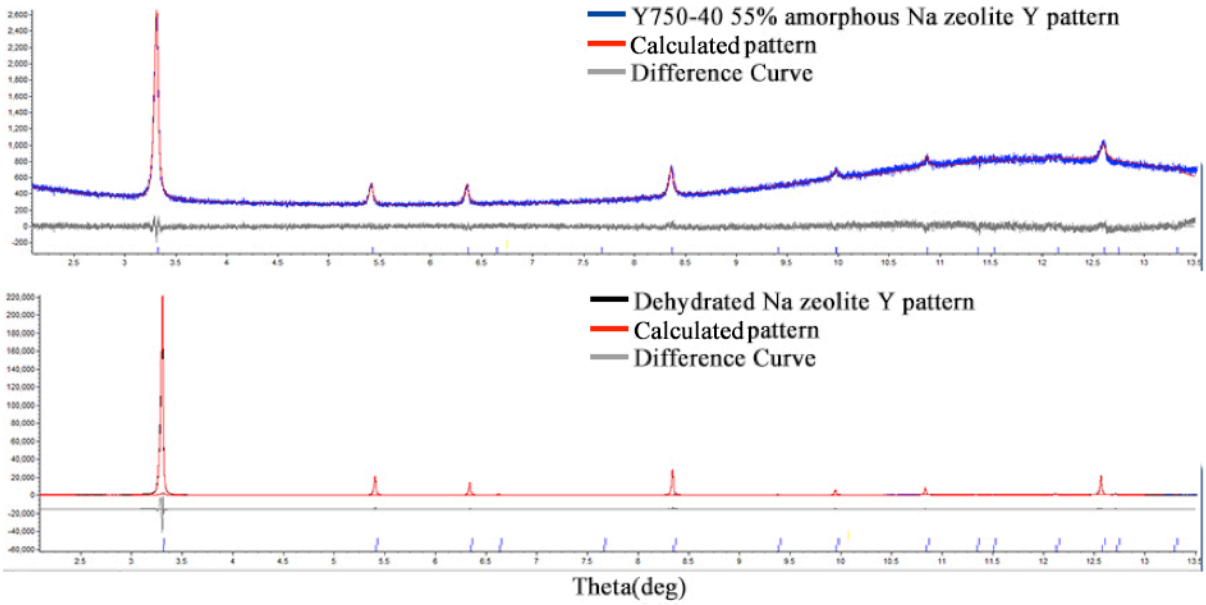

Fig 3.11 The comparison of the calculated pattern with the observed pattern

The R factor and the difference curve show that the structure obtained from this is reasonable.

3.2.7. Raman Spectroscopy

Raman spectroscopy was conducted at room temperature on samples heated previously up to 1023K in order to show a range of degrees of amorphization as presented Fig. 3.12. Focusing on the uncollapsed zeolite sample, the spectrum shows the stretching and bending modes of the T(Al, Si)-O. Mixed stretching and bending modes of T-O-T are shown in Raman bands from 300cm^{-1} to 550 cm^{-1}. [*9, 10*] These bands come from the inter-tetrahedral angle, bond length and mass of T atoms. For the different tetrahedral ring sizes which occur in the Faujasite structure, well-separated Raman bands can be detected: the lower the number of participating tetrahedra per ring size, the lower the intra-tetrahedral angle and, hence, the higher the vibration's resonance energy and band frequency. The bands at 295 cm^{-1} and 384 cm^{-1} are characteristic for the T-O-T bending associated with 6-membered rings, while the 515 cm^{-1} band comes from the 4-fold rings. There are basic rings that make zeolite Y (Fig. 1.4). The higher frequency range of >700 cm^{-1} is dominated by bands associated with T(Si,Al)-O symmetric and asymmetric stretching vibrations which are weak for uncollasped Na zeolite Y compared to the Raman results with different degrees of amorphization. Peaks become significantly broader and the intensity of 515 cm^{-1} peak decreases slightly, which indicates the four fold ring is relatively stable. Signatures of 6-fold rings also remain but become weaker. For fully collapsed Na zeolite Y all the peaks below 550 cm^{-1} overlap forming a broad amorphous peak, signifying other bending is occurring, notably 5-fold rings. In the higher frequency range, the small peaks from the stretching vibration increases a lot as the collapse destroys the cage

structure. When the structure is totally destroyed in the 100% amorphous sample, the Raman result converges with the quenched aluminosilicate spectrum, where very similar Raman profiles are present for similar composition. For example $(Na_2O)_{0.25}$ $(Al2O3)_{0.25}$ $(SiO_2)_{0.75}$ [*11*] to our $Na_{58}Al_{58}Si_{134}O_{384}$.

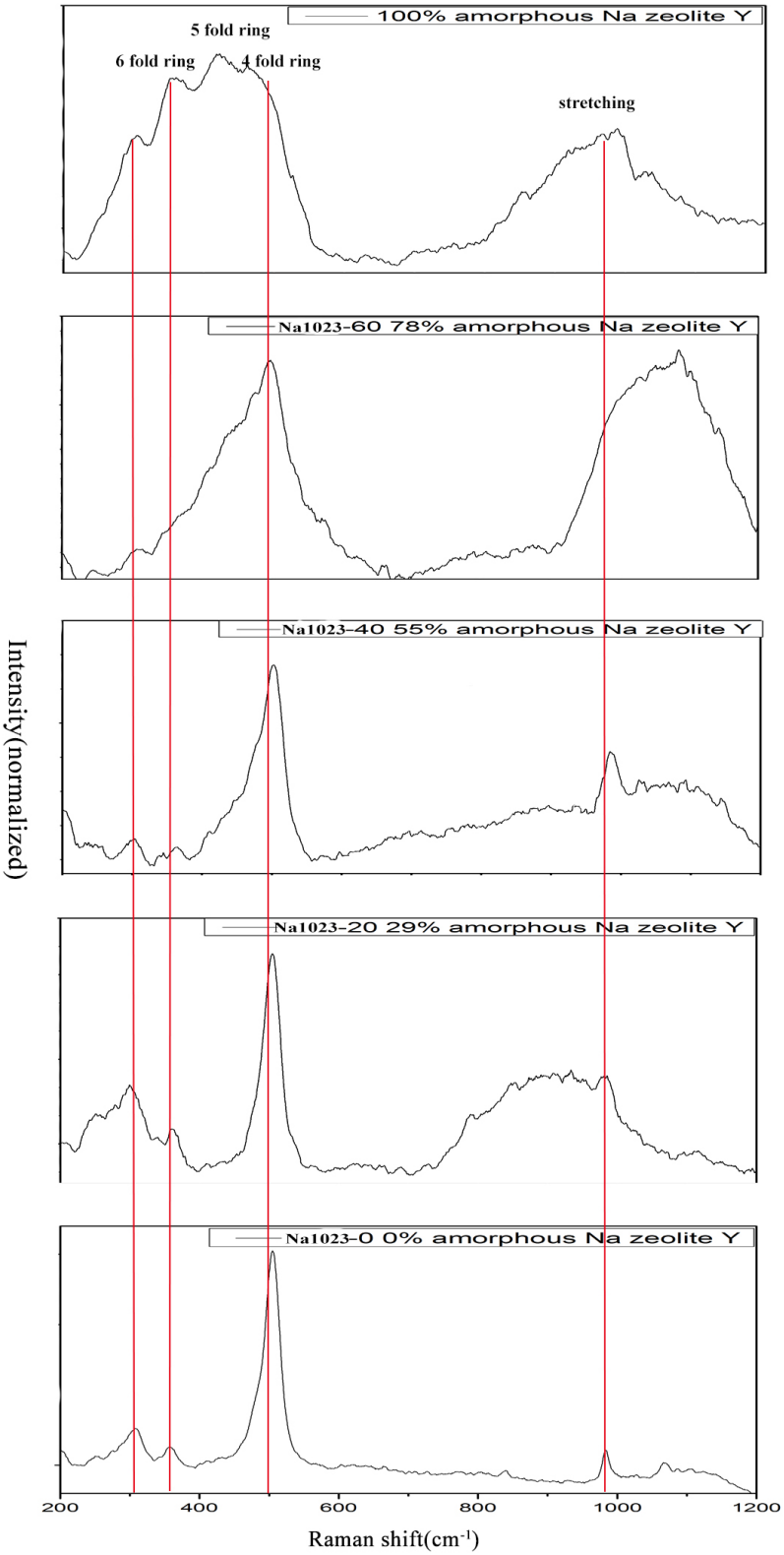

Fig 3.12 The Raman spectra of different amorphous sample marked with obvious changes with the collapse.

3.2.8. Neutron scattering

Inelastic neutron scattering results were produced on ISIS MARI instrument. It was conducted on dehydrated samples and the collapsed samples using 17meV neutrons and 0.8 meV resolution. (Fig. 3.13)

a **b**

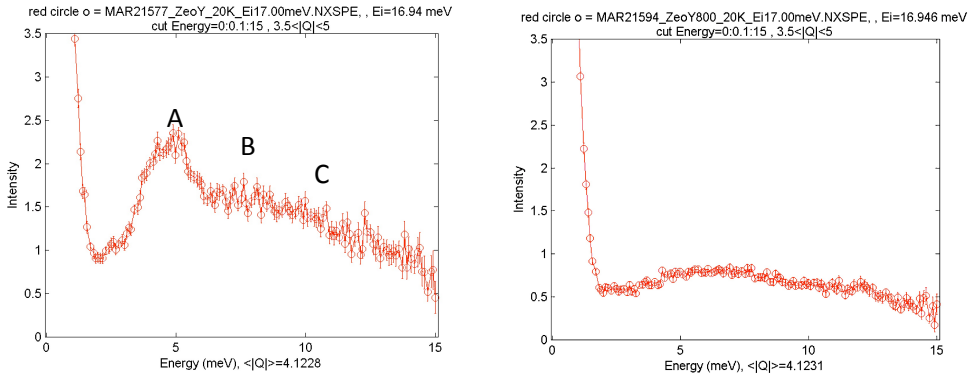

Fig. 3.13 (a) INS result of zeolite Y at 20 K to reduce the thermal vibration. (b)INS result of collapsed Zeolite Y at 20 K to reduce the thermal vibration.

From the uncollapsed sample we can determine the features of the structure. The 5meV band (A) indicates the vibration of the super cage made up of 4- and 6- fold rings (Fig.1.4) . The broad peaks around 8 meV (B)indicates the vibration of sodalite cage and the broad peaks around 12meV (C) indicates the vibration of the D6R following identification in reference [*12*]. These peaks disappear in the collapsed sample showing that the vibrations of the supercages, sodalite cages and D6R vanish which indicates the structure becomes that of a quenched glass. There is a broad peak of this amorphous sample which is associated with the Boson peak [*13*].

3.3. Analysis

Combining the DSC result (Fig. 3.1) and the XRPD results (Fig. 3.4-3.6), the process of collapse can be shown to happen over a broad temperature range and within this temperature range the speed of collapse is observed to be faster when the temperature is higher (Fig. 3.7). According to G. N. Greaves [*14*], this temperature range will change according to the rate of heating, the temperature range being higher when the of heating is lower.

Combining the Raman and the inelastic neutron scattering (Fig. 3.12 and 3.13), the disappearance of the zeolite cages can be seen. The inelastic neutron scattering shows the changes to the cages and the Raman shows the change to the rings. The cages topology disappear with amorphization according to the inelastic neutron scattering, however the uncollapsed structure still contains 4- and 6- fold rings according to Raman results. The 4-fold rings in the cages appear to be relatively stable. The Raman spectroscopic results suggest some new rings grow with the heat treatment.

3.4. References

1. D. W. Breck, *Zeolite molecular sieves*. (Krieger, 1984.).
2. O. D. Sparkman, *Mass Spectrometry Desk Reference*. (Global View Pub, Califonia, 2000).
3. G. W. H. Höhne, W. F. Hemminger and H. J. Flammersheim, *Differential Scanning Calorimetry*. (Springer-Verlag Berlin Heidelberg, Berlin, 2003).

4. S. P. Thompson, J. E. Parker, J. Potter, T. P. Hill, A. Birt, T. M. Cobb, F. Yuan and C. C. Tang, "Beamline I11 at Diamond: A new instrument for high resolution powder diffraction". *Review of Scientific Instruments* 80, 075107 (2009).

5. J. R. Sieber, S.Turner, T. W. Vetter, R. Zeisler, A. F. Marlow, M. G. Moreno-Ramireza, M. E. Davis, G. J. Kennedy, W. G. Borghard, S. Yang, A. Navrotsky, B. H. Toby, J. F. Kelly, R. A. Fletcher, E. S. Windsor, J. R. Verkouteren and S. D. Leigh, "Characterization of chemical properties, unit cell parameters and particle size distribution of three zeolite reference materials: RM 8850 – zeolite Y, RM 8851 – zeolite A and RM 8852 – ammonium ZSM-5 zeolite". *Microporous and Mesoporous Materials* 107, 252 (2008).

6. R. A. Young, *The Rietveld Method*. (Oxford University Press, Oxford, 1993).

7. R. B. Von Dreele, L. B. McCusker, D. E. Cox, D. Louër and P. Scardi, "Rietveld refinement guidelines". *J. Appl. Cryst.* 32, 36 (1999).

8. A. A. Coelho, *Topas-Academic*. (A Computer Programme for Rietveld Analysis, 2004.).

9. S. Fuhrmann, T. Palenta, G. N. Greaves, W. Schwieger and L. Wondraczek "Thermal collapse and hierarchy of polymorphs in a faujasite-type zeolite and its analogous melt-quenched glass". *J. Chem. Phys.* 142, 084503 (2015).

10. W. Mozgawa, M. Krol, K. Barczyk, T. Bajda and M. Kozanecki, "Changes in the vibrational spectra of zeolites due to sorption of heavy metal cations". *J. App. Spec.* 80, 662 (2013).

11. B. O. Mysen, D. Virgo and F. A. Seifert, "Three-dimensional network structure of quenched melts (glass) in the systems SiO2-NaAlO2, SiO2-CaAl2O4 and SiO2-MgAl2O4.". *American Mineralogist* 67, 696 (1982).

12. F. Meneau, G. N. Greaves, O. Majérus, D. G. Jones and J. Taylor, "Identifying Vibrations That Destabilize Crystals and Characterize the Glassy State". *Science* 308, 1299 (2005).

13. C. Oligschleger and M. Dolg and A. B. Mukhopadhyay, "Low-frequency vibrational excitations in zeolite ZSM-5 and its partially crystalline derivatives". *Physical Review* 69, 12202 (2004).

14. G. N. Greaves, F. Meneau, A. Sapelkin, L. M. Colyer, I. A. Gwynn, S. Wade and G. Sankar, "The rheology of collapsing zeolites amorphized by temperature and pressure". *Nature Materials* 2, 622 (Sep, 2003).

4. Ion exchanged Zeolites

4.1. Introduction

The investigation of temperature induced structural changes in ion exchanged zeolite Y and a comparison to Na zeolite Y (from Chapter 3) is introduced in this chapter. The exchange ions here are Cu^{2+} and Nd^{3+}, using the method of ion exchange detailed in Chapter 2 [*1*]. Various samples have been made by treatment under different temperature and time conditions, achieving several samples with different degrees of amorphization. The compositions of the ion exchanged zeolite Y samples were obtained by ICP-MS in the Department of Geography at Aberystwyth University. Differential scanning calorimetry (DSC) is used here to detect the thermal properties of the ion exchanged zeolite Y. This was completed in Department of Material Science at Shanghai University. The structure of the ion exchanged zeolite Y and changes under heat treatment were studied by laboratory X-ray diffraction (XRPD) at ISIS material lab and high resolution X-ray diffraction at Diamond light source. Raman spectroscopy conducted in the Physics Department was used to study the dynamic properties of the samples. These complementary techniques were chosen to study the structure of ion exchanged zeolite Y as well as their changes during amorphization.

4.2. Experimental work

4.2.1. ICP-MS

The ion exchange was conducted on the raw Na zeolite Y using the method introduced in Chapter 2. With this method the weight percentage of the exchanged ion can be estimated, however the detailed composition still need to be determined by ICP-MS. Experiments were conducted on Agilent Technology 7700 series ICP-MS. The compositional results of all the metal ions are listed in Table 4.1. All the compositions are in weight percentage. The content of oxygen was calculated by the valence from the mole percent of the cations.

Ion(wt%) / Sample	Na	Al	Si	Cu	Nd
Cu zeolite Y	5.2	11.8	28.3	6.7	0
Nd zeolite Y	4.7	11.4	27.1	0	10.4

Table 4.1 The weight percent of the metal ions in Cu zeolite Y and Nd zeolite Y samples obtained by ICP-MS(errors are within 0.01%)

The chemical formula for the Cu zeolite Y and Nd zeolite Y samples can be calculated as $Cu_{14}Na_{30}Al_{58}Si_{134}O_{384}$ and $Nd_{10}Na_{28}Al_{58}Si_{134}O_{384}$.

4.2.2. Water content

The water content of the two ion exchanged samples were determined by measuring the weight difference of the samples before and after dehydration as described in section 3.2.2. The weight difference and the calculated weight percentage of the water are listed in Table 4.2

Sample	Sample weight before dehydration (g)	Sample weight after dehydration (g)	Weight difference (g)	Weight difference (%)
Cu zeolite Y	14.50	11.19	3.31	22.8
Nd zeolite Y	13.42	10.19	3.23	21.4

Table 4.2 The weight difference of the samples before and after dehydration and the weight percentage(errors are within 0.01g).

Using the data from Table 4.2, the complete chemical formulas for hydrated Cu zeolite Y and Nd zeolite Y samples were calculated as $Cu_{14}Na_{30}Al_{58}Si_{134}O_{384}\cdot 213H_2O$ and $Nd_{10}Na_{28}Al_{58}Si_{134}O_{384}\cdot 205H_2O$. A number of samples were measured, and the weight percent of the water was consistent to within 1%.

4.2.3. DSC

The DSC conducted using the same instrument as for Na zeolite Y (Section 3.2.3) with a temperature raising rate 10K/min which is the same as the heat treatment used after dehydration. The samples used here are hydrated materials, as they are dried during the measurement. Fig. 4.1 and Fig. 4.2 show the DSC result of the Cu and Nd zeolite Y samples.

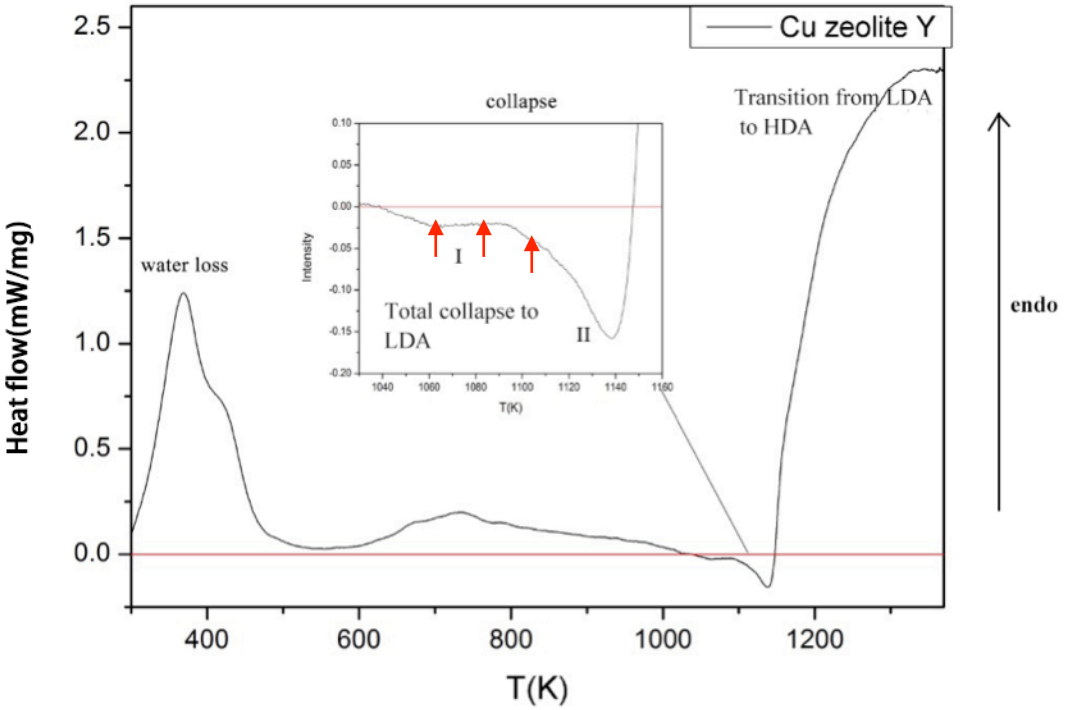

Fig. 4.1 DSC result of hydrated Cu zeolite Y that shows the water loss, and the collapse with heating rate 10K/min. Regions I and II refer to isothermal reaction followed by collapse from zeolite to LDA. The subsequent endotherm follows the conversion from LDA to HDA. The red arrows refers to target temperature used for XRPD and Raman experiments.

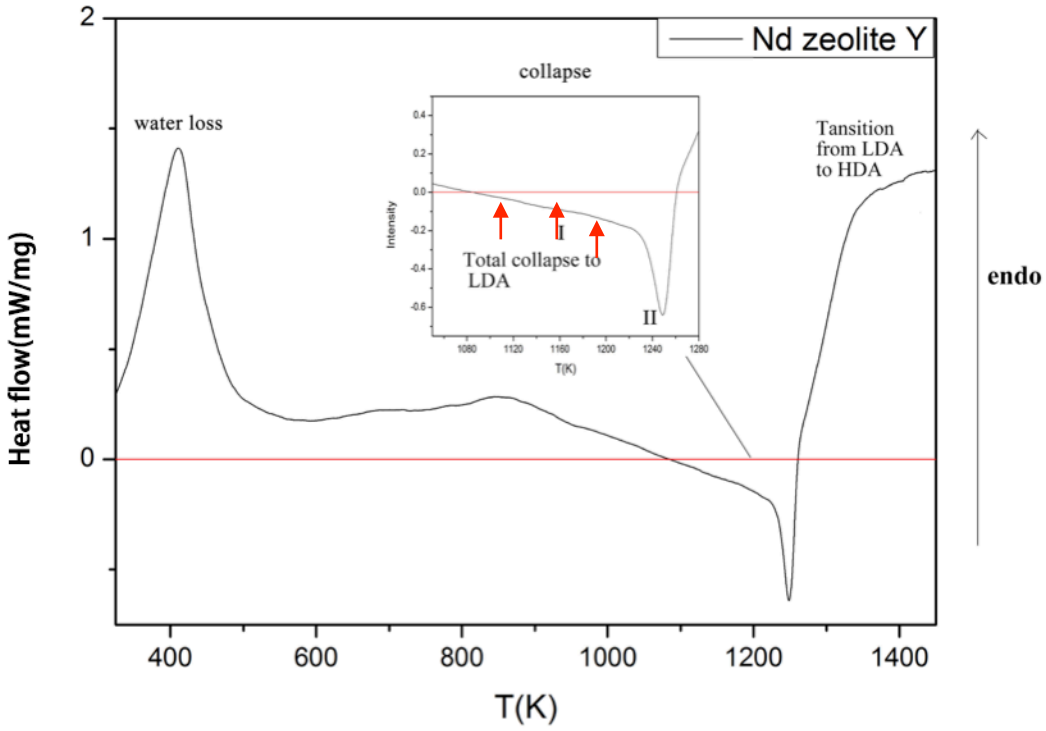

Fig. 4.2 DSC result of hydrated Nd zeolite Y that shows the water loss, and the collapse with heating rate 10K/min. Regions I and II are equivalent to Fig. 4.1, with the conversion to HDA identified. The red arrows refer to target temperature used for *ex situ* XRPD and Raman experiments.

From Fig. 4.1 and Fig. 4.2, it can be seen that most of the water is lost before 500K, where the samples show high endothermic peaks. The collapse curves have been enlarged in both figures, showing that the collapse of Cu zeolite Y happens between 1040K and 1147K, and the collapse of Nd zeolite Y happens at higher temperatures between 1085K and 1260K. Both samples collapse over a large temperature range,

which is similar to Na zeolite Y (Chapter 3, Section 3.2.3). Looking at the enlarged exothermic peaks, two part of the curve with a obvious turn can be seen suggesting the changes of the ion exchanged zeolites from zeolite to low density amorphous state. The following peak suggests the transition from LDA to HDA. [*2*] The target temperatures chosen in the following experiments are marked in the figures.

4.2.4. Amorphous samples preparation for ex situ XRPD and Raman experiments

All the samples were heat treated by the process used for Na zeolite Y (see section 3.2.4). The target temperature and the length of time kept at target temperature for Cu zeolite Y and Nd zeolite Y are listed in Table 4.3 and 4.4, also shown in Fig. 4.3 and 4.4

Time / Target Temperature	0min	20min	40min	60min
1048K	Cu1048-0	Cu1048-20	Cu1048-40	Cu1048-60
1073K	Cu1073-0	Cu1073-20	Cu1073-40	Cu1073-60
1098K	Cu1098-0	Cu1098-20	Cu1098-40	Cu1098-60

Table 4.3 Cu zeolite samples under different heat treatment

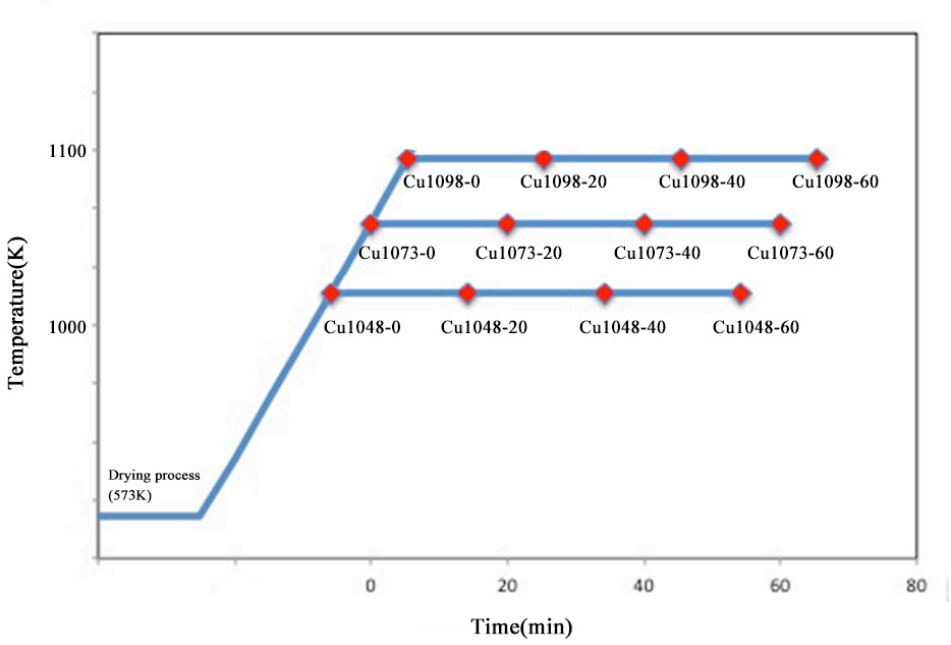

Fig.4.3 Cu zeolite samples under different heat treatments showing target temperature and measurement times (staged by 2 minutes)

Time / Target Temperature	0min	20min	40min	60min
1098K	Nd1098-0	Nd1098-20	Nd1098-40	Nd1098-60
1123K	Nd1123-0	Nd1123-20	Nd1123-40	Nd1123-60
1148K	Nd1148-0	Nd1148-20	Nd1148-40	Nd1148-60

Table 4.4 Nd zeolite samples under different heat treatment

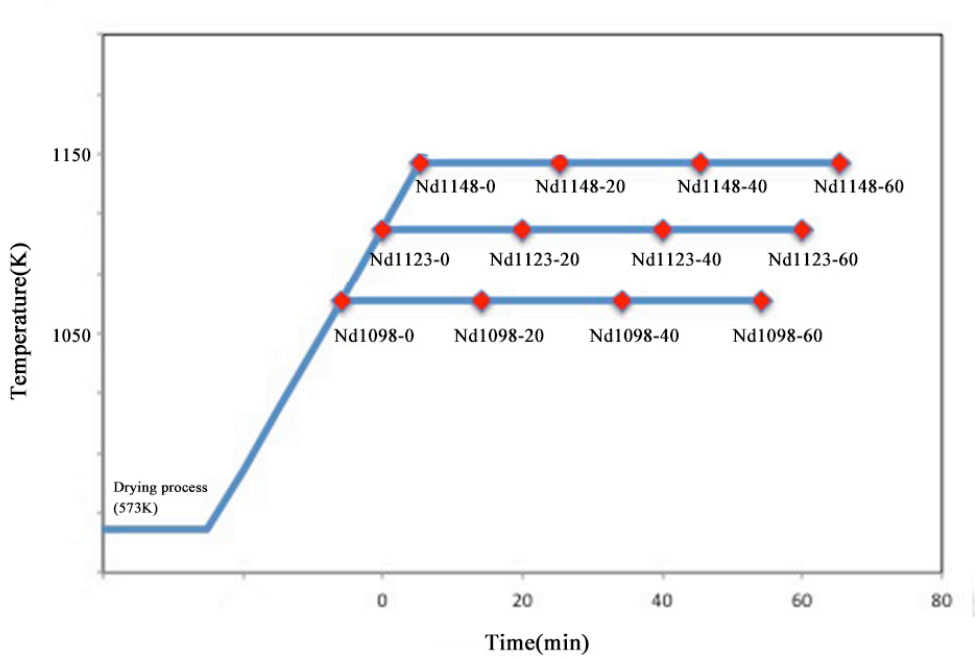

Fig. 4.4 Nd zeolite samples under different heat treatments showing target temperatures and measurement times (staged by 2 minutes)

4.2.5. XRPD

XRPD was conducted on all the samples listed in Table 4.3 and 4.4. The diffraction measurements tests were taken using Rigaku Miniflex 600, with Cu $K\alpha_1$(40kV,15mA, λ=1.5406 Å). As the framework structure stay almost the same in Cu zeolite Y and Nd zeolite Y samples, the XRPD results of dehydrated samples show very similar features as the standard Na zeolite Y.(Fig. 4.5), but with obvious changes of peak intensities of 2θ between 6 and 16 degrees.

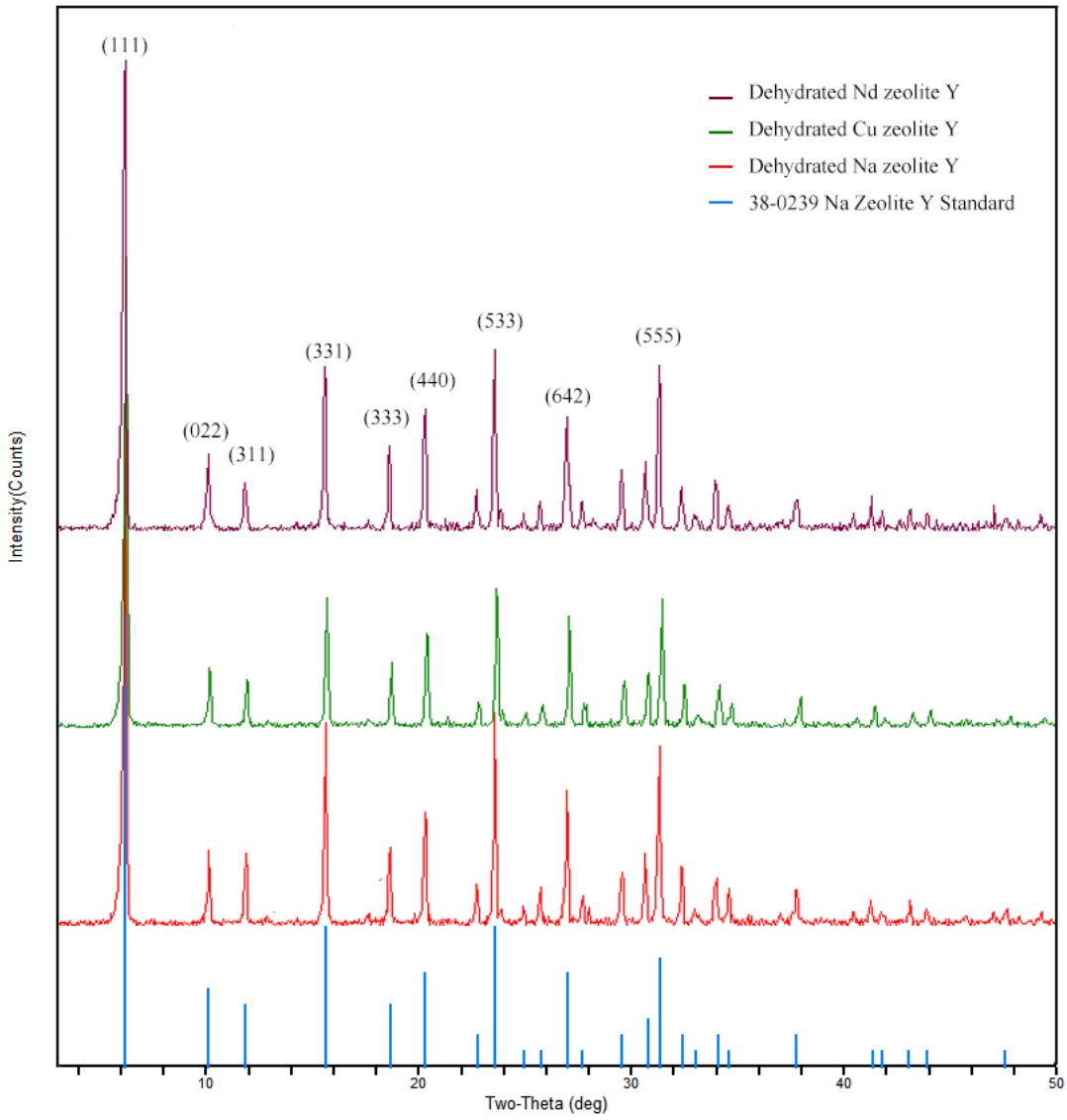

Fig. 4.5 The patterns of dehydrated Cu zeolite Y, Nd zeolite Y, Na zeolite Y and the standard Na zeolite Y. The patterns for Cu and Nd zeolite Y have been offset in the y-axis for comparison.

The XRPD pattern of Cu zeolite Y samples heated at different target temperatures are shown in Fig. 4.6, 4.7 and 4.8. The patterns for 20, 40and 60 min heating have been offset in all three figures in the y-axis for comparison.

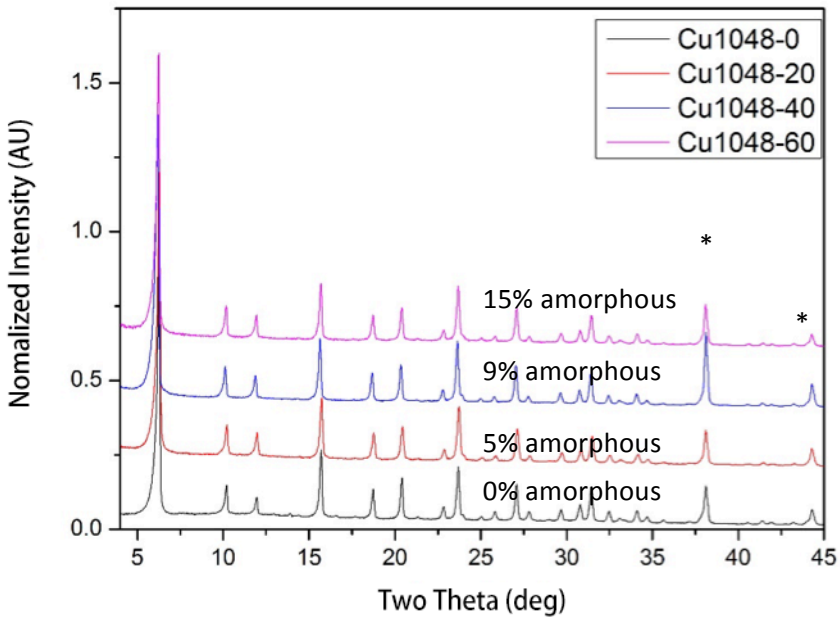

Fig. 4.6 The XRPD pattern of Cu zeolite Y samples at 1048K kept for 0 min, 20 min, 40min, and 60 min. * peaks derive from Al container

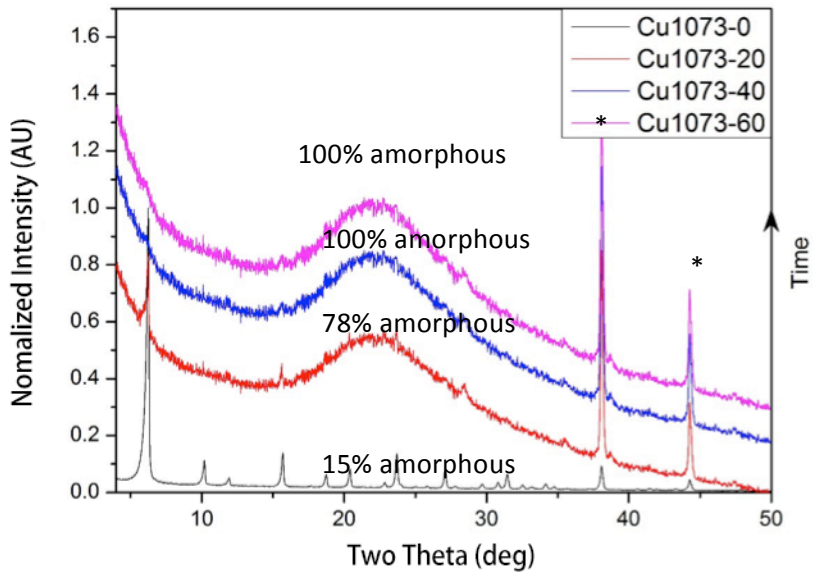

Fig. 4.7 The XRPD pattern of Cu zeolite Y samples at 1073K kept for 0 min, 20 min, 40min, and 60 min. * peaks derive from Al container

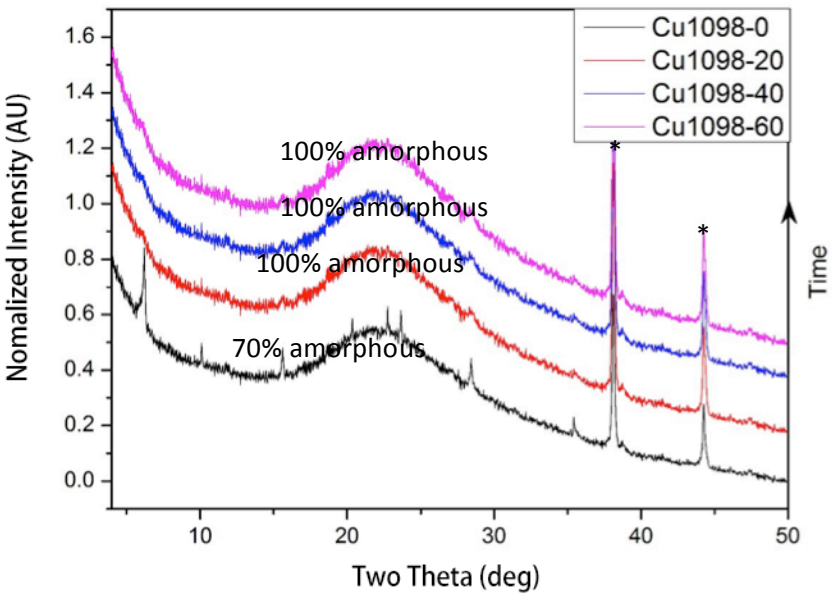

Fig. 4.8 The XRPD pattern of Cu zeolite Y samples at 1098K kept for 0 min, 20 min, 40min, and 60 min. * peaks derive from Al container.

The sequences from 1048K to 1098K clearly show how amorphization become more rapid with high temperature. At 1048 K, there is a small change in the patterns over 60 min, by which time 15% amorphization has resulted. However, at 1073K 100% amorphization results after 60 minutes during which time the zeolite diffraction peaks have completely disappeared. The same can be seen at 1098K except that complete amorphization is achieved after approximately 30 minutes. In all cases amorphization is calculated from the integrated changing area of all peaks 4.5 deg. to 35 deg [*3*].

The XRPD pattern of Nd zeolite Y samples heated at different target temperatures are shown in Fig. 4.9, 4.10 and 4.11. The patterns for 20, 40and 60 min heating have been offset in all three figures in the y-axis for comparison.

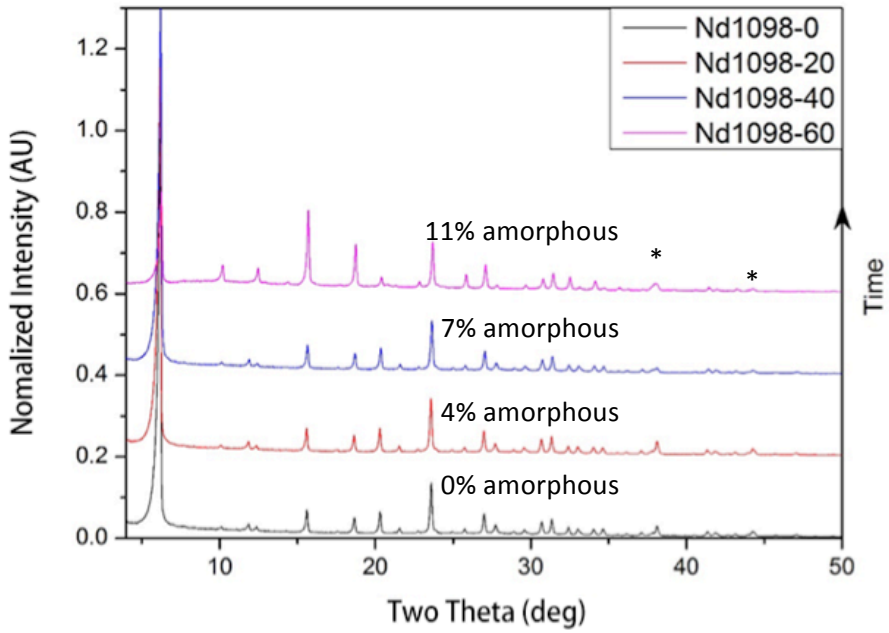

Fig.4.9 The XRPD pattern of Nd zeolite Y samples at 1098K kept for 0 min, 20 min, 40min, and 60 min. * peaks derive from Al container.

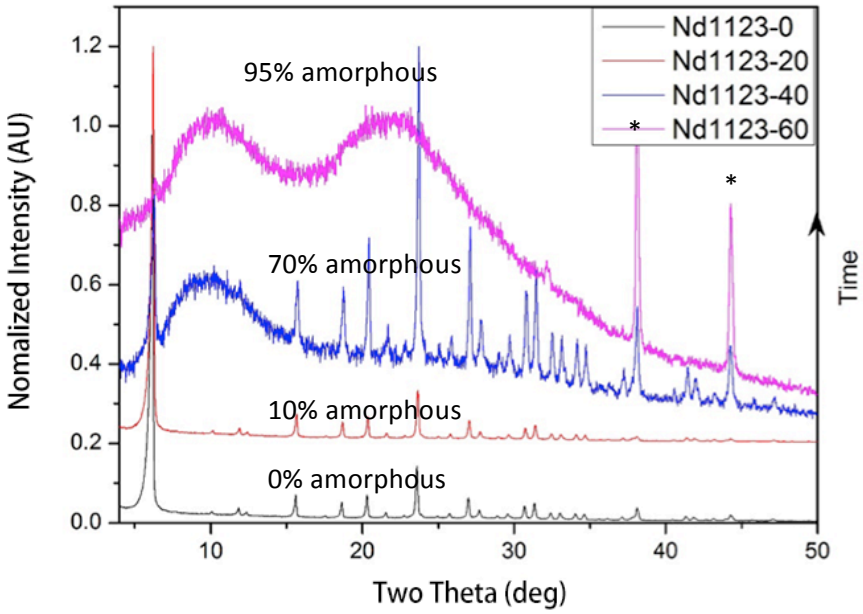

Fig.4.10 The XRPD pattern of Nd zeolite Y samples at 1123K kept for 0 min, 20 min, 40min, and 60 min. * peaks derive from Al container.

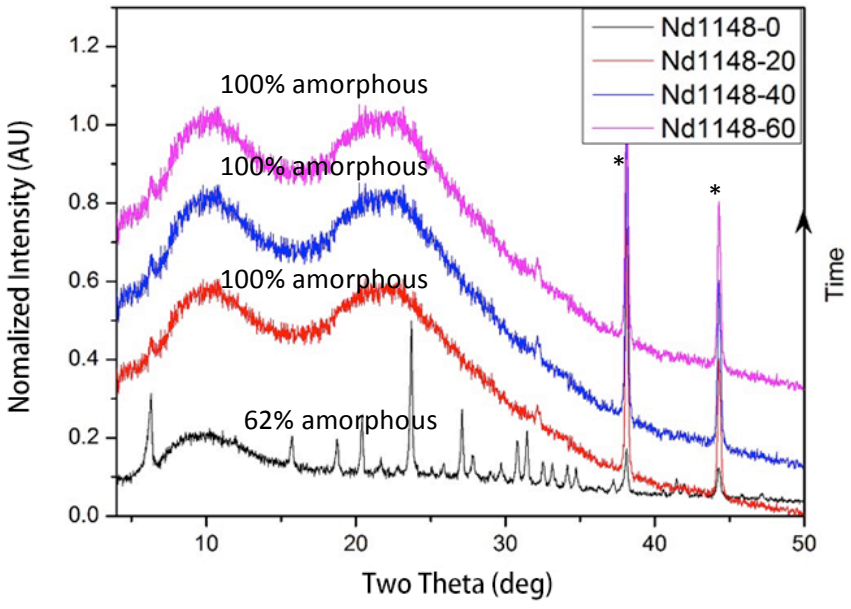

Fig.4.11 The XRPD pattern of Nd zeolite Y samples at 1148K kept for 0 min, 20 min, 40min, and 60 min. * peaks derive from Al container.

Again the consequence of increasing target temperature causes increasing speed of amorphization. The result is similar to Cu zeolite Y except the temperature are higher, 1098K to 1128K. So when Cu zeolite become 15% amorphous in 60 minutes at 1048K, Nd zeolite at 1098K only 11% amorphization is achieved after 60 minutes, and at 1148k amorphization is completed in about 30 minutes. In addition, where diffuse scattering peak occurs at 10 degree for Nd zeolite Y at 1123K and a new peak appear at 22 degrees at 1148K. This 22 degree peak also occurs in Cu zeolite Y, but without the 10 deg peak seen in Nd zeolite Y. The two diffuse peaks can be associated with the First Sharp Diffraction Peak(FSDP) similar to the diffuse peaks in Na zeolite Y after collapse.

Using the degree of amorphization and the heating time, the speed of the collapse can be seen from Fig. 4.12 for Cu zeolite Y and Fig. 4.13 for Nd zeolite Y.

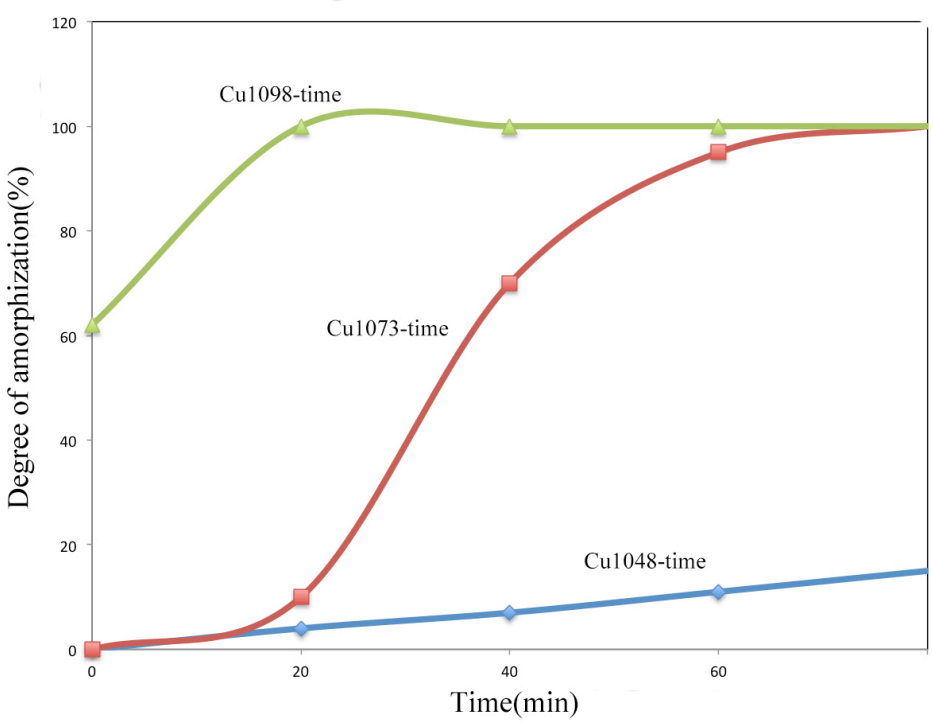

Fig. 4.12 The degree of amorphization against time for Cu zeolite Y

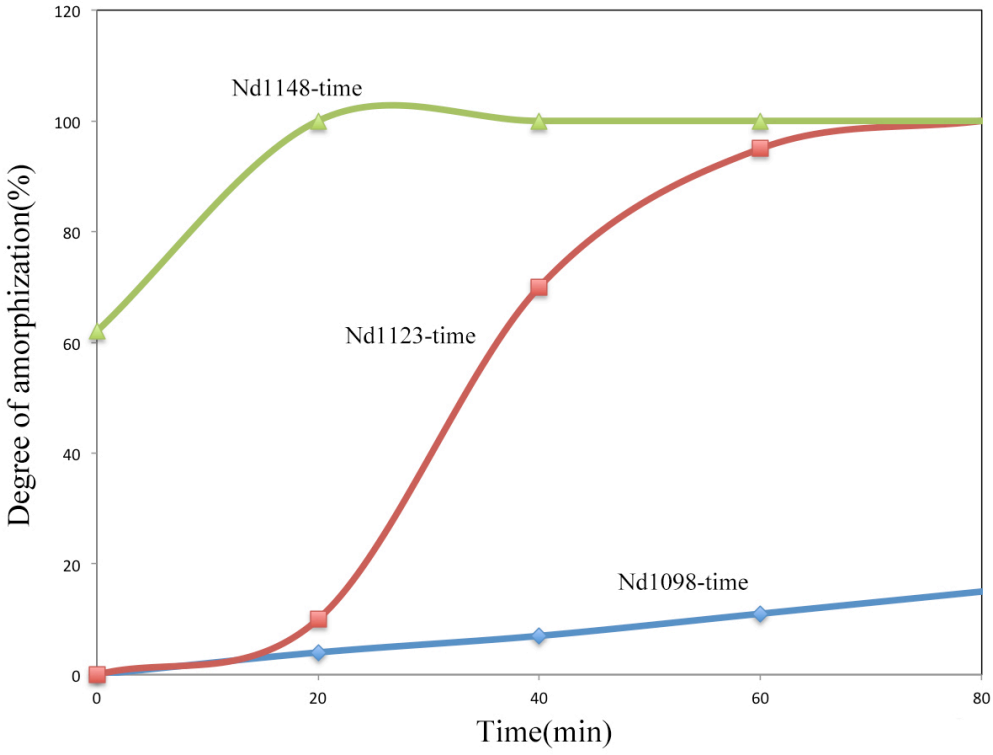

Fig. 4.13 The degree of amorphization against time for Nd zeolite Y

As shown in Fig. 4.12 and 4.13, the speed of collapse is higher with higher temperatures. It can also be seen that once the temperature is high enough the collapse happens very fast in the ion exchanged zeolite Y, however when the temperature is low the collapse is very slow. The speed changes more rapidly over a range of 50K compared to Na zeolite Y (Fig. 3.7).

4.2.6. HR-XRPD

High resolution X-ray diffraction was performed on I11 at Diamond Light source(DLS), using 15 keV,λ=0.825875(10) Å calibrated with a high quality Si standard as mentioned in Section 3.2.6. The initial pattern of Cu zeolite Y and partial amorphous Cu zeolite Y are shown in Fig. 4.14, and the Nd zeolite Y and partial amorphous Nd zeolite Y are shown in Fig. 4.15. All samples were dehydrated and sealed in capillaries as shown in Chapter 2. Significant differences in line intensity and the peak position can be seen in the 45% amorphized sample achieved by heating for 30 min (1123K for Nd zeolite Y and 1073 for Cu zeolite Y).

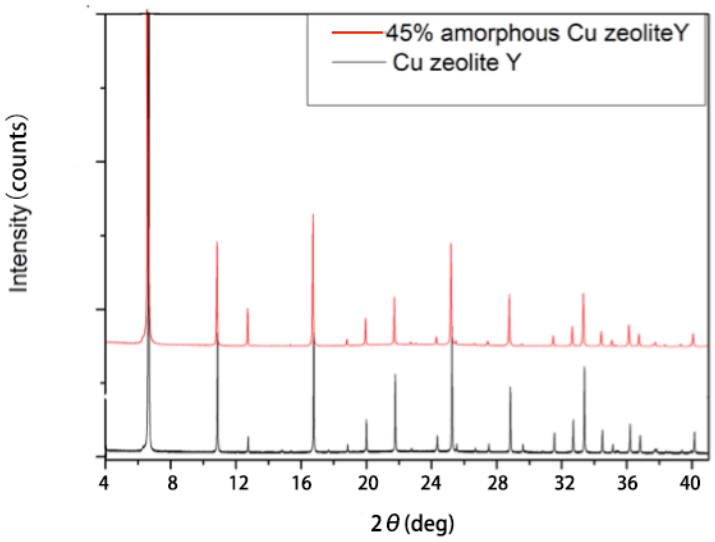

Fig. 4.14 The HR-XRPD pattern of Cu zeolite and partial amorphous Cu zeolite Y sample.

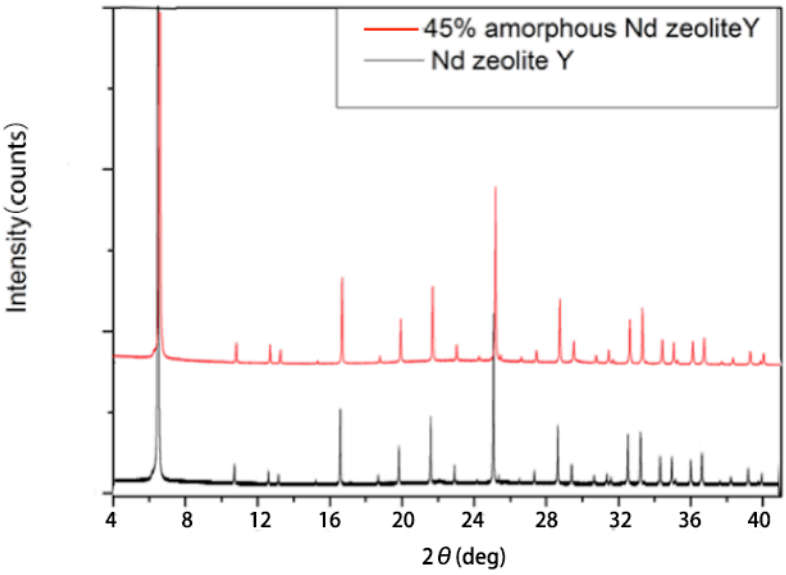

Fig. 4.15 The HR-XRPD pattern of Nd zeolite and partial amorphous Nd zeolite Y sample.

HR-XRPD data were analysed using TOPAS software as introduced in Chapter 2 [*4*]. The unit cells were found to be smaller than the Na zeolite Y structure presented in

Chapter 3. The unit cell parameters, coordinates and occupancies of Cu^{2+} and Nd^{3+} are shown in Table 4.5. Notably, while there were fewer charge-compensating cations present, around 50% of Cu^{2+} were located preferentially in the sodalite cages and 49% of Cu^{2+} in the super cages, but virtually no Cu^{2+} in D6R [*5, 6*]. When it comes to Nd^{3+}, less Nd^{3+} cations stay in sodalite cage, and more located in the super cages. At the same time, the remaining Na^{+} in Cu zeolite Y shift with ion exchange from sodalite cages to super cage to maintain charge balance. In Nd zeolite Y the occupation of Na^{+} is not appreciably altered with ion exchange. Taken together these occupations are understandable. This is commensurate with the size of the compensating ion, as Cu^{2+} is smaller than Nd^{3+}. A Cu atom would replace 2 Na atoms, while a Nd atom would replace 3 Na atoms, and the exchanged cations distribute evenly in the super cages and sodalite cages. After 50% collapse it can be seen that the heat treatment causes the exchange ion to move from super cages to sodalite cages for both Cu and Nd. The unit cell size for Nd zeolite Y is smaller (24. 658Å), however, the unit cell size for Cu zeolite Y is larger (24.673Å) than the uncollapsed samples. The D6R is too constrictive for the Cu^{2+} and Nd^{3+} to occupy. The simulated structure of Cu zeolite Y and Nd zeolite Y shown in Fig. 4.16 indicated that the Cu^{2+} and Nd^{3+} located in more central position in the cages than Na zeolite Y.

Sample	Unit cell parameter, a (Å)	Metal ion in D6R (%)	Metal ion in sodalite cage(%)	Metal ion in super cage(%)
Na zeolite Y	24.715±0.001	5.2	43.0	51.8
Cu zeolite Y	24.632±0.002	0.2 Na:5	50.0 Na25.3	49.8 Na:69.7
Amorphous Cu zeolite Y	24.673±0.002	0.3 Na:5	69.1 Na:38.2	30.6 Na:56.8
Nd zeolite Y	24.674±0.002	0.2 Na:6	40 Na: 35.0	59.8 Na:59.0
Amorphous Nd zeolite Y	24. 658±0.002	0.3 Na:5	65.3 Na:37.1	34.4 Na:56.9

Table 4.5 Cubic size and ion distribution in Cu zeolite Y and Nd zeolite Y. Occupancy errors are +/-0.2%

a

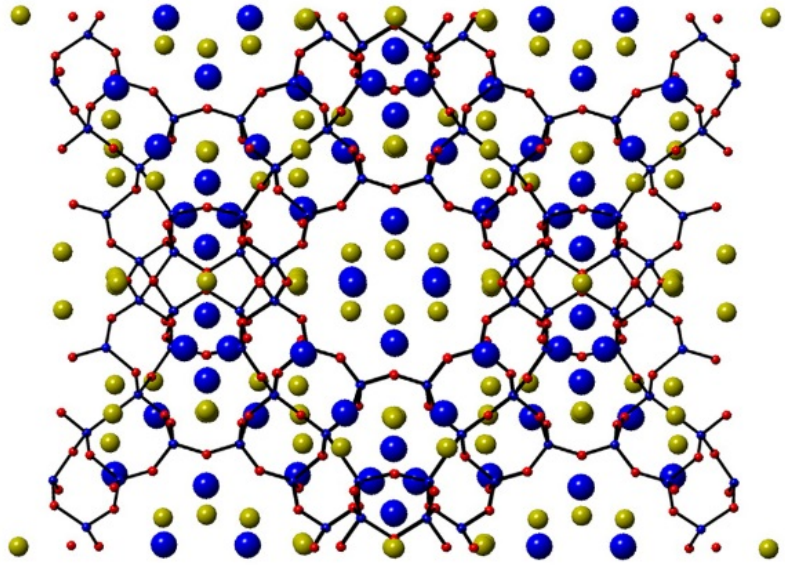

b

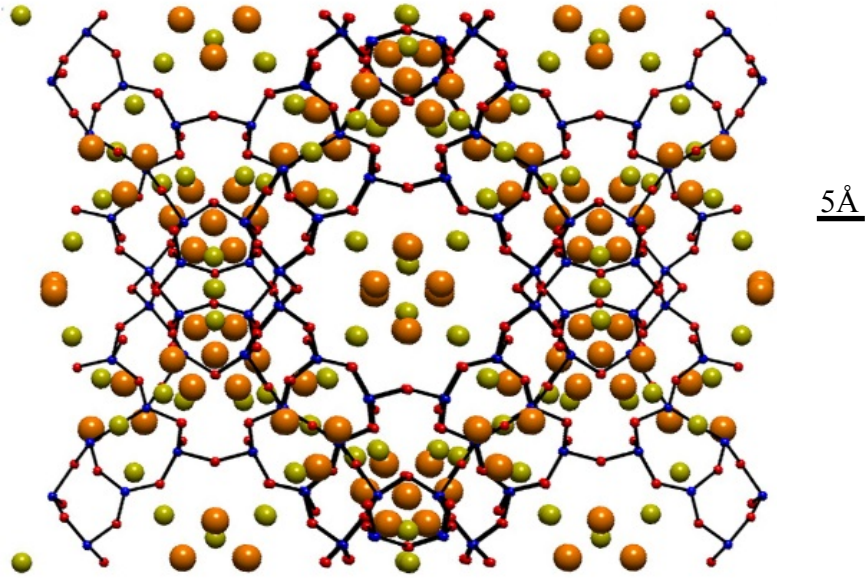

Fig. 4.16 (a) The structure of Cu zeolite Y(one unit cell), where blue balls are Cu atom ,green balls are Na, and the framework buildingballs are Al (small dark blue balls), Si (small dark blue balls) and O (small red balls). (b) The structure of Nd zeolite Y, where orange balls are Nd atoms, green balls are Na and the framework

buildingballs are Al (small dark blue balls), Si (small dark blue balls)and O (small red balls).

Finally , the Rietveld parameters of the refinement are shown in Table 4.6, where the calculated R_{wp} factors are greater for ion exchange zeolite Y than for Na zeolite Y , the experimental R_{exp} factors are similar, reflecting similar experimental conditions. The overall R_p factor is also greater for ion exchanged zeolite reflecting more complex structure. The Final structure model of the three samples shown in Table 4.7

Rietveld parameters	CuNaY	Amorphous CuNaY	NdNaY	Amorphous NdNaY
Scale factor	2.944e-7	3.258e-7	3.686e-7	1.269e-7
Zero point θ	-0.0815	-0.007	-0.0703	-0.00179
Background				
B0	407.143	374.058	550.299	370.148
B1	-105.832	-124.000	-170.106	-183.962
B2	-65.288	-50.434	19.020	46.056
B3	-18.808	-35.124	-101.837	-92.146
Overall isotropic				
R_{wp}	11.743	9.985	10.972	11.064
R_{exp}	2.767	2.929	2.583	3.039
R_p	8.258	7.033	7.626	8.056

Table 4.6 Rietveld parameters of refinement, errors are within 1% of the original data.

As mentioned in Chapter 2.3.1, R_{exp} is very small in these refinements, because the data obtained from synchrotron source (DLS I11) has much greater number of observables (n) than laboratory X-ray analogue due to smaller 2θ step size and much higher observed intensities.

Atom type	x	y	z	Occupation
Cu zeolite Y				
Si， Al	0.125	0.944	0.037	1
O1	0.172	0.172	0.983	1
O2	0.179	0.179	0.325	1
O3	0.252	0.252	0.139	1
O4	0.106	-0.106	0	1
Na1	0.246	0.242	0.246	0.18
Na2	0	0	0	0.11
Na3	0.445	0.561	0.445	0.54
Cu1	0.126	0.186	0.126	0.11
Cu2	0	0	0	0.01
Cu3	0.503	0.615	0.503	0.092
Nd zeolite Y				
Si， Al	0.121	0.952	0.032	1
O1	0.168	0.168	0.972	1
O2	0.179	0.179	0.316	1
O3	0.245	0.245	0.157	1
O4	0.1066	-0.1066	0	1
Na1	0.058	0.058	0.058	0.43
Na2	0	0	0	0.11
Na3	0.414	0.545	0.414	0.25
Nd1	0.071	0.121	0.071	0.17
Nd2	0	0	0	0.012
Nd3	0.0508	0.424	0.508	0.1

Table 4.7 Final structure model of ion exchanged samples, errors are within 1% of the original data.

4.2.7. Raman Spectroscopy

Raman spectroscopy was conducted on a range of sample with different degrees of amorphization with results shown in Fig. 4.17 for Cu zeolite Y and Fig. 4.18 for Nd zeolite Y. Both of the figures show the features of the stretching and bending modes of the T(Al, Si)-O in uncollapsed samples similar to what was found in LSX zeolite which have a Faujasite structure[*7*]. However there are many differences in detail. For Cu zeolite Y and Nd zeolite Y together with Na zeolite Y samples, the bands at 295 cm^{-1} and 384 cm^{-1} are characteristic for the T-O-T bending associated with 6-membered rings, while the 515 cm^{-1} band comes from the 4-fold rings. The higher frequency range of >700 cm^{-1} is dominated by bands associated with T (Si,Al)-O symmetric and asymmetric stretching vibrations. However, when the collapse happens, Cu zeolite Y shows quite different features compared to Na zeolite Y. The band around 515cm^{-1} reduces dramatically, then grows again. Peaks around 300cm^{-1} become the most stable feature, which means that the 4-fold rings first diminish with the collapse and then grow, leaving the 6-fold rings remain relatively stable. In particular the features around 295-385 cm^{-1} broaden with 6-fold and 4-fold rings reducing in favor of 5-fold rings. When collapse occurs for Nd zeolite Y the changes are very similar to Na zeolite Y, reflecting the similarities in the ionic radii. This means that the rings are better defined in collapsed Cu zeolite Y samples than Nd zeolite Y sample and most of the rings are 6-fold ones.

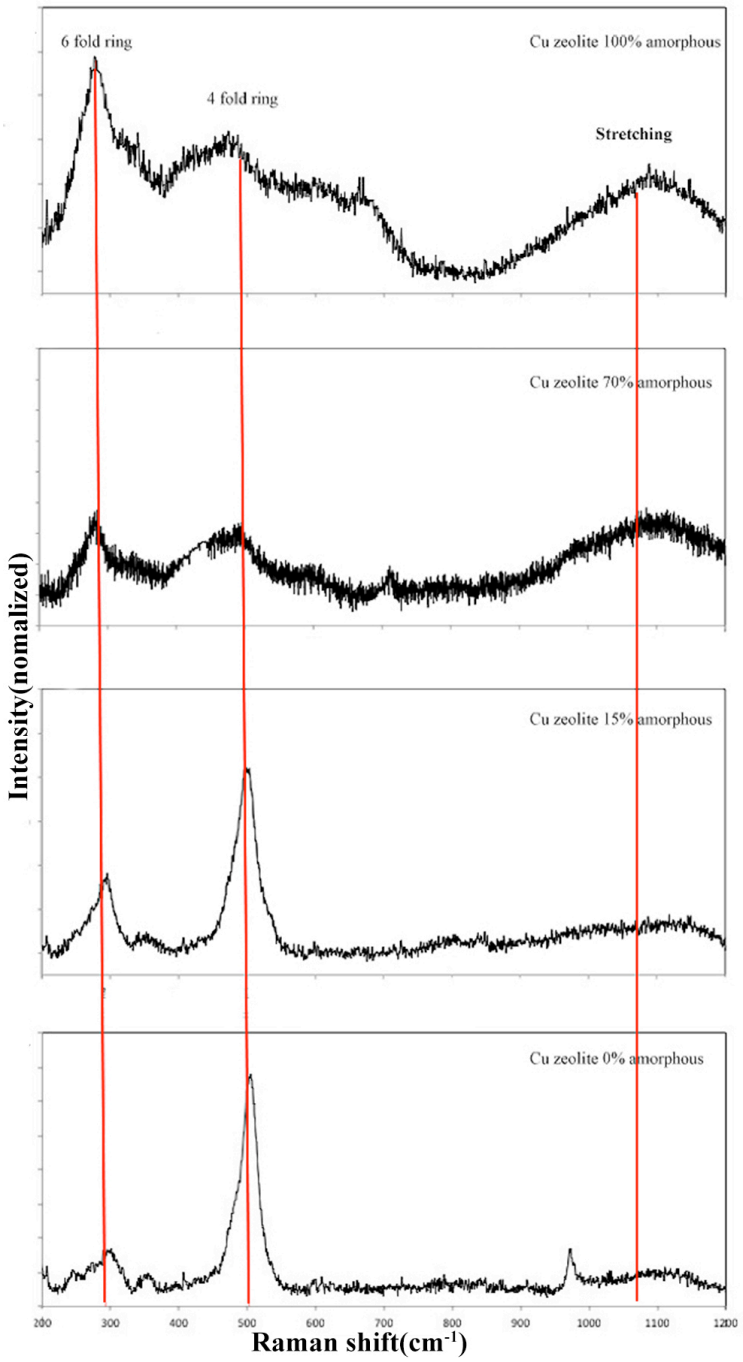

Fig. 4.17 Raman spectra for Cu zeolite Y with different degrees of amorphization

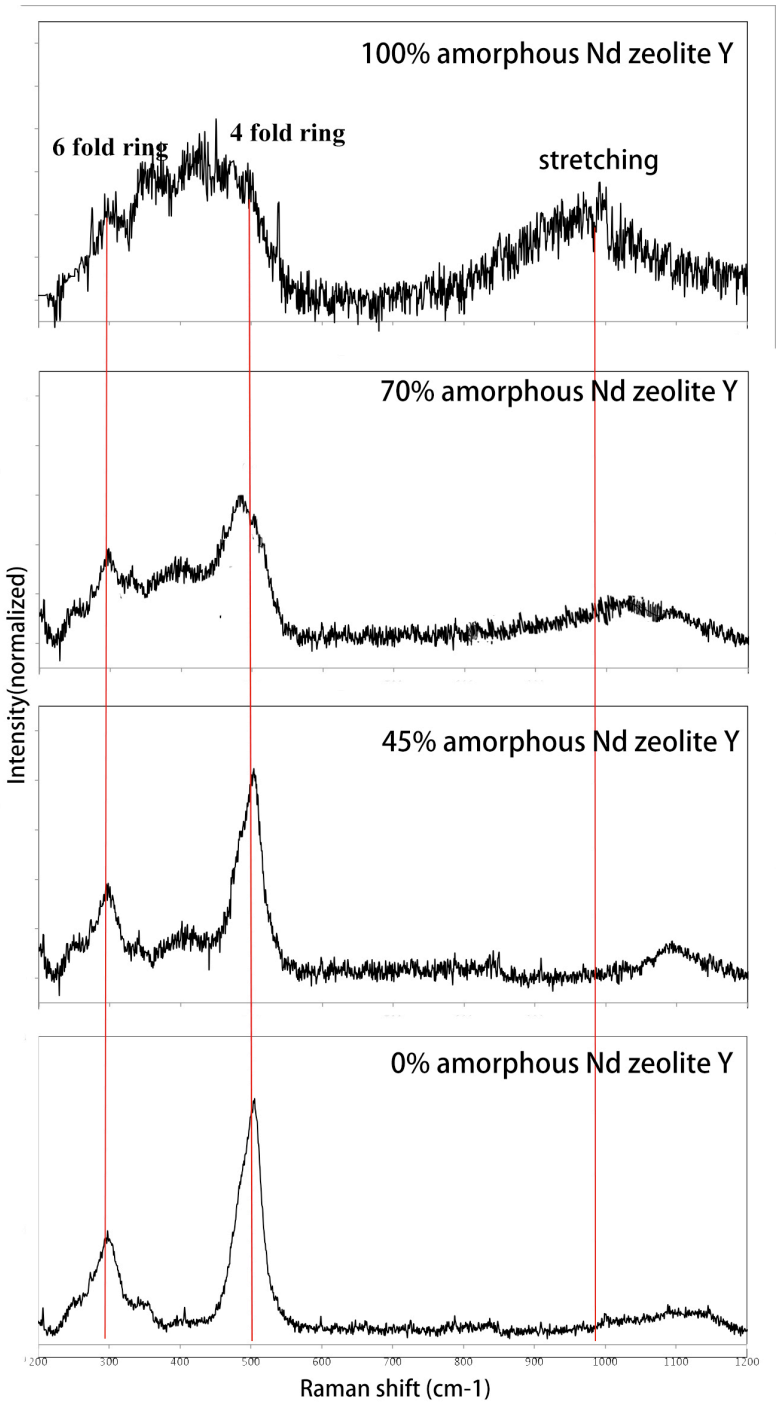

Fig. 4.18 Raman spectroscopy for Nd zeolite Y with different degrees of amorphization

4.3. Results and discussion

4.3.1. DSC

To see the influence of exchange ion on collapse from DSC, the three DSC results are put together in Fig. 4.19. These show very huge changes in the collapse temperature for Na zeolite Y (Fig. 3.1), Cu zeolite Y (Fig. 4.1) and Nd zeolite Y (Fig. 4.2). The exothermic peak becomes sharper following the ion exchange, with collapse temperature range shrinking from 204K (Na zeolites Y) to 107K (Cu zeolite Y) and 175K (Nd zeolite Y). The start temperature of collapse increases with the order Na-Cu-Nd, from 946K to 1040K to 1085K. All these show that the ion exchange increases the collapse temperature at the same time reduces the temperature range over which collapse occurs. The collapse exotherms become less asymmetric in collapsing stucture to LDA for the ion exchange zeolite Y. The zeolite framework survives to higher temperature folloing ion exchange. Ion exchange is known to increase the stability of conventional zeolites [*8*]. The higher temperature of the collapse for Cu zeolite makes it suitable for applications such as Cu exchange ZSM-5 in the dewax reaction [*7*].

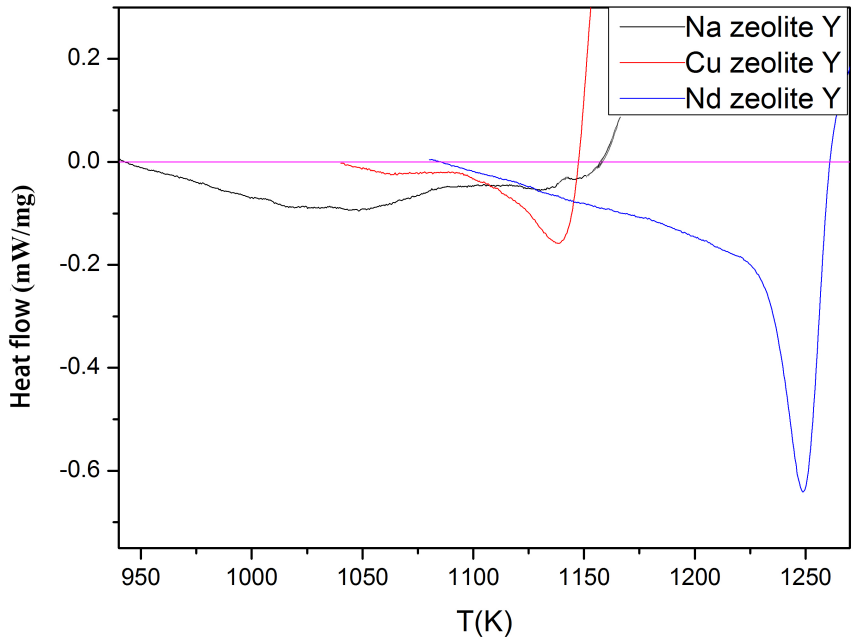

Fig. 4.19 A comparison of the temperature range of collapse for Na zeolite Y, Cu zeolite Y, and Nd zeolite Y.

4.3.2. XRPD

The speed of collapse inferred from DSC is more obvious than the reduction of the crystalline Debye-Scherer pattern over time. XRPD shows that the temperature of collapse increases when the ion exchange has taken place. The speed of collapse also becomes much faster than for Na zeolite Y which means that it is more difficult to reach the collapse temperature for ion exchanged zeolite Y. However when it is reached the collapse is more rapid than for Na zeolite Y. Fig. 3.7, 4.12 and 4.13 show clearly that the dynamics of the collapse become more rapid for ion-exchanged zeolite Y, Nd zeolite Y as the most thermally resistant form of zeolite Y.

4.3.3. HR-XRPD

The unit cells are different in the ion exchanged zeolites as found by HR-XRPD shown in Table 4.5 which includes data from Table 3.4 in Chapter 3. Ion exchange reduces the size of the unit cell considerably, which reflect the higher field strength of the exchanged ions. The field strength can be calculated as Z/r^2 here [*9*], in which Z is the valence of the ion and r is the radius of the ion (Table 4.8). In particular, Cu^{2+} has the highest field strength and shrinks the unit cell the most, Nd^{3+} with medium field strength compared to Na^{+} cause an intermediate reaction. When collapse happened, the unit cell size of Cu zeolite Y become larger opposite to the changes of Na and Nd zeolite Y. This could be due to the movement of the Cu^{2+} from supercages to sodalite cages during heat treatment, making the supercage even larger than uncollapsed Cu zeolite Y.

Sample	Na^{+}	Cu^{2+}	Nd^{3+}
Field strength($1/Å^2$)	1	3.7	2.5

Table 4.8 The field strength of the different charge compensating ion

It is interesting that the unit cell sizes of the ion exchanged zeolite Y is opposite that of the starting collapse temperature. Even though the Cu zeolite Y has a smaller unit cell, it has a lower collapse temperature compared to Nd zeolite Y. This may be the influence of the field strength and the ion occupation in the zeolite Y subunits.

Considering Table 4.5, where occupancies in D6R, sodalite cage and super cage are listed, Nd^{3+} is distributed relatively similar to Na^{+}. However Cu^{2+} is more located in the sodalite cage than the super cage. This suggests that the supercage is more vulnerable to collapse than the sodalite cages and D6R. At the same time Nd^{3+} occupies the super cage similar to Na+, which may explain higher collapse temperature when the heavy Nd^{3+} ion is imported. However, the precise nature of relationship needs more study using greater variety of ion exchange compositions.

4.3.4. Raman spectroscopy

From the Raman spectra it can be seen that the exchanged ion has little influence on the uncollapsed zeolite Y samples. However when the collapse happens, the exchanged ion will influence the Raman considerably such as the ring distribution and the stretching modes. Notably for Cu zeolite Y, the 6- and 4- fold rings that make up the sodalite cage are retained in the LDA phase. However 6-fold rings dominate 4-fold rings compared to the crystalline phase. For Nd zeolite Y, ring modes become hugely broadened, although 6-fold, 5-fold and 4-fold features can be discerned. Combining with the simulated structural changes for Cu and Nd zeolite Y during heat treatment in HR-XRPD section, it suggests that a different route to collapse in its final stage.

4.4. References

1. A. Dyer, *An Introduction to Zeolite Mocular Sieves*. (Wiley, New York, 1988).
2. L. Santona, P. Castaldi, C. Cozza, V.Giuliano, C. Abbruzzese, V. Nastro and P. Melis, "Thermal and spectroscopic studies of zeolites exchanged with metal cations". *Journal of Molecular Structure* 734, 99 (2005).
3. R. B. Von Dreele, L. B. McCusker, D. E. Cox, D. Louër and P. Scardi, "Rietveld refinement guidelines". *J. Appl. Cryst.* 32, 36 (1999).
4. A. A. Coelho, *Topas-Academic*. (A Computer Programme for Rietveld Analysis, 2004.).
5. R. M. Ibberson, M. J. Rosseinsky and A. J. Fowkes, "Structural Characterization of the Redox Behavior in Copper-Exchanged Sodium Zeolite Y by High-Resolution Powder Neutron Diffraction". *Chem. Mater,* 14, 590 (2002).
6. S. Krishnamurty, D. Berthomieu, B. Coq, G. Delahay and Annick Goursot, "Theoretical Modeling of a Copper Site in a Cu(II)-Y Zeolite". *J. Phys. Chem* 105, 1149 (2001).
7. S. Fuhrmann, T. Palenta, G. N. Greaves, W. Schwieger and L. Wondraczek "Thermal collapse and hierarchy of polymorphs in a faujasite-type zeolite and its analogous melt-quenched glass". *J. Chem. Phys.* 142, 084503 (2015).
8. J. Zhang, C. Deng, L. Dong, M. Huang, B. Li, G. Jin, J. Gao, F. Zhang, M. Fan, L. Zhang and Y. Gong, "The effect of positioning cations on acidity and stability of the framework structure of Y zeolite". *Scientific Report* 6, 23382 (2016).

9. I. Joseph, D. Pye, and A. Montenero, *Properties of Glass-Forming Melts*. (CRC Press, Boca Raton, 2005).

5. Conclusions and future work

This research has studied the structure of Na zeolite Y and its collapse, which involves structural, thermal and dynamic changes. Furthermore, ion exchanged zeolites including Cu and Nd zeolite with resident Na are also studied. This includes the structural changes caused by the exchange ions, and the changes during the collapse due to these ions. The reasons for this change are explained. Although quantity of studies have been done, there are still more to be developed such as *in situ* work, inelastic neutron scattering work, and work on more samples with different compositions facilitated by ion exchange conditions which may have commercial value.

5.1. Conclusions

5.1.1. Na zeolite Y

1) The Na zeolite Y material studied has a typical zeolite Y Faujasite structure, whose composition is $Na_{58}Al_{58}Si_{134}O_{384}\cdot 212H_2O$. The unit cell size was 24.715Å, which is smaller than the reference structure ($Na_{59}Al_{59}Si_{133}O_{384}$, ICSD structural database code 159246) (24.791 Å). The ion distribution of the Na was slightly different from the reference structure where the sodalite cages of the studied samples hold more Na (43.0%) than the reference sample (35%), however, the D6Rs hold less (5.2% compared to 11.5%), with the super cages similar (about 50%). This changes with Al/Si (58/134) compared to the reference sample (59/133)

and have not been reported before.

2) DSC results have shown that the collapse happens over a wide temperature range (946K to 1150K). Over this temperature range the speed of collapse changes rapidly from slow to fast. The trend can be seen in Fig. 3.7, Na zeolite Y transfers first from a crystal to LDA at this stage. This is followed by a transition from LDA to HDA. The transformations can be seen in the DSC result (Fig. 3.1). This marks an improvement on earlier work , in which two stage(crystal to LDA， LDA to HDA) process being ambiguous.

3) XRD has shown how the structure changes during the heat treatment. A range of samples with different degrees of amorphization shows this clearly (Fig. 3.4-3.6). When studied by the high resolution XRD, however the changes in each material are more visible showing that the unit cell size shrinks to 24.689Å compared to the starting Na zeolite Y(24.715 Å). In particular the compensating ion moves to smaller cages, with the occupancy in sodalite cage (56.1%) being much less in the largest super cage (37.9%). The movement of Na ions during collapse has not been observed to date and indicates that the energy landscape changes with amorphization.

4) The analysis of the HR-XRPD was done using TOPAS (section 3.3.4, 4.2.6). The high quality data were used successfully to refines the zeolite structure. The

refinement results showed that these structures obtained are reliable. The errors have been reduced to minimum values, generally acceptable for analysis of complex crystalline structures.

5) The Raman spectroscopy has shown the dynamic properties of Na zeolite Y, revealing the stretching and bending modes of the T (Al, Si)-O. The four fold and six fold rings as the basic building units are clearly shown in the result and also the unique peaks showing the stretching vibration. When the collapse happens, the four fold rings remain stable while the six fold rings feature first diminished and then grew, new five fold ring feature grew too. The stretching mode becomes quite complex. These results are qualitatively similar to a recent study of LSX zeolites ($Na_3KAl_4Si_4O_{16}$) and confirm the attribution of Raman modes in caged zeolites during collapse.

6) The inelastic neutron scattering showed the disappearance of the cages with the peaks decreasing and broadening (section 3.2.8). Combined with the Raman result, it showed that smaller cages defined by smaller rings are relatively stable during the collapse as observed earlier.

5.1.2. Ion exchanged zeolite Y

1) After detection by ICP-MS and dehydration, the composition of the two kinds of

ion exchanged zeolite Y studied here were determined to be $Cu_{14}Na_{30}Al_{58}Si_{134}O_{384}\cdot 213H_2O$ and $Nd_{10}Na_{28}Al_{58}Si_{134}O_{384}\cdot 205H_2O$. These compositions also reflect the residual Na present. This is important because all the three cations influence the amorphization.

2) The crystalline structural changes in these ion exchange zeolites have been revealed by HR-XRPD. Notably the exchange ions (Cu, Nd) cause the cages to be smaller in size due to their higher field strength compared to Na as discussed in Section 4.3.3. The exchange ion definitely changes the occupation of the charge compensating ions. As the exchange results in a smaller number of cations compensating, so they are moved to more central positions, while the Na moves to complete the balance of the charge. In the literature, these effects have not been reported so far for Faujasite structure.

3) The about 50% amorphous zeolite Y are also detected by the HR-XRPD, showing that the movement of different cation influence the structural change during amorphization. The unit cell size of amorphous Cu zeolite Y become larger than crystalline Cu zeolite Y, but still smaller than the crystalline Na zeolite Y (Section 4.2.6, Table 4.5). This is due to its high field strength and movement of the cations from supercage to sodalite cage. The change of the amorphous Nd zeolite Y is similar to Na zeolite Y. This has not been reported before.

4) DSC showed a similar result to Na zeolite Y, however the exchange ion causes the collapse temperature to be higher than the Na zeolite Y, e.g. Cu 90K higher and Nd about 130K higher than Na zeolite Y. What is more, the changes between crystal and LDA occur faster with temperature, which results in sharper peaks during collapse. (Fig 4.1 and 4.2) This confirms how the zeolite structures are more stabilized at higher temperatures with ion exchange transition metal and rare earth cations. At the same time the collapse, when it happens, is more abrupt (full collapse for Na zeolite Y costs 22min, Cu zeolite Y costs 11min, and Nd zeolite Y costs 16 min).

5) The XRD results, showing the degree of amorphization have revealed how the structure changes for Cu and Nd ion exchanged zeolite Y. Getting from this result, the speed of collapse (Fig. 4.12 and 4.13) can be followed with different target temperatures, showing that the higher the temperature the faster the collapse, which is similar to Na zeolite Y. However the speed changes during the chosen 50K range are much more obvious for ion exchanged zeolite Y than the Na zeolite Y (Fig. 3.7). Ramifying the DSC results, these *ex situ* experiments show more clearly the retention of stability to higher temperature and the increased dynamics of collapse that follow.

6) The HR-XRPD results for the ion exchanged zeolite Y analyzed by TOPAS were analogous to Na zeolite Y, but with different occupancies of subunits. The R-factor of the ion exchanged zeolite Y is relatively higher than that of Na zeolite Y, but since the chemical composition is acceptable and the structure obtained is reasonable (according to Section 2.3.1), there is confidence in the quality of the zeolite structures obtained and the interpretation of the amorphization process in the ion exchanged zeolites. The R-factors from the Rietveld refinement are helpful indicators, but they are not solely used to confirm the structure model. The importance of the results from HR-XRPD is that the zeolite structures obtained including high precision atomic coordinates and ion occupancies as discussed in Section 3.2.6 and 4.2.6. The structural parameters enabled the interpretation of the amorphization process due to ion exchanged in the zeolites.

7) The Raman spectra of the Cu zeolite Y showed quite different features to Na zeolite Y, with the reductions of the 4 fold and 6 fold peak features during collapse being slight and then growing, with new features like 5 fold rings appearing. In the collapsed features, 6 fold rings dominate 4 fold and 5 fold rings. However the Nd zeolite Y showed the similar features to Na zeolite Y. This is attributed to the ion size, the compensating charge and the occupation. The findings for ion exchanged zeolite Y are new and reveal differences in ring topology between the different cation mixes.

5.2. Future work

5.2.1. Na zeolite Y

To study the dynamic properties we used techniques like Raman and inelastic neutron scattering, however there were some problems doing this work. Considerable improvement could be made with *in situ* Raman experiments. Currently *in situ* changes of the Raman peaks cannot be easily identified which is believed to be due to focusing problem with the remote sensing head in conjunction with a programmable furnace. But it is believed that using the portable Raman as well as a shorter furnace distance this hopefully can be achieved.

The experience at ISIS MARI showed non-reproducibility for the same sample which suggests instrumental problems. Given reproducibility can be solved, the inelastic neutron scattering would benefit more research. For example, we can test the properties of the 50% amorphous samples to see the change partway during the collapse.

5.2.2. Ion exchanged zeolite Y

As only two samples of ion exchanged zeolite Y were tested here, to study the connection between amorphization of the ion exchanged zeolite Y and the size of the exchange ion, more samples could be considered, for example Mg, Ca, Sr, and so on.

What is more, a range of samples with different levels of exchange could also be interesting.

It will be worthwhile to complete the *in situ* Raman on exchanged zeolite Y to see the peak changes defined in *ex situ* Raman during collapse. This would lead to a better explanation of the amorphization mechanism.

Inelastic neutron scattering measurements for the ion exchange zeolite Y would be interesting to see the influence of the exchange ion on the low frequency properties in zeolite Y, when the reproducibility problems are solved.

The ion exchange zeolite Y could be very useful in the industry. It is hoped that this work may lead to some product with future cooperation.